

03/05/148

Form Approved
OMB No. 0704-0188

REPORT DOCUMENTATION PAGE

Public reporting burden for this collection of information is estimated to average 1 hour per response, including the time for reviewing instructions, searching existing data sources, gathering and maintaining the data needed, and completing and reviewing this collection of information. Send comments regarding this burden estimate or any other aspect of this collection of information, including suggestions for reducing this burden, to Department of Defense, Washington Headquarters Services, Directorate for Information Operations and Reports (0704-0188), 1215 Jefferson Davis Highway, Suite 1204, Arlington, VA 22202-4302. Respondents should be aware that notwithstanding any other provision of law, no person shall be subject to any penalty for failing to comply with a collection of information if it does not display a currently valid OMB control number. PLEASE DO NOT RETURN YOUR FORM TO THE ABOVE ADDRESS.

1. REPORT DATE (DD-MM-YYYY) 07/04/07	2. REPORT TYPE Final Performance	3. DATES COVERED (From - To) 25/06/03 - 31/07/06		
4. TITLE AND SUBTITLE Advanced Materials Deposition for Semiconductor Nanostructures Using Supercritical Fluids		5a. CONTRACT NUMBER		
		5b. GRANT NUMBER F49620-03-1-0361		
		5c. PROGRAM ELEMENT NUMBER		
6. AUTHOR(S) Chien M. Wai		5d. PROJECT NUMBER		
		5e. TASK NUMBER		
		5f. WORK UNIT NUMBER		
7. PERFORMING ORGANIZATION NAME(S) AND ADDRESS(ES) University of Idaho Moscow, Idaho 83844-3020		8. PERFORMING ORGANIZATION REPORT NUMBER		
9. SPONSORING / MONITORING AGENCY NAME(S) AND ADDRESS(ES) AFOSR 875 N Randolph Street Suite 325, Room 3112 Arlington, VA 22203-1768 <i>Dr. Donald Selversmith/NE</i>		10. SPONSOR/MONITOR'S ACRONYM(S) ONR		
12. DISTRIBUTION / AVAILABILITY STATEMENT <i>DISTRIBUTION STATEMENT A</i> Approved for Public Release Unlimited Distribution Unlimited		11. SPONSOR/MONITOR'S REPORT NUMBER(S)		
13. SUPPLEMENTARY NOTES				
14. ABSTRACT Supercritical fluid carbon dioxide provides an attractive medium for depositing materials in small structures with high aspect ratios and poorly wettable substrates due to the fact that it is able to dissolve solutes like a liquid and transport dissolved materials like a gas. Metal and metal sulfide nanoparticles of controllable size can be synthesized in supercritical fluid carbon dioxide using water-in-CO ₂ microemulsion as template. Continuous tuning the size of metallic nanoparticles and metal sulfide nanoparticles with diameters from less than 2 nm to over 10 nm can be achieved by varying the density of the fluid phase in the synthetic process. The synthesized nanoparticles are stabilized in the fluid phase using an alkylthiol compound. Deposition of the stabilized metal nanoparticles in the fluid phase forming self-assembled arrays has been demonstrated. Supercritical fluid deposition of metals on surfaces of carbon nanotubes has also been studied. Metal nanoparticles of narrow size distributions can be uniformly attached to carbon nanotube surfaces using this method. The carbon nanotube-supported platinum group metal nanoparticles show remarkably high activities for catalyzing chemical and electrochemical reactions. Examples of utilizing the carbon nanotube-nanoparticle composite materials as catalysts for chemical reactions, fuel cells and sensor applications are given.				
15. SUBJECT TERMS Supercritical Fluid, Nanoparticles, Semiconductor, Nanostructure, Carbon Nanotube				
16. SECURITY CLASSIFICATION OF: a. REPORT U		17. LIMITATION OF ABSTRACT SAR	18. NUMBER OF PAGES 25 pages + appendix	19a. NAME OF RESPONSIBLE PERSON Chien M. Wai
b. ABSTRACT U		19b. TELEPHONE NUMBER (Include area code) 208-885-6787		

Best Available Copy

Standard Form 298 (Rev. 8-98)
Prescribed by ANSI Std. Z39.18

REPORT DOCUMENTATION PAGE

Title: Advanced Materials Deposition for Semiconductor Nanostructures Using Supercritical Fluids (F49620-03-1-0361)

DISTRIBUTION STATEMENT A

Forward

Approved for Public Release
Distribution Unlimited

Supercritical fluid carbon dioxide (SF-CO₂) with its moderate critical constants (T_c = 31 °C and P_c = 73 atm), nonflammable nature and low cost provides an attractive alternative for replacing organic solvents traditionally used in chemical manufacturing processes. Above the critical point, SF-CO₂ exhibits a novel hybrid of gas-like and liquid-like properties. It can dissolve solutes like a liquid and yet possesses low viscosity, high diffusivity and zero surface tension like a gas. In addition, the solvation strength of SF-CO₂ can be tuned by changing the density (i.e. pressure and temperature) of the fluid phase, thus selective dissolution or deposition of compounds may be achieved in supercritical fluid-based processes. These unique properties make SF-CO₂ an attractive medium for depositing materials in small structures with high aspect ratios and poorly wettable substrates to attain high uniformity and homogeneity.

The creation of nanoparticles of controllable size as building blocks for the assembly of supramolecular structures such as nanoparticle thin films and ordered arrays has been an area of considerable interest to material scientists in recent years. Much of the interest has been driven by their prospective applications as electronic devices, optical materials, sensors, molecular catalysts, and others. The purpose of this research is to explore the feasibility of using SF-CO₂ as a medium for synthesizing and depositing advanced materials in small structures of semiconductor substrates. The materials of particular interests are nanometer-sized particles composed of metals, oxides, or sulfides, which are known to be conductors, insulators, and semiconductors. Developing techniques of synthesizing nanoparticles of controllable size and their subsequent deposition in nano-structured substrates in SF-CO₂ is one of the main objectives of this project. Patterned silicon wafers and carbon nanotubes are two types of substrates used for developing supercritical fluid-based materials deposition techniques in this project.

20070426202

Table of Contents

Forward	1
Table of Contents	2
Statement of the Problems Studied	3
Summary of the Important Results	
1. Synthesizing Metal Nanoparticles of Controllable Size in Supercritical Carbon Dioxide Using Water-in-CO ₂ Microemulsion as Template	4
2. Synthesizing Metal Sulfide Semiconductor Nanoparticles of Controllable Size in Supercritical Fluid Carbon Dioxide	7
3. Deposition of Nanoparticles and Array Formation in Supercritical Carbon Dioxide	12
4. Supercritical Fluid Chemical Deposition of Metals in Nano-Structured Substrates	15
5. Applications of Carbon Nanotube-Nanoparticles Composite Materials	17
6. References	22
7. List of Papers Published under AFOSR Sponsorship	23
8. Scientific Personnel	24
Appendix – Reprints of Published Papers	25

Statement of the Problems Studied

A microemulsion-templated method is used for synthesizing metallic and metal sulfide semiconductor nanoparticles of different sizes in SF-CO₂. The water-in-CO₂ microemulsion serves as a nanoreactor for the synthesis as well as a template for controlling the size of the particles. One significant observation from this study is that density of the supercritical fluid phase can be used as a parameter for fine tuning the particle size synthesized by the microemulsion method. Continuous tuning the size of metallic particles and metal sulfide particles with diameters from less than 2 nanometers to over 10 nanometers can be achieved by varying the density of the fluid phase in the synthetic process. The synthesized nanoparticles are stabilized in SF-CO₂ using a chemical stabilizer such as an alkylthiol compound. Deposition of the thiol-stabilized metal nanoparticles in SF-CO₂ forming self-assembled arrays has also been demonstrated. The possibility of synthesizing and depositing metal nanoparticles of adjustable size in nanostructures of silicon wafers using the supercritical fluid technology is currently under investigation.

Direct supercritical fluid deposition of metals in small structures of semiconductor devices with high aspect ratios and in the interior of carbon nanotubes has been demonstrated in our previous studies. Further research in this direction shows that with proper surface treatment, condensation and aggregation of metal nanoparticles can lead to nanoparticle formation on carbon nanotube surfaces. Potential applications of the carbon nanotube-supported metal nanoparticles as catalysts for various chemical reactions have been investigated. Nanoparticles of platinum group metals attached to carbon nanotubes show remarkably high catalytic activities for hydrogenation reactions and for carbon-carbon coupling reactions. Utilization of the nanoparticle catalysts for fuel cell and for sensor applications is also investigated.

Summary of the Important Results

1. Synthesizing Metal Nanoparticles of Controllable Size in Supercritical Carbon Dioxide Using Water-in-CO₂ Microemulsion as Template

There has been much interest recently in synthesizing nanometer-sized metal and semiconductor particles because such particles in the quantum confinement range exhibit size dependent optical and electrical properties. Water-in-CO₂ microemulsions with nanometer-sized water core are well suited as nanoreactors for synthesizing nanoparticles in SF-CO₂.¹ The particle growth occurs within the water core of the microemulsion and the precursors of the nanoparticles are commonly available water-soluble ions. Since the radii of the water cores are determined by the water-to-surfactant ratio (W), the size of the particles synthesized in the microemulsion may be controlled by the W value. Other factors such as density of the fluid phase, which is known to affect the solvation environment of the microemulsion and change the micelle-micelle interactions during collisions, may also be used to control the size of nanoparticles synthesized by the microemulsion method.

We started this research using a water-in-oil microemulsion with a fixed W value for making monodispersive gold (Au) nanoparticles by chemical reduction of Au³⁺ ions to metallic Au with a reducing agent NaCNBH₃. Sodium bis(2-ethylhexyl)sulfosuccinate (AOT) was used as the surfactant to make the microemulsion. The synthesized Au nanoparticles were stabilized with 1-decanethiol. Self-assembling of the protected Au nanoparticles in an evaporating hexane solution leads to the formation of 2D and 3D arrays of gold nanoparticles. Figure 3 shows a TEM micrograph of a 2D array of Au nanoparticles formed on a carbon coated copper grid using this method. When water-in-hexane microemulsion was used for the synthesis, we obtained 2D arrays of Au nanoparticles with an average particle size of 4.7 and a RSD (relative standard deviation) of 7.5 %. When the synthesis was done using a water-in-heptane microemulsion, 2D arrays of 3.8 nm average size gold nanoparticles with RSD of 5.4 % were observed. Solvent appears to play a role in determining the size of the gold nanoparticles synthesized by the water-in-oil microemulsion method. The results of this study were published in early 2006 ("A Simple and Rapid Method of Synthesizing 2D and 3D Arrays of Gold Nanoparticles", *Journal of Nanoscience and Nanotechnology* **2006**, *6*, 669-674).

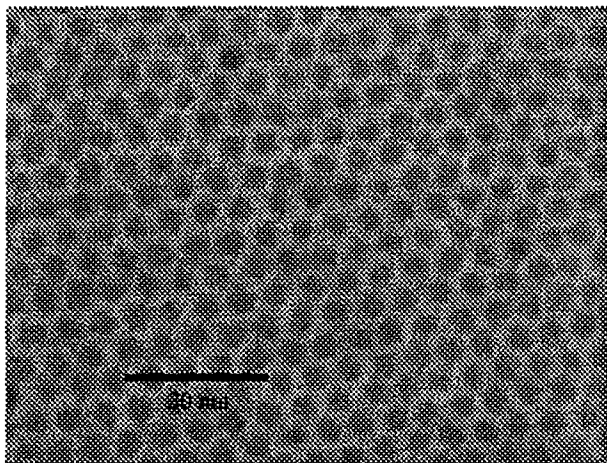


Figure 3. 2-D array of gold nanoparticles synthesized by the microemulsion method in hexane.

The Hildebrand solubility parameter is a classical thermodynamic concept of evaluating solubility of a solute in a solvent. In terms of the Hildebrand solubility parameter, carbon dioxide near its critical point density ($\phi_c = 0.47 \text{ g mL}^{-1}$) is similar to liquid hexane at room temperature.^{2,3} The solubility parameter of SF-CO₂ increases with density and may approach that of liquid toluene or carbon tetrachloride at higher densities. Since SF-CO₂ is a tunable solvent, we can easily manipulate its solvation strength by changing density (determined by pressure and temperature) of the fluid phase. Therefore, density may be used as a simple factor for the fine tuning of nanoparticle size synthesized by the microemulsion method. To make water-in-CO₂ microemulsion, a fluorinated AOT surfactant, sodium bis(2,2,3,3,4,4,5,5-octafluoro-1-pentyl)-2-sulfosuccinate, was used in our experiments. Fluorine containing compounds are known to have high solubilities in SF-CO₂.⁴ The synthesized Ag nanoparticles were stabilized by a perfluorodecanethiol compound. We used this water-in-CO₂ microemulsion system to study the effects of pressure and temperature on size distribution of silver (Ag) nanoparticles synthesized in SF-CO₂. Our results indicate that the size of the Ag nanoparticles synthesized by the CO₂ microemulsion method does depend on the density of the SF-CO₂ phase and continuous tuning of Ag nanoparticle size can be achieved by varying density of the fluid phase. Figure 2A shows the variation of average Ag nanoparticle size synthesized by the CO₂ microemulsion method with respect to pressure at a fixed temperature (40 °C) in SF-CO₂. Figure 2B shows the variation of Ag nanoparticles with temperature at a fixed pressure (280 atm) synthesized by the same method.

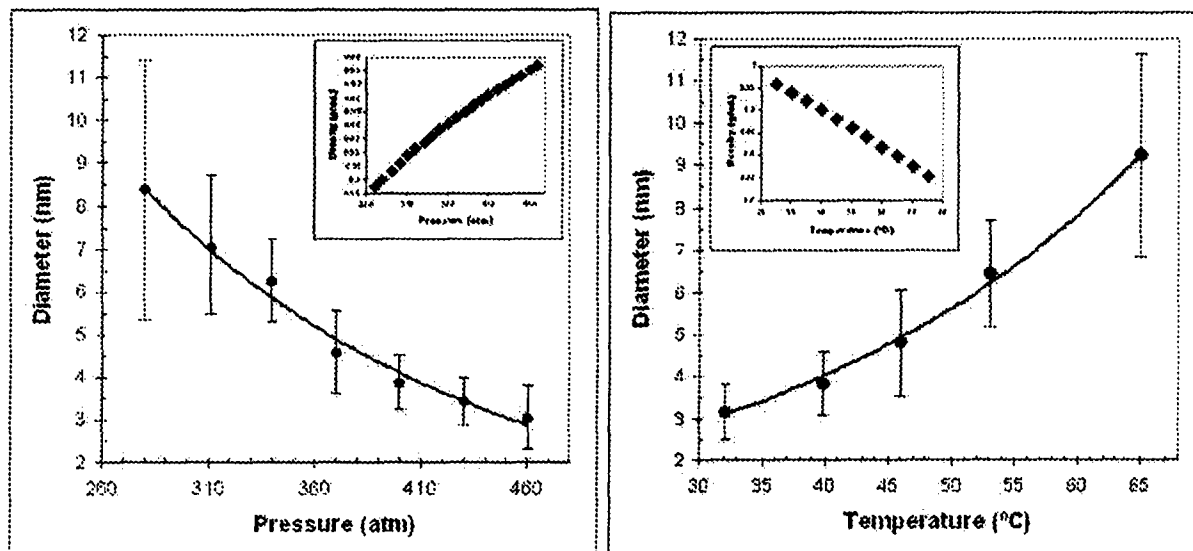


Figure 2. Left: (A) Variation of Ag nanoparticle size with respect to pressure at 40 °C (W=6). Right: (B) Variation of Ag nanoparticle size with temperature at 280 atm (W=6). The insets in the figures show variation of density with respect to P and T.

The pressure and temperature of the experiments shown in Figure 2 can be expressed in terms of the density of the fluid phase.⁵ When the average diameter of the Ag nanoparticles synthesized by the CO₂-microemulsion method is plotted against the density of the fluid phase, the experimental data given in Figures 2A and 2B can be fitted into a straight line (Figure 3A for W=6). The observed linear relationship suggests that the average Ag nanoparticle size can be tuned continuously by varying density of the fluid phase during the synthesis. Within the density range of our experiments, the average Ag particle size varies from 9.3 nm at 0.80 g mL⁻¹ to 1.9 nm at 0.96 g mL⁻¹ with a slope of -0.04 nm/(g mL⁻¹). Higher density tends to form smaller Ag nanoparticles using the CO₂-microemulsion synthetic method. One plausible explanation is that the cohesive energy density of the SF-CO₂ solvent is higher at increased density (higher P or lower T), which results in enhanced ligand-solvent interactions.^{2,3} Therefore, at higher pressures or lower temperatures, the surfactant molecules of the microemulsion are more solvated by SF-CO₂, resulting in weaker micelle-micelle interactions. The net effect might be a decrease in the amount of material exchange during micelle-micelle collision; as a result smaller Ag particles with narrower size distributions are obtained.

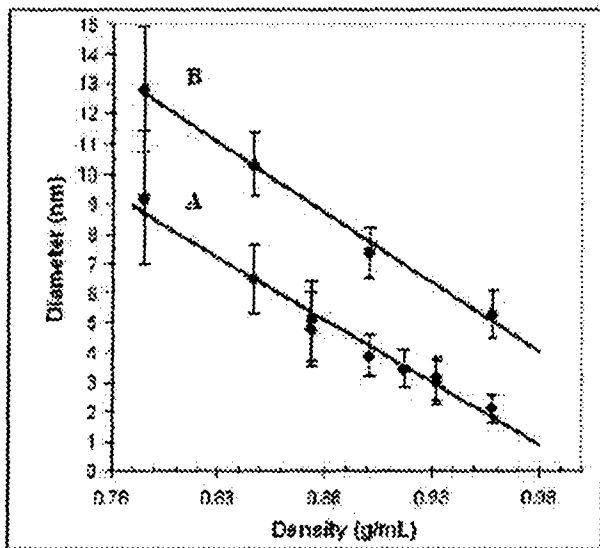


Figure 3. Influence of CO_2 density on the average size and size distribution of silver nanoparticles at $W=6$ (A) and at $W=10$ (B)

When the size of the microemulsion is increased from $W=6$ to $W=10$ (W is the mole ratio of water to surfactant used in the microemulsion preparation) for the Ag nanoparticle synthesis, the same linear relationship between the average Ag particle size and the density of the fluid phase is observed. In this case, the average Ag particle size varies from 12.8 nm at 0.80 g mL^{-1} to 5.4 nm at 0.96 g mL^{-1} , as shown in Figure 3B. Therefore, by manipulating both the W value and the density of the fluid, a wide size range of nanoparticles may be synthesized in SF- CO_2 using the microemulsion method. The results of this study were published in *Small* in 2006 (“Continuous Tuning of Silver Nanoparticle Size in a Water-in-Supercritical Carbon Dioxide Microemulsion”, *Small* 2006, 2(11), 1266-1269).

2. Synthesizing Metal Sulfide Semiconductor Nanoparticles of Controllable Size in Supercritical Fluid Carbon Dioxide

Synthesizing semiconductor quantum dots, such as CdS and ZnS nanoparticles, has been largely explored during the past decade due to their size-dependent optical, magnetic and electric properties. Luminescence tagging and imaging, medical diagnostics, and nanoelectronics are some of the applications that are being developed with these nanomaterials. One method of synthesizing metal sulfide nanoparticles of adjustable size is using microemulsion as a template. In an earlier study, we showed that CdS and ZnS nanoparticles can be synthesized in SF- CO_2

using a microemulsion-plus-microemulsion method.⁶ In this approach, one microemulsion containing the desired metal ions (Cd^{2+} or Zn^{2+}) is added to another microemulsion containing the sulfide ions (S^{2-}) in a high-pressure supercritical fluid reaction cell equipped with optic fibers for in situ spectroscopic measurement of the resulting metal sulfide nanoparticles. From the absorption spectra, we concluded that the size of the metal sulfides synthesized can be adjusted by the W value or the water-to-surfactant molar ratio. Since the solvation strength of the supercritical fluid can be tuned by density of the fluid phase, this may be a simple parameter for controlling the size of the metal sulfide nanoparticles synthesized by the microemulsion method.

The surfactant used in this study is the same as that described in the previous section for the synthesis of silver nanoparticles in SF-CO_2 . The formation of metal sulfide nanoparticles in SF-CO_2 using the two-microemulsion method is illustrated by the following diagram. After the synthesis, the metal sulfide nanoparticles were stabilized by the same fluorinated decanethiol compound used in the silver nanoparticle study for spectroscopic characterization.

Synthesis of metal sulfide nanoparticles using a microemulsion-plus-microemulsion method

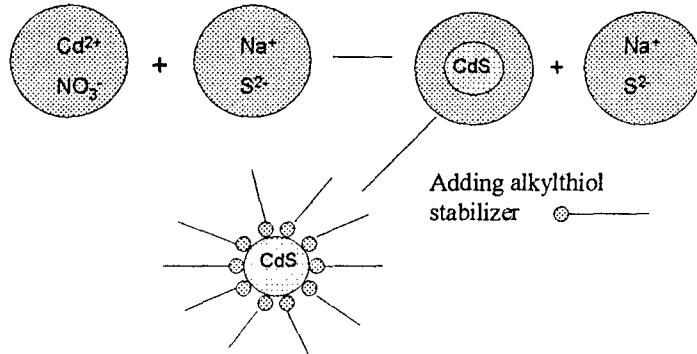


Figure 4(a) shows a plot of the average CdS nanoparticle size with the SF-CO_2 density using different pressure-temperature combinations, for $W = 10$. A linear relationship between the average size of the CdS nanoparticles and the density of the fluid phase (in the range 0.86 to 0.99 g cm^{-3}) is observed. The average size of the semiconductor particles varies from $7 \pm 1 \text{ nm}$ at 0.86 g cm^{-3} to about $2.1 \pm 0.3 \text{ nm}$ at 0.99 g cm^{-3} , with a slope of $-0.036 \text{ nm}/(\text{mg mL}^{-1})$. The

size dispersion varied from 12 % to 20 % in all the experiments, in general larger size particles occurred at lower densities. From Figure 4(a), it seems possible that a continuous tuning of the CdS nanoparticle size synthesized using the CO₂-microemulsion method could be achieved by varying the density of the fluid in this range. Figure 4(b) shows the diameter of the nanocrystals as a function of density for W = 6, where the size varied from 4.0 ± 0.5 nm to 1.3 ± 0.2 nm. A linear relationship with a slope of -0.020 nm/(mg mL⁻¹) similar to the one obtained for W = 10 was observed. Our results suggest that the nanoparticle's size follows a linear relationship with the density of the fluid phase independently of the size of the microemulsion. Consequently, by manipulating both parameters, density, and W value, the diameter of the metal sulphide nanoparticles could be tuned over a wide range of values.

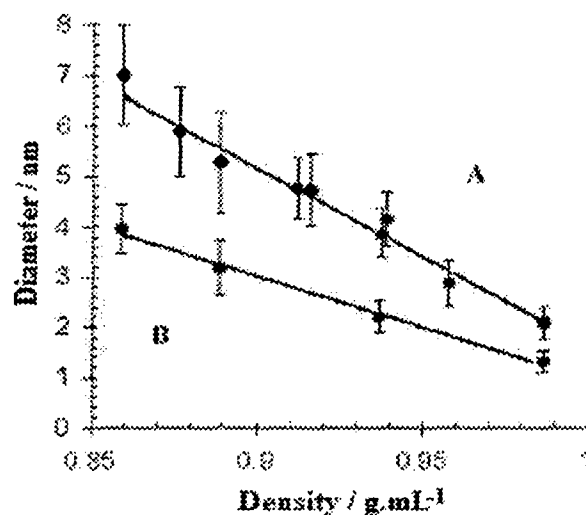


Figure 4. Influence of SF-CO₂ density on the average size and size distribution of CdS nanoparticles. (a) W=10; (b) W=6; surfactant concentration (F-AOT)=10 mM.

Figure 5 shows a representative excitation and emission spectra of the stabilized CdS nanoparticles obtained at two different densities of SF-CO₂. A red shift of 14 nm (from 349 nm to 363 nm) together with an increase in the Full Width at Half Maximum (FWHM) from 48 nm to 63 nm, was observed in the excitation spectra when the density of the solvent decreased from 0.92 g/mL to 0.87 g/mL (W=10 F-AOT concentration 10 mM). This is related to the observed increase in the average size of the CdS particles from 4.7 ± 0.7 nm to 6.0 ± 0.9 nm, when the synthesis of the materials is carried out at lower fluid densities. The emission spectra are

probably associated with the emission of the surface defects, such as electron-hole pair recombination of surface trap states. Yet, a red shift in the fluorescence wavelength from 440 to 498 nm was observed when the size of the CdS nanoparticles increased in the range described above.

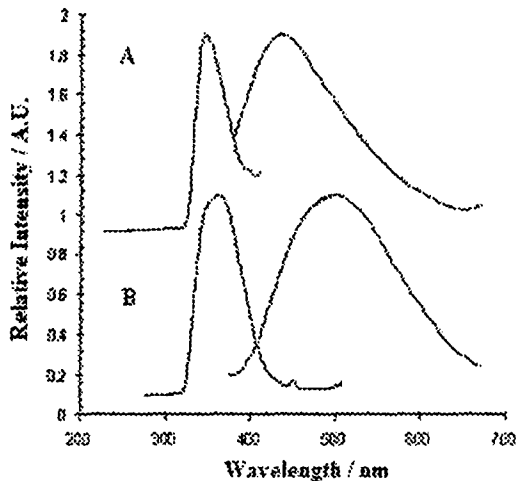


Figure 5. Excitation and emission spectra of CdS nanoparticles obtained at two different fluid densities. (a) Spectra of 4.7 nm (average) CdS nanoparticles obtained at an SF-CO₂ density of 0.92 g mL⁻¹; (b) spectra of 6.0 nm (average) CdS nanoparticles obtained at 0.87 g mL⁻¹.

The variation of the size of ZnS nanoparticles with the fluid density was studied by performing experiments in a similar way to that of the CdS nanoparticles. Figure 6 shows a plot of the variation of ZnS nanoparticles with the density of SF-CO₂ for two different W values. When the W value was 10 (Figure 6A), the size of the nanoparticles decreased from 9 ± 1 nm to 1.9 ± 0.3 nm, when the density of the solvent increased from 0.86 g/mL to 0.99 g/mL. The slope of the trend line was -0.053 nm/(mg mL⁻¹). When W = 6 was used in the preparation of the microemulsions, the size of the ZnS particles synthesized decreased from 7 ± 1 nm to 1.5 ± 0.2 nm with a slope of -0.042 nm/(mg mL⁻¹), as shown in Figure 6B. The increase in the average size of the nanoparticles with the size of the micelles (W value) in SF-CO₂ microemulsions follows the same trend as that described previously for CdS nanoparticles.

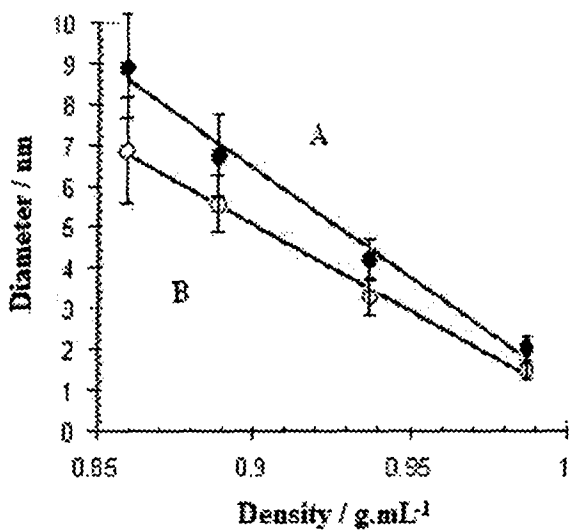


Figure 6. Influence of SF-CO₂ density on the average size and size distribution of ZnS nanoparticles. (a) W=10; (b) W=6; surfactant concentration (F-AOT) = 10 mM.

On Figure 7, the excitation and emission spectra of the stabilized ZnS nanoparticles obtained at two different densities of carbon dioxide are shown. A red shift of 23 nm (from 263 nm to 286 nm) and an increase in the FWHM from 22 nm to 30 nm, are observed in the excitation spectra when the density of the solvent decreased from 0.99 g/mL to 0.89 g/mL. These results are in agreement with an increase in the average size of the ZnS particles from 2.0 ± 0.3 nm to 6.7 ± 0.9 nm, when the synthesis of the materials is carried out at lower fluid densities. Similar to what we observed for CdS nanoparticles, the emission spectra of ZnS nanoparticles show a red shift in the fluorescence wavelength from 340 nm to 373 nm when the size of the ZnS nanoparticles increased.

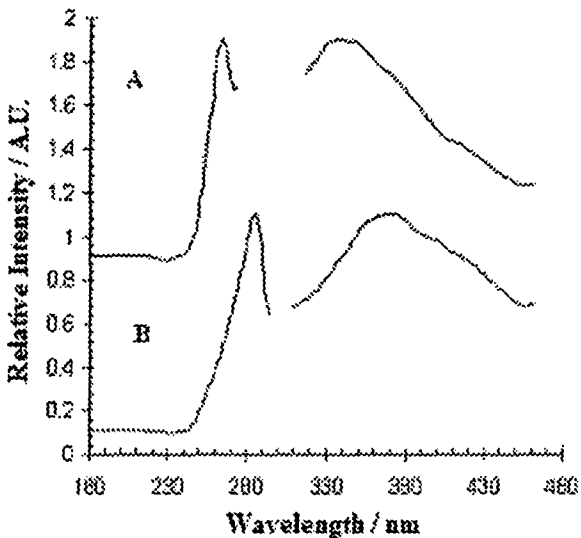


Figure 7. Excitation and emission spectra of ZnS nanoparticles obtained at two different SF-CO₂ densitites. (a) Spectra of 2.0 nm (average) ZnS nanoparticles obtained at a CO₂ density of 0.99 g mL⁻¹; (b) spectra of 6.7 nm (average) ZnS nanoparticles obtained at a density of 0.89 g mL⁻¹.

In addition to the W value and the density, other parameters such as the concentration of the surfactant and the precursor ions used in the synthesis can also affect the size of the nanoparticles. The ability of continuous tuning of nanoparticle size by density is significant because this parameter can be easily controlled by varying pressure or temperature of the supercritical fluid phase. The particle size distribution appears large especially for the nanoparticles synthesized at lower densities. The microemulsion-templated technique requires further refinement for production of monodispersive nanoparticles with narrow size distribution. The chemical nature and the structure of the chemical stabilizer used for stabilizing the synthesized nanoparticles are also important for preserving the nanoparticle size and for their subsequent deposition and array formation in SF-CO₂. The distance between the nanoparticles in ordered 2-D arrays probably can be controlled by different alkyl chain length or structure of the chemical stabilizer. Further research along this direction is currently in progress at the University of Idaho and in Dr. Gail Brown's laboratory at WPAFB.

3. Deposition of Nanoparticles and Array Formation in Supercritical Carbon Dioxide

Production of stable nanoparticle building blocks with uniform size and shape is a prerequisite for the assembling and formation of ordered nanoparticle arrays and films. Utilizing microemulsion as a template followed by addition of a chemical stabilizer appears to be a promising approach for making stable nanoparticles of controllable size as the building blocks

for making ordered arrays. Deposition and self-assembling of the stabilized nanoparticles in SF-CO₂ may be achieved by two different approaches. One approach is by reducing pressure of a SF-CO₂ solution containing a saturated amount of the stabilized metal nanoparticles causing precipitation of the solute from the solution. The second approach uses an anti-solvent effect in SF-CO₂ causing precipitation of stabilized metal nanoparticles in an organic solution. In the second approach, the metal nanoparticles are stabilized by a chemical reagent which is not soluble in SF-CO₂ but can be dissolved in an organic solvent. When the solution is in contact with SF-CO₂, the organic solvent will dissolve in the supercritical fluid phase by raising pressure of the system. This method of removing the solvent from the organic solution would cause precipitation of the stabilized metal nanoparticles on substrates submerged in the organic solution. Evaporating the organic solution in SF-CO₂ tends to form more uniform and long-range 2-D arrays, probably due to the near zero surface tension of the fluid.

Both approaches have been tested in our studies. The second approach appears to be able to produce long range arrays of gold nanoparticles. Figure 8 shows the TEM image of a decanethiol stabilized gold nanoparticle array formed by the SF-CO₂ anti-solvent effect. The stabilized gold nanoparticles prepared by the microemulsion method were first dissolved in toluene. The toluene solution in a small glass vial with a carbon coated copper grid on the bottom was placed in a high-pressure view cell with quartz windows. The pressure of the SF-CO₂ system was raised slowly until all solvent was dissolved in the supercritical fluid phase. The supercritical fluid solution was then slowly released from the system by opening an exit valve. Ordered 2-D arrays of gold nanoparticles can be formed on the copper grid as illustrated in Figure 8.

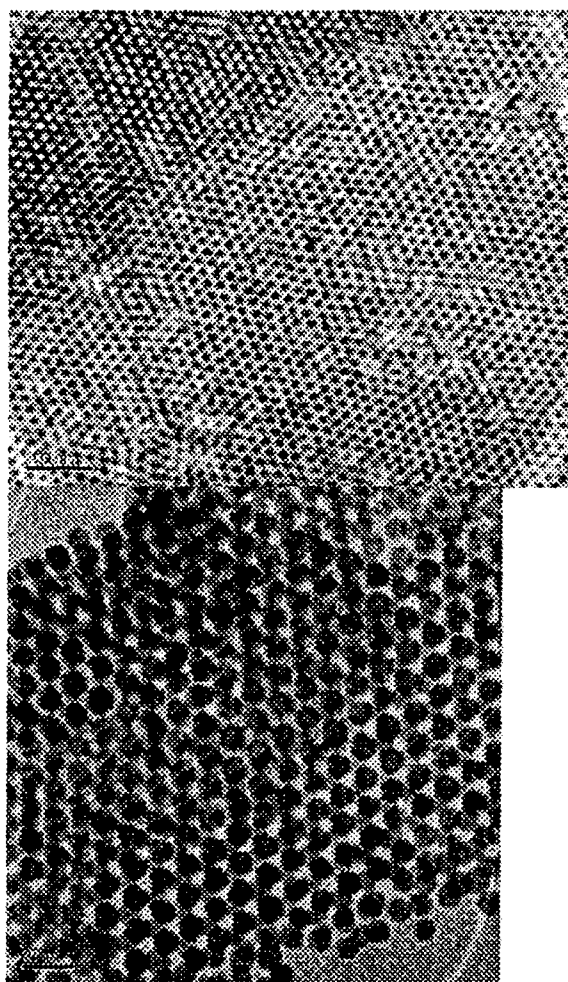
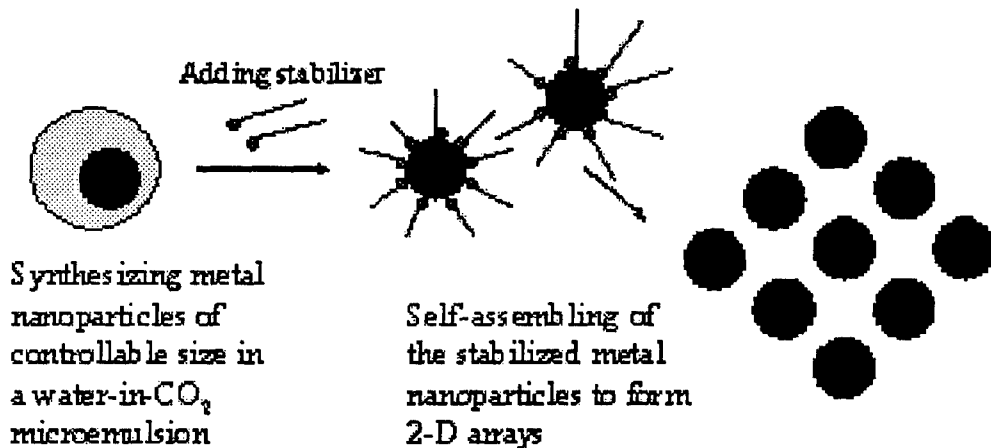


Figure 8. Array of gold nanoparticles formed by SF-CO₂ evaporation of a toluene solution containing dodecanethiol stabilized gold nanoparticles synthesized by a microemulsion method.

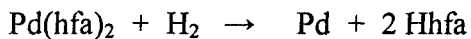
Research in nanoparticles deposition using SF-CO₂ as a medium is still in progress at the University of Idaho and in Dr. Gail Brown's laboratory at WPAFB. The technique should be able to adjust the particle size and the distance of separation between the particles arranged in an ordered fashion in a small area as illustrated in the following diagram. Formation of a grid or array of conductive nanodots that are isolated from each other and uniformly distributed in a precisely defined location has a number of potential application in microelectronics. For example, the conductive volume could be the target recipient of tunnelling electrons, through an adjacent dielectric layer, as the charge trap to regulate the switching voltage threshold of a transistor, thus defining the state of the "bit". This is a part of the nanocrystal Flash memory strategy that some semiconductor companies are currently pursuing. We plan to test such

nanocrystals prepared in SF-CO₂ for possible charge storage study in 2007 in collaboration with a semiconductor company (Micron Technology, Inc.) in Idaho.



4. Supercritical Fluid Chemical Deposition of Metals in Nano-Structured Substrates

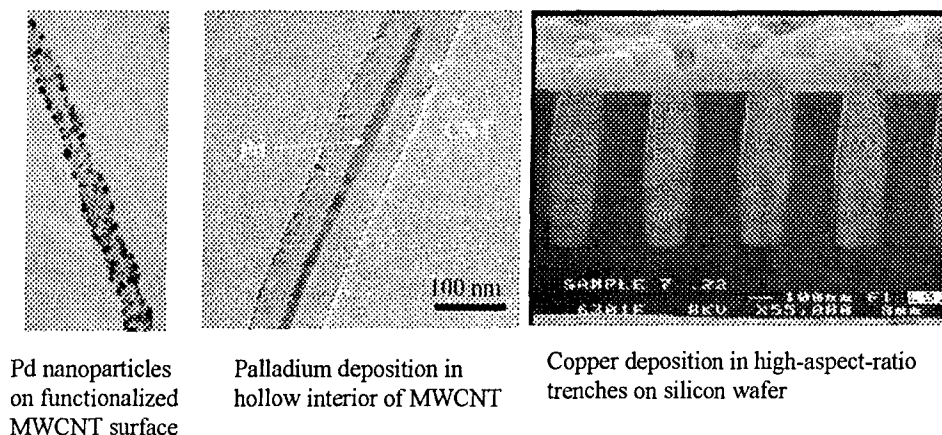
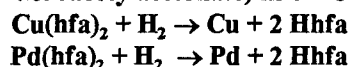
In our previous studies, we have demonstrated that metals can be deposited in small structures with high aspect ratios by chemical reduction of a metal precursor dissolved in the SF-CO₂ phase. Metal β -diketonates have been widely used as precursors because of their high solubilities in SF-CO₂. A number of transition metal- β -diketonates can be reduced to their elemental state by hydrogen at moderate temperatures in SF-CO₂. For example, by hydrogen reduction of a palladium precursor Pd(hfa)₂ (hfa=hexafluoroacetylacetone) in SF-CO₂, palladium metal film can be formed on the surface of a semiconductor substrate according to the following reaction.



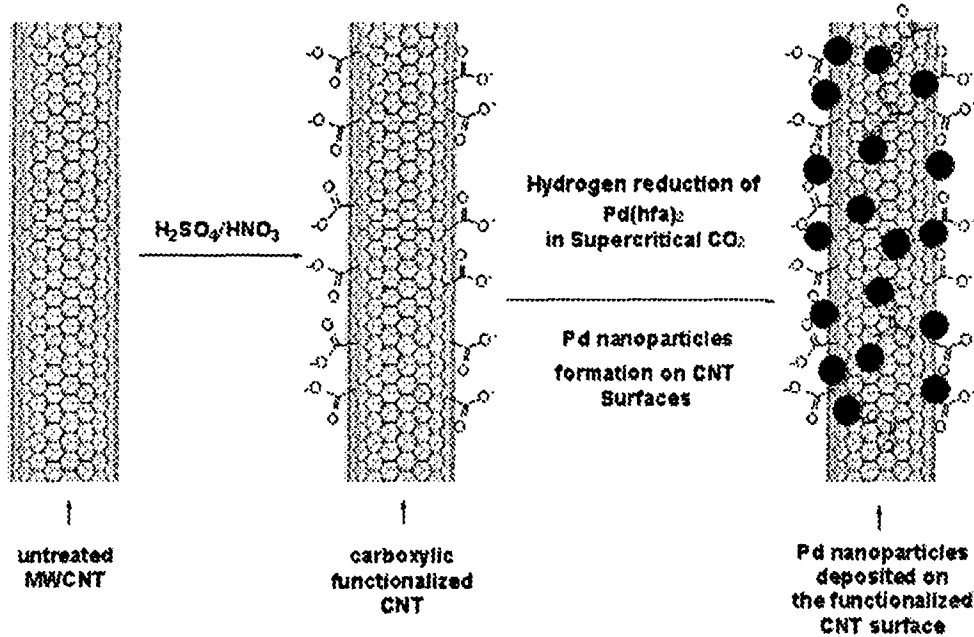
For palladium reduction, this reaction occurs at a relative low temperature (50 °C or higher) with 3 atm of H₂ in 80 atm of CO₂. For copper and nickel, the required temperature is ≥ 250 °C. The metal films deposited on silicon wafers using the supercritical fluid chemical deposition (SFCD) method exhibit good adhesion, smooth morphology, and high purity. Because of the penetration ability of SF-CO₂, metals can be deposited in high-aspect-ratio small structures using the SFCD method. In a previous study, we showed that device quality copper can be deposited in high-aspect-ratio trench structures by hydrogen reduction of Cu(hfa)₂ in SF-CO₂ (Figure 9). In the presence of a small amount (2-5%) of Pd(hfa)₂, the required temperature for copper deposition

can be significantly reduced to 100 °C or lower.⁷ Palladium probably acts like a catalyst for the copper deposition in SF-CO₂. In another report, we demonstrated that the SFCD method is capable of depositing metals such as Pd, Cu, and Ni in the hollow interiors of multi-walled carbon nanotubes with diameters in the range of 10 nm or less.⁸ These reports suggest that SFCD is a potential technique for depositing advanced materials in nanostructures of semiconductor devices. Continuation of this research for metal oxide deposition in small structures of semiconductor devices using metal alkoxide as precursor in SF-CO₂ is currently in progress at the University of Idaho and in Dr. Gail Brown's lab at WPAFB.

**Hydrogen reduction of metal-hfa
(hexafluoroacetylacetone) in SF-CO₂**



An interesting observation in our carbon nanotube study is that when the MWCNTs are treated with acids prior to the SFCD of metals, nano-metersized metal particles are formed on the surfaces of the nanotubes. Acid treatment of MWCNTs is known to result in carboxylate formation on the surfaces of the nanotubes which apparently can serve as active sites for nucleation and growth of metal nanoparticles during the SFCD process. The metal nanoparticles are uniformly dispersed on the surfaces and often show a narrow size distribution. The high curvature of the CNT surfaces is probably a factor that permits only a certain size range of metal nanoparticles to be attached. Surface modified carbon nanotubes with metal particles have a number of potential applications including catalysts, sensor materials, and nano-electronics.



5. Applications of Carbon Nanotube-Nanoparticles Composite Materials

We have investigated some potential uses of the carbon nanotube-based nanoparticle composite materials for chemical catalysis and sensor applications. One example is the preparation of MWCNT-supported platinum (Pt) nanoparticles using the SFCD method and their potential use as an electrochemical catalyst for low temperature proton exchange membrane fuel cell application. The CNT-supported Pt nanoparticle catalyst prepared by the SFCD method shows much higher activities for oxygen reduction and for methanol oxidation compared with commercial carbon-based Pt catalyst. Carbon nanotube-supported bimetallic nanoparticles can also be synthesized by the SFCD method. According to the literature, platinum-ruthenium (Pt-Ru) bimetallic catalyst is effective for preventing poisoning of Pt catalyst in anodic oxidation of methanol. We synthesized a MWCNT-supported Pt-Ru bimetallic nanoparticle catalyst using the SFCD method with two metal precursors $\text{Pt}(\text{acac})_2$ and $\text{Ru}(\text{acac})_2$ with a molar ratio of 1:1 in the SF- CO_2 phase, where acac stands for acetylacetone. Methanol was used as a modifier in this case to increase the solubility of the metal precursors in SF- CO_2 . Figure 9 shows a typical TEM micrograph of the carbon nanotube-supported bimetallic Pt-Ru nanoparticles prepared by the direct SFCD method. The XRD (powder X-ray diffraction) pattern shows a slight shift of the Pt peaks indicating a possible alloy formation for the bimetallic Pt-Ru nanoparticles. The EDS

(energy dispersive X-ray spectroscopy) spectrum shows both Pt and Ru are present in the decorated carbon nanotubes.

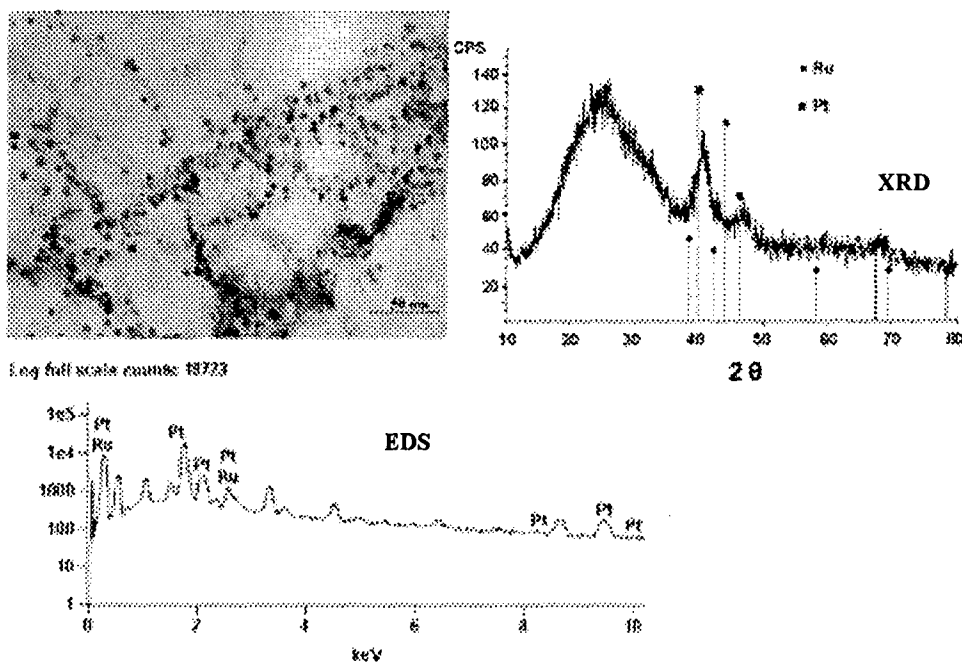


Figure 9. Carbon nanotube-supported Pt-Ru bimetallic nanoparticles prepared by the SFCD method.

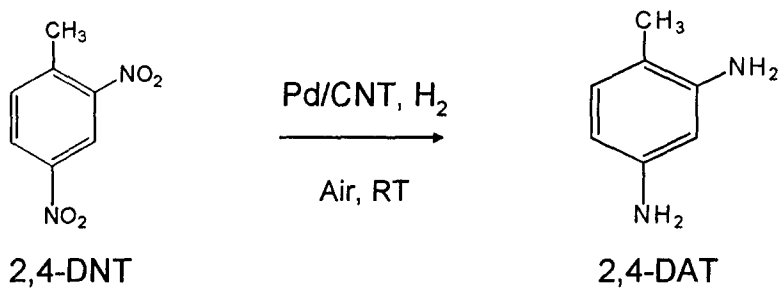
The carbon nanotube-supported Pt and bimetallic Pt-Ru nanoparticles exhibit remarkably high electrocatalytic activities for cathode reduction of oxygen and for anode oxidation of methanol. These new nanocatalysts appear important for developing more efficient and durable low temperature fuel cells such as direct methanol fuel cells. The results of this study were published in 2005 ("PtRu/Carbon Nanotube Nanocomposite Synthesized in Supercritical Fluid: A Novel Electrocatalyst for Direct Methanol Fuel Cell", *Langmuir* 2005, 21, 11474-11479).

The CNT-supported Pd nanoparticles show high chemical catalytic activity for hydrogenation reactions and for C-C coupling reactions. The catalytic activities of the carbon nanotube-supported Pd nanocatalysts are much higher compared with commercially available Pd catalysts stabilized on carbon black. In addition to its high catalytic activity, the CNT-supported metal nanopartical catalyst can also be recycled for repeated use. A paper describing the CNT-supported Pd nanoparticles for the Suzuki coupling reactions was published in 2006

(“Recyclable and Ligandless Suzuki Coupling Catalyzed by Carbon Nanotube-Supported Palladium Nanoparticles Synthesized in Supercritical Fluid”, *Synthetic Communications* **2006**, *36*, 3473-3478). Another paper describing the catalytic activities of carbon nanotube-supported palladium-rhodium bimetallic nanoparticles was published in 2005 (“Microemulsion-Templated Synthesis of Carbon Nanotube-Supported Pd and Rh Nanoparticles for Catalytic Applications”, *Journal of the American Chemical Society* **2005**, *127*, 17174-17175).

The carbon nanotube-supported Pd nanoparticles are very effective for catalytic conversion of organic nitro groups to amino groups in the presence of hydrogen gas. For example, conversion of nitrobenzene to aniline in the vapor phase can be accomplished in one minute at room temperature in the presence of hydrogen gas using the CNT-supported Pd nanoparticles as catalyst. This rapid nitro to amino conversion may have important applications for detection of nitro explosives. One of the current methods for detecting nitro-aromatic explosives such as TNT (2,4,6-trinitrotoluene) and its impurity 2,4-DNT (2,4-dinitrotoluene) is by means of quenching fluorescent polymers caused by the nitro-aromatic compounds. This method is rapid and sensitive but is not selective for detecting different nitro-aromatic compounds. If the nitro aromatic compounds can be converted to aromatic amines, the molecular electronic transitions would allow for relatively intense fluorescence of the aromatic amines. The main reason for the increase in the fluorescence of aromatic amines is due to a $\pi \rightarrow \pi^*$ transition. This transition occurs because the $-\text{NH}_2$ substituent is a strong electron-donating group, therefore providing electrons to the benzene ring and subsequently allowing for radiative decay. It can be considered that the $-\text{NO}_2$ substituent involves an $n \rightarrow \pi^*$ transition (from selection rules, forbids radiative decay) and that the $-\text{NH}_2$ substituent involves a $\pi \rightarrow \pi^*$ transition. The highly sensitive and selective nature of fluorescence makes it ideal for detecting and identifying explosive vapors.

Real world detection of TNT often occurs through the detection of its impurity 2,4-DNT due to its higher vapor pressure relative to TNT. We have demonstrated that the reduction of 2,4-dinitrotoluene (2,4-DNT) vapor to 2,4-diaminotoluene (2,4-DAT) could be accomplished by hydrogenation at room temperature using carbon nanotube-supported palladium nanoparticles (CNT-Pd) as the catalyst according to the following reaction.



In our initial experiments, the CNT-Pd nanoparticle catalyst was packed in a stainless steel tubing (2 mm i.d. and 13 cm in length) and hydrogen gas carrying saturated 2,4-DNT vapor in air was forced through the tubing at a flow rate of 0.7 L per minute. The exit gas was bubbled through an ethanol solution to collect the hydrogenation product for fluorescence measurements. Using this crude small channel gas flow reactor, we were able to detect the presence of 2,4-DAT in the ethanol solution after one minute of reaction by fluorescence using a Spex FluoroMax-3TM spectrometer (HORIBA Jobin Yvon) with a 150 watt Xe arc lamp. The fluorescence intensity of the ethanol solution was found to increase with reaction time because of accumulation of 2,4-DAT. Without the nanoparticle catalyst no conversion of 2,4-DNT was observed. To increase the fluorescence yield, commercially available amino-fluorescence-enhancing reagents such as fluorescamine can be used. These reagents do not fluoresce themselves, but, when bonded to amino groups, can significantly increase fluorescence yields of the amino compounds. The fluorescence tends to shift farther to the red, which could decrease background from impurities. Our preliminary experiments also showed that in the presence of fluorescamine, 2,4-DAT could be detected down to 10^{-12} M (mol/L) in ethanol using the FluoroMax-3TM spectrometer. The fluorescence detection limit could be further lowered using several approaches including using a small laser (or blue LED) for excitation and concentration of the amino product. The results of this study were published in *Applied Spectroscopy* last year (“Fluorescence of Aromatic Amines and Their Fluorescamine Directives for Detection of Explosive Vapors”, *Applied Spectroscopy* 2006, 60, 958-963).

We have also demonstrated methods to increase selectivity of explosive detection using fluorescence; this includes synchronous luminescence and derivative spectroscopy with appropriate smoothing. By implementing synchronous luminescence and derivative spectroscopy, we were able to resolve the reduction products of one major TNT-based explosive compound, 2,4-diaminotoluene, and the reduction products of other minor TNT-based explosives

in a mixture. Our approach appears promising for developing a method for rapid, sensitive, and selective detection, with the discrimination necessary to distinguish among various explosives. This study was also published in *Applied Spectroscopy* ("Increasing Selectivity for TNT-based Explosive Detection by Synchronous Luminescence and Derivative Spectroscopy with Quantum Yields of Selected Aromatic Amines", *Applied Spectroscopy* 2007, 61, 68-73. Figure 10 shows the second derivative synchronous luminescence spectrum of a mixture of 4 aromatic amino compounds which are likely hydrogenation products present in a TNT-based explosive mixture. The ability of the fluorescence technique to distinguish the hydrogenation products from the explosive mixture is obvious as illustrated in Figure 10. Research in rapid hydrogen reduction of other explosive vapors including tagging compounds using the nanoparticle catalysts developed by this project and their fluorescence detection is currently in progress. A proposal has recently been submitted to the National Science Foundation requesting support for continuation of the explosive detection research.

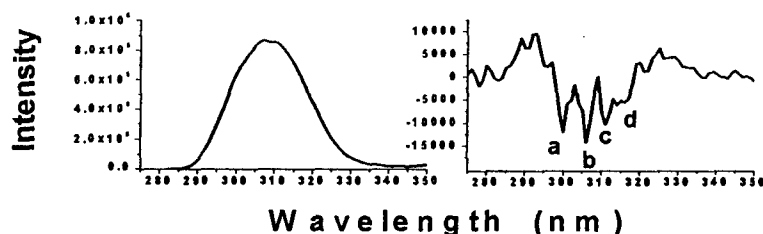


Figure 10. Left is synchronous luminescence (SL) spectrum of a four-component mixture. Overlapping of fluorescence peaks result in a broad single peak located at 310 nm. Right is the 2nd derivative of SL on the left. Four peaks (a) 300 nm (b) 305 nm (c) 311 nm (d) 316 nm corresponding to 2,6-DAT, *o*-toluidine, 2,4-DAT, and *p*-toluidine, respectively.

6. References

1. Ji, M.; Chen, X.; Wai, C.M., *J. Amer. Chem. Soc.* **1999**, *121*, 2631.
2. Phelps, C.L.; Smart, N.G.; Wai, C.M., *J. Chem. Edu.* **1990**, *12*, 1163-1168.
3. Giddings, J.C., *Science* **1968**, 67-73.
4. Hiderbrand, J.H., *J. Amer. Chem. Soc.* **1919**, *41*, 1067.
5. Laintz, K.E.; Wai, C.M.; Yonker, C.R.; Smith, R.D., *J. Supercritical Fluid* **1991**, *4*, 194-198.
6. National Institute of Standards and Technology, *Thermophysical Properties of Fluid System*, can be found under <http://webbook.nist.gov/chemistry/fluid>.
7. Ohde, H.; Ohde, M.; Kim, H.; Wai, C.M., *Nano Letters* **2002**, *2*, 721-724.
8. Ye, X.R.; Lin, Y.; Wang, C.; Wai, C.M. *Adv. Mater.* **2003**, *25*, 316-319.
9. Ohde, H.; Kramer, S.J.; Moore, S.; Wai, C.M., *Chem. Mater.* **2004**, *81*, 207-213.
10. O'Neil, A.; Watkins, J.J., *MRS Bulletin* **2005**, *30*, 967-975.
11. Serp, P.; Corriás, M.; Kalck, P., *Applied Catalysis A: General* **2003**, *253*, 337-358.
12. Steigerwalt, E.S.; Deluga, G.A.; Cliffel, D.E.; Lukehart, C.M., *J. Physl Chem. B* **2001**, *105*, 8097-8101.
13. Swager, T.M., in *Electronic noses and Sensors for the Detection of Explosives*, J.W. Gardner and J. Yinon, Eds., Kluwer Academic Publishers, Boston, 2004.
14. Rose, A.; Zhu, A.; Madigan, C.F.; Swager, T.M.; Bulovic, V., *Nature* **2005**, *434*, 876-879.

7. Publications Derived from this Project

1. Carlos A. Fernandez, Chien M. Wai, "A Simple and Rapid Method of Synthesizing 2D and 3D Arrays of Gold Nanoparticles", *J. Nanosci. Nanotech.* **2006**, *6*, 669-674.
2. Carlos A. Fernandez, Chien M. Wai, "Continuous Tuning of Silver nanoparticle Size in a Water-in-CO₂ Microemulsion", *Small* **2006**, *2*, 1266-1269.
3. Carlos A. Fernandez, Chien M. Wai, "Continuous Tuning of Cds and ZnS Nanoparticle Size in a Water-in-CO₂ Carbon Dioxide Microemulsion", *Chem.- A European J.* **2007**, in press.
4. Joanna S. Wang, Horng-Bin Pan, Chien M. Wai, "Deposition of Metal Nanoparticles on Carbon Nanotubes via Hexane Modified Water-in-CO₂ Microemulsion at Room Temperature", *J. Nanosci. Nanotech.*, **2006**, *6*, 2025-2030.
5. Yuehe Lin, Xiaoli Cui, Clive Yen, Chien M. Wai, "PtRu/Carbon Nanotube Nanocomposite Synthesized in Supercritical Fluid: A Novel Electrocatalyst for Direct Methanol Fuel Cell", *Langmuir* **2005**, *21*, 11474-11479.
6. Byunghoon Yoon, Chien M. Wai, "Microemulsion-templated Synthesis of Carbon Nanotube-supported Pd and Rh Nanoparticles for Catalytic Applications", *J. Amer. Chem. Soc.* **2005**, *127*, 17174-17175.
7. Horng-Bin Pan, Clive H. Yen, Byunghoon Yoon, Masaki Sato, Chien M. Wai, "Recyclable and Ligandless Suzuki Coupling Catalyzed by Carbon Nanotube-Supported Palladium Nanoparticles Synthesized in Supercritical Fluid", *Syn. Commun.* **2006**, *36*, 3473-3478.
8. DeLyle Eastwood, Carlos Fernandez, Byunghoon Yoon, Chrystal N. Sheaff, Chien M. Wai, "Fluorescence of Aromatic Amines and Their Fluorescamine Derivatives for Detection of Explosive Vapors", *Appl. Spectrsc.*, **2006**, *60*, 958-963.
9. Chrystal N. Sheaff, DeLyle Eastwood, Chien M. Wai, "Increasing Selectivity for TNT-Based Explosive Detection by Synchronous Luminescence and Derivative Spectroscopy with Quantum Yields of Selected Aromatic Amines", *Appl. Spectrosc.* **2007**, *61*, 68-73.

8. Scientific Personnel

Chien M. Wai – Principal investigator

DeLyle Eastwood – Post-doctoral Research Fellow

Joanna S. Wang – Post-doctoral Research Fellow

Carlos Fernandez – Chemistry graduate student, completed Ph.D. in August 2006

Dissertation Title: "Synthesis and Characterization of 2D and 3D Arrays of Metal and Semiconductor Nanoparticles of Tunable Sizes in Supercritical Carbon Dioxide"

Department of Chemistry, University of Idaho, Moscow, Idaho 83844

Byunghoon Yoon – Chemistry graduate student, completed Ph.D. in January 2007

Dissertation Title: "Synthesis of Matrix-Supported Metal Nanoparticles and Catalysis Applications", Department of Chemistry, University of Idaho, Moscow, Idaho 83844

Clive Yen – Chemistry graduate student, completed Ph.D. degree in January 2007

Dissertation Title: "Supercritical Fluid Synthesis and Applications of Carbon Nanotube-Supported Nanoparticle Catalysts", Department of Chemistry, University of Idaho, Moscow, Idaho 83844

9. Inventions - None

Appendix

Reprints of the publications derived from this project are attached in the Appendix.



A Simple and Rapid Method of Making 2D and 3D Arrays of Gold Nanoparticles

Carlos A. Fernandez and Chien W. Wai*

Department of Chemistry, University of Idaho, Moscow, ID 83844, USA

Monodispersive gold nanoparticles can be synthesized by a dropwise addition of a reducing agent microemulsion to a gold ion microemulsion followed by immediate stabilization with 1-decanethiol. No size-selective precipitations or digestive ripening procedures are necessary. There is no need for metal functionalization of the surfactant AOT. Gold nanoparticles with an average size of 3.8 nm and a relative size dispersion of 5.4% were observed using *n*-heptane as a solvent. It seems possible to adjust the nanoparticle size by small changes in the carbon chain length of the solvent. Self-assembled 2D and 3D arrays of gold nanoparticles with adjustable sizes have been obtained on carbon-coated copper grids and on a silicon wafer. The arrays have good crystallinity as evidenced by the external morphology and transmission electron diffraction results. The size of the gold nanoparticle 3D arrays depends on the immersion time and can be greater than 15 μ m. This approach could be used to synthesize other noble metal nanoparticle arrays that may lead to new materials for electronic and photonic applications.

Keywords: Gold Nanoparticles, Microemulsions, 2D, 3D Arrays.

1. INTRODUCTION

Self-assembled nanoparticle arrays and their electronic and photonic properties represent an area of physics that has rapidly progressed in the past decade. The importance of gold nanoparticles for areas ranging from electron microscopy (contrast agents),¹ analysis (chemical and biological sensors),^{2–5} electronics (single-electron transistors, electrical connects),^{6,7} materials (dyes, conductive coatings),^{8,9} and catalysis (CO oxidation on Au/TiO₂ composites),^{10,11} is well documented in the literature. Several research groups have produced gold nanoparticle arrays, but none with well-defined morphologies larger than about one micron. Kimura et al.,¹² found a way to make these arrays, but the procedure is complicated and very time-consuming, taking at least six days in order to obtain the final crystals. Micrometer-sized gold nanoparticle arrays have been synthesized by Klabunde et al.,^{13,14} but the procedure is tedious because all solvents must be argon-purged for 4 h, and the reactions have to be carried out under an argon atmosphere. Besides that, a ripening procedure consisting of an extra addition of the protecting agent (dodecanethiol) and a 90 minute reflux with toluene (under an inert atmosphere) needs to be performed,

in order to improve the highly polydisperse particles obtained by these reactions.

In this report, we present a simple, rapid and reproducible method for synthesizing organosulfur-protected, monodisperse gold nanoparticles and the formation of 2D arrays and 3D macrocrystals of tunable size. Water-in-oil microemulsions are used to prepare the nanoparticles; the size of the micelles seems to be determined by the solvent nature rather than by the water-to-surfactant (sodium di-2-ethylhexylsulfosuccinate) ratio, or *W* value,¹⁵ used in its preparation. With a dropwise introduction of the reducing agent microemulsion to the gold ion microemulsion, reproducible monodisperse gold nanoparticles of well-defined size and shape can be synthesized. Neither size-selective precipitation nor digestive ripening is necessary and there is no need of previous metal functionalization of the AOT. The experimental conditions for synthesizing monodisperse Au nanoparticles and the procedures of making 2D and 3D arrays of the protected Au nanoparticles are described in this paper.

2. EXPERIMENTAL DETAILS

2.1. Reagents

All chemicals were purchased and used without any further purification. Sodium cyanoborohydride 95%, sodium

*Author to whom correspondence should be addressed.

di-2-ethylhexylsulfosuccinate (AOT) and 1-decanethiol were purchased from Aldrich. Tetrachloroauric acid was obtained from Fisher Scientific. HPLC grade hexanes and *n*-heptane were obtained from Fisher Chemicals. Pharmco ethanol (200 proof) was used for the washing procedure.

2.2. Preparation of Monodispersive Gold Nanoparticles

In a typical preparation procedure, 1 mL of water-in-hexanes or water-in-heptane microemulsion containing NaCNBH_3 solution ($W = 12$) was added drop-wise (1 minute total time) to 1 mL of stirring Au^{+3} containing water-in-hexanes or water-in-heptane microemulsion with the same W value. The molar ratios of reducing agent: Au^{+3} ion used were 2.7 : 1 and 1 : 1 with an initial (overall) concentration of Au^{+3} ions of 3.2×10^{-3} M in all cases. As the reducing agent was added, the color changes from yellow to orange to brownish-blue and finally to dark purplish-red. Immediately after the last of the reducing agent was added, 40 μL of decanethiol was added. It is well known that there is a selective reaction of the decanethiol on the surface of gold particles due to the strong affinity of the SH head-group for the noble metal.¹⁶ The solution was stirred for one hour. A large amount of precipitate was observed when a 1 : 1 reducing agent: gold ion molar ratio was utilized. Ethanol was used to wash the nanoparticles' microemulsion. This procedure was carried out in triplicate. The nanoparticles were finally air-dried. The protected Au nanoparticles can be dispersed in non-polar solvents such as hexanes, isooctane or chloroform. The solutions are stable for months, showing no observable change in color or UV-VIS absorption spectra.

2.3. Preparation of Gold Nanoparticle Arrays

Solutions used to form nanoparticle arrays were prepared by sonicating the dried nanoparticles in hexanes for about 10 seconds. Two-dimensional nanoparticle arrays were prepared by placing one drop of this solution onto a carbon-coated copper grid. Three dimensional nanoparticle arrays were prepared by immersing a grid in 600 μL of solution for one to three hours. In all cases, the grids were dried under ambient conditions. TEM images were obtained with a JEOL 1200 EX II transmission electron microscope at an accelerating voltage of 120 kV. Scanning electron microscope (SEM) photographs were taken with a LEO Supra 35 VP FESEM. The nanoparticles' average size and standard deviation, as well as their average separation distance, were determined from the TEM data of the monolayers and using MathLabTM software. UV-VIS absorption spectra of the gold nanoparticle solutions were recorded on a SI440 CCD-array spectrophotometer from Spectral Instruments Inc.

3. RESULTS AND DISCUSSION

3.1. UV-Vis Characterization of Gold Nanoparticles

The UV-VIS spectrum (Fig. 1) shows a typical surface plasmon absorption band at 520 nm for the protected Au nanoparticles in the microemulsion. No obvious changes in color, UV-VIS spectrum or particle size (ca. 4 nm) were detected upon prolonged storage (3 months) of the gold nanoparticle solutions.

3.2. TEM and SEM Characterization of Gold Nanoparticle Arrays

According to Fletcher¹⁷ and Lopez-Quintela et al.,^{18,19} the material exchange during micelles' collisions can take place by the formation of an encounter-pair followed by either the opening of a channel or by fusing the two micelles and forming a fused dimer. Most of the results reported in the literature assume exchange through the fused dimer, and few reports discuss exchange through the encounter pair. In fact, exchange through the encounter pair should be difficult unless the surfactant film is disrupted, as it is in the case of some cosurfactants like benzylalcohol.

There are two mechanisms by which growing of nanoparticles occur, autocatalysis and Ostwald ripening.¹⁹ In the first mechanism, the reaction inside the microemulsion droplet is catalyzed by the surface of an existing aggregate. In the second case, growing occurs by condensation of material, coming from the smallest particles. These particles are more abundant at the nucleation process and at the beginning of the growth process and are more likely to collide and aggregate than the larger nanoparticles. As a result, a small nanoparticle formed inside a droplet can be transferred to another one forming a bigger particle, depending on the size ratio between the

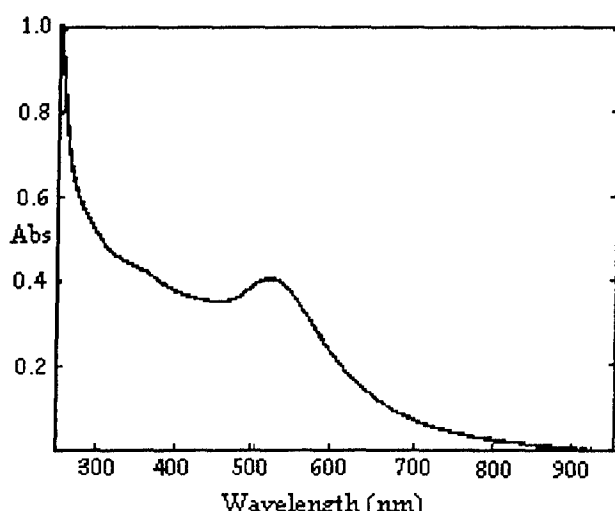


Fig. 1. Typical UV-VIS spectrum of gold nanoparticles (4 nm size) stabilized by a water-in-hexane microemulsion.

small particle and the interdroplet channel. In our experiments, by using a dropwise addition of the reducing-agent-containing microemulsion to the microemulsion containing Au^{3+} the concentration of the reducing agent should always be lower than that of the Au^{3+} in the system, except just at the end. Growing by autocatalysis should then be minimized due to the fact that one of the reactants (the reducing agent) is consumed right after each drop is added. For this non-stoichiometric dropwise method, Ostwald-ripening would be the main mechanism for particle growth, which would be inhibited and limited by the droplet intercollision channel size. This channel size depends on the W value we select. Therefore, further growth and size dispersion would be limited due to the following two factors: the limiting channel size and the immediate stabilization of the nanoparticles by the protecting agent added right after the reducing agent microemulsion is introduced.

In the reported microemulsion methods, a reducing agent microemulsion solution or an aqueous solution of reducing agent is added at once to a metal-ion-containing microemulsion solution.²⁰⁻²² In these methods, both autocatalysis, and Ostwald-ripening can occur and the size and size distribution of the nanoparticles are less restricted. Therefore AOT functionalization, time-consuming size-selective precipitation or digestive ripening procedures are necessary in order to obtain gold nanoparticles with narrow size distributions.²⁰ By simply limiting the particle growth to the Ostwald ripening mechanism as demonstrated in this study, it is possible to obtain Au nanoparticles with smaller sizes and narrower size distributions than those obtained by the methods reported in the literature.

Figure 2 shows a typical transmission electron microscope (TEM) photograph obtained in our study of a 3D array formation of the thiol-protected gold nanoparticles obtained from water-in-hexanes microemulsions using a molar ratio of the reducing agent : gold ion = 2.7 : 1. These superlattices were obtained by immersing a carbon-coated copper grid in the Au nanoparticles' solution for an hour and then allowing it to evaporate at room temperature.

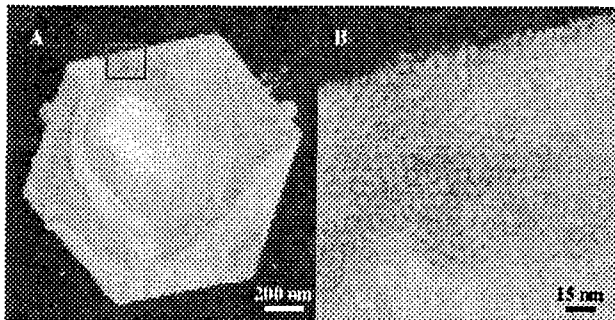


Fig. 2. TEM image of a 3D array of gold nanoparticles of 4 nm average size, immersion time: 1 hour (A), and a magnification-marked area (B). The white areas correspond to extra layers of the Au nanoparticles due to the nonhomogeneous solvent evaporation.

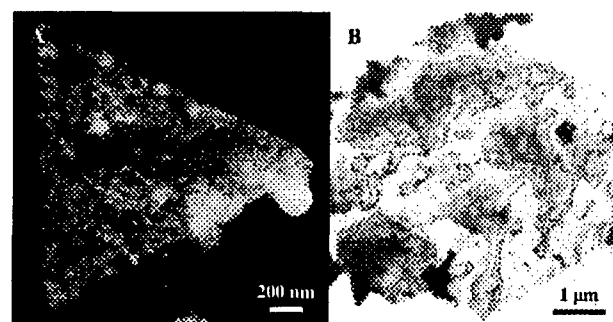


Fig. 3. (A) TEM image of a 3D array of gold nanoparticles of 4 nm average size, in this case with a triangular shape. Immersion time: 1 hour (B) Six μm -sized crystals of gold nanoparticles were obtained by immersing a carbon-coated grid in the protected nanoparticles' hexanes solution for 3 h. The "coffee rings" areas correspond to extra layers of particles and are due to the non-uniform solvent evaporation.

Several macrocrystals (3D arrays) of well-defined hexagonal geometric figures were formed with sizes larger than a micrometer. Figure 3A shows another gold nanoparticles' superlattice with a triangular shape and with a similar size to the one shown in Figure 1. The contours of these crystals are well defined. When the immersion time of the grids in the nanoparticles' solution was longer (e.g., 3 h), crystals of several micrometers in size could be formed (Fig. 3B). This suggested that a large concentration of the protected Au nanoparticles was still present in the solution and would continue to interact with the 3D array resulting in further growth of the crystals. Similar results were obtained when a silicon dioxide coated Si-wafer was exposed to the nanoparticle solutions. Figure 4 shows scanning electron micrographs (SEM) of gold nanoparticle superlattices formed on the silicon dioxide wafer for immersion times of 1 hour (4A) and 3 hours (4B). The size of the arrays was as large as 16 μm in cross section and 4 to 6 μm in thickness. Various shapes can be developed when the growth rates in different directions of the crystals are different. In general, the growth rate in the direction normal to the top surface of the plate crystals is slower than those in other directions.

Taleb et al.²⁰ have mentioned that formation of 3D lattices does not need external forces and is due to an

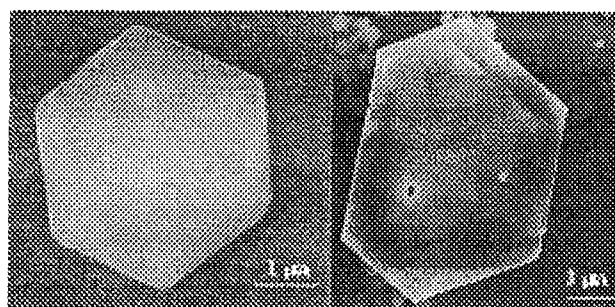


Fig. 4. SEM images of individual gold crystals formed by 4 nm size gold nanoparticles in a SiO_2 coated wafer with immersion times of 1 hour (A) and 3 hours (B).

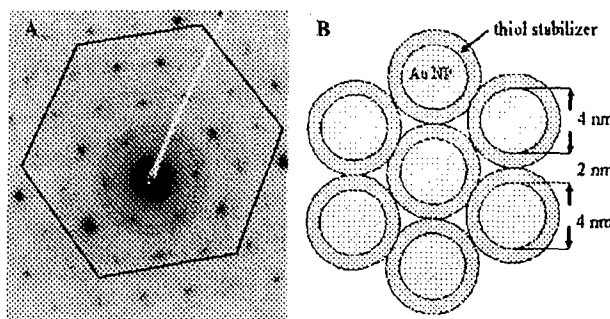


Fig. 5. (A) Transmission electron diffraction pattern of an individual gold crystal formed by 4 nm size gold nanoparticles. (B) Stacking model of Au nanoparticles (treated as hard spheres). Distances calculated from TEM data.

equilibrium between the van der Waals attraction forces and the repulsive hard-sphere interactions. Both forces are isotropic and the array is achieved by increasing the density of the "pseudocrystal," which tends to have a close-packed structure. Transmission electron diffraction (TED) measurements were carried out on some samples. All of the TED patterns recorded from several zones of randomly selected crystals have the same pattern and similar inter-spot distance. The crystals were tilted 20° and the diffraction pattern did not change. A representative TED photograph of these 3D arrays is shown in Figure 5A, exhibiting a 6-fold symmetric arrangement of sharp diffraction spots. Clearly, the hexagonal pattern indicates a 6-fold projected symmetry in the colloidal crystals. Three structures, face-centered-cubic (fcc), body-centered-cubic (bcc), and hexagonal close packing (hcp) exhibit this type of symmetry, therefore the most direct way to distinguish a hexagonal-close-packing system from a cubic-close-packing system is to record the TED from at least two zone axes.¹² Even though more information is needed to conclude what kind of lattice these crystals represent, it is worth mentioning that the crystals obtained by Kimura et al.¹² had similar TED patterns. They combined this information with X-ray diffraction (XRD) and transmission electron diffraction (TED) data to conclude that the Au nanoparticles were arranged in a very long-range translational ordering, forming a hexagonal close-packed superlattice structure. The monodispersive Au nanoparticles obtained here were approximately spherical with an average diameter of 4.0 nm and a particle size distribution of 18%. (The picture of the monolayers used for this calculation is not shown.) The average distance between two particle centers was 6.5 ± 0.7 nm. The particles' average separation was 2.0 ± 0.5 nm, which was similar (taking into account the associated distribution) to the calculated length (1.55 nm) of the alkanethiol, using the following empirical Eq. (1):²³

$$L(\text{nm}) = 0.25 + 0.127n \quad (1)$$

where n is the number of CH_2 groups ($n = 10$). The similarity between the average interparticle distance and the

length of the alkyl chain suggest that the alkyl chains have an all-trans conformation. In this way, close-packing of alkyl chains into an all-trans conformation is achieved by intercalation or interpenetration of individual chains or domains of chains.²⁰ Figure 5B is a representation of the data discussed above in a stacking model of gold nanoparticles treated as hard spheres. It should be noted that in order to form these monodispersed nanoparticles, neither digestive ripening nor size-selective precipitation was used in our procedure. As explained above, dropwise addition of the reducing-agent-containing microemulsion to the gold ion microemulsion appears to provide a simple way to avoid these steps.

In the case where a 1 : 1 reducing agent : gold ion molar ratio was used in the preparation of Au nanoparticles in hexanes, 2D arrays of Au nanoparticles with narrower size distributions were obtained. The average Au particle size was in this case 4.7 nm with a RSD value of 7.5%. The average distance between the nanoparticle centers was calculated to be 6.0 ± 0.5 nm, while the average distance between particles' edges was 2.0 ± 0.3 nm.

Figure 6 shows two different zones of the nanoparticle monolayers formed under the conditions last described. When using the same NaCNBH_3 : Au^{+3} molar ratio, but in water-in-heptane microemulsions instead of in hexanes, we observed 2D arrays of Au nanoparticles with an average size of 3.8 nm and a relative size dispersion of 5.4%.

Figure 7A shows 2D gold arrays formed when *n*-heptane was used as a solvent. Magnifications of two different zones of the 2D Au arrays are shown in Figures 7B and 7C. The average distance between the particle centers was 5.7 ± 0.4 nm, while the distances between the particles' edges were similar to that obtained in water-in-hexanes microemulsions (1.7 ± 0.4 nm). In both solvents, the particle separation was roughly similar to the calculated length (1.55 nm) of the alkanethiol. The results appear to suggest that, under similar conditions, a more viscous solvent (*n*-heptane) tends to decrease the nanoparticle size, the size distribution and the distance between centers, compared with a less viscous solvent (hexanes).

Precipitation of the Au particles was observed when the molar ratio of reducing agent : gold ion was 1 : 1. This

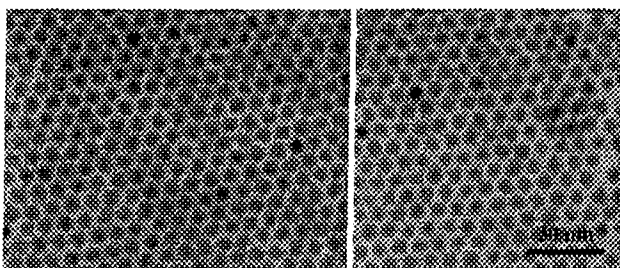


Fig. 6. TEM photographs of two different zones of a gold nanoparticle 2D-array with a particle mean size of 4.7 nm, obtained using water-in-hexanes microemulsions and a NaCNBH_3 : gold ion molar ratio of 1.03 : 1. The scale bar applies to both figures.

small particle and the interdroplet channel. In our experiments, by using a dropwise addition of the reducing-agent-containing microemulsion to the microemulsion containing Au^{3+} the concentration of the reducing agent should always be lower than that of the Au^{3+} in the system, except just at the end. Growing by autocatalysis should then be minimized due to the fact that one of the reactants (the reducing agent) is consumed right after each drop is added. For this non-stoichiometric dropwise method, Ostwald-ripening would be the main mechanism for particle growth, which would be inhibited and limited by the droplet intercollision channel size. This channel size depends on the W value we select. Therefore, further growth and size dispersion would be limited due to the following two factors: the limiting channel size and the immediate stabilization of the nanoparticles by the protecting agent added right after the reducing agent microemulsion is introduced.

In the reported microemulsion methods, a reducing agent microemulsion solution or an aqueous solution of reducing agent is added at once to a metal-ion-containing microemulsion solution.²⁰⁻²² In these methods, both autocatalysis, and Ostwald-ripening can occur and the size and size distribution of the nanoparticles are less restricted. Therefore AOT functionalization, time-consuming size-selective precipitation or digestive ripening procedures are necessary in order to obtain gold nanoparticles with narrow size distributions.²⁰ By simply limiting the particle growth to the Ostwald ripening mechanism as demonstrated in this study, it is possible to obtain Au nanoparticles with smaller sizes and narrower size distributions than those obtained by the methods reported in the literature.

Figure 2 shows a typical transmission electron microscope (TEM) photograph obtained in our study of a 3D array formation of the thiol-protected gold nanoparticles obtained from water-in-hexanes microemulsion's using a molar ratio of the reducing agent : gold ion = 2.7:1. These superlattices were obtained by immersing a carbon-coated copper grid in the Au nanoparticles' solution for an hour and then allowing it to evaporate at room temperature.

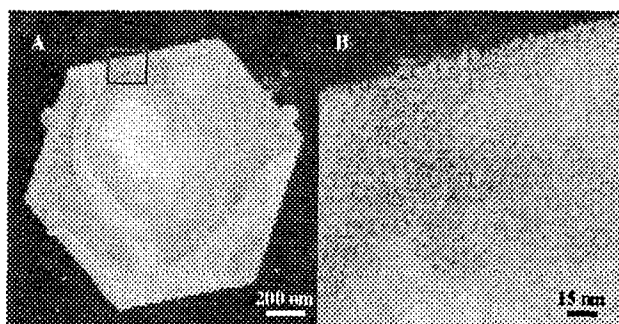


Fig. 2. TEM image of a 3D array of gold nanoparticles of 4 nm average size, immersion time: 1 hour (A), and a magnification-marked area (B). The white areas correspond to extra layers of the Au nanoparticles due to the nonhomogeneous solvent evaporation.

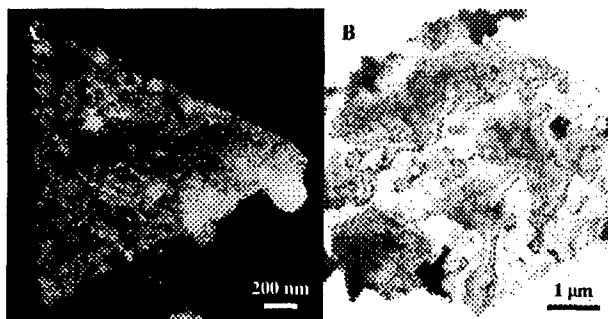


Fig. 3. (A) TEM image of a 3D array of gold nanoparticles of 4 nm average size, in this case with a triangular shape. Immersion time: 1 hour. (B) Six μm -sized crystals of gold nanoparticles were obtained by immersing a carbon-coated grid in the protected nanoparticles' hexanes solution for 3 h. The "coffee rings" areas correspond to extra layers of particles and are due to the non-uniform solvent evaporation.

Several macrocrystals (3D arrays) of well-defined hexagonal geometric figures were formed with sizes larger than a micrometer. Figure 3A shows another gold nanoparticles' superlattice with a triangular shape and with a similar size to the one shown in Figure 1. The contours of these crystals are well defined. When the immersion time of the grids in the nanoparticles' solution was longer (e.g., 3 h), crystals of several micrometers in size could be formed (Fig. 3B). This suggested that a large concentration of the protected Au nanoparticles was still present in the solution and would continue to interact with the 3D array resulting in further growth of the crystals. Similar results were obtained when a silicon dioxide coated Si-wafer was exposed to the nanoparticle solutions. Figure 4 shows scanning electron micrographs (SEM) of gold nanoparticle superlattices formed on the silicon dioxide wafer for immersion times of 1 hour (4A) and 3 hours (4B). The size of the arrays was as large as 16 μm in cross section and 4 to 6 μm in thickness. Various shapes can be developed when the growth rates in different directions of the crystals are different. In general, the growth rate in the direction normal to the top surface of the plate crystals is slower than those in other directions.

Taleb et al.²⁰ have mentioned that formation of 3D lattices does not need external forces and is due to an

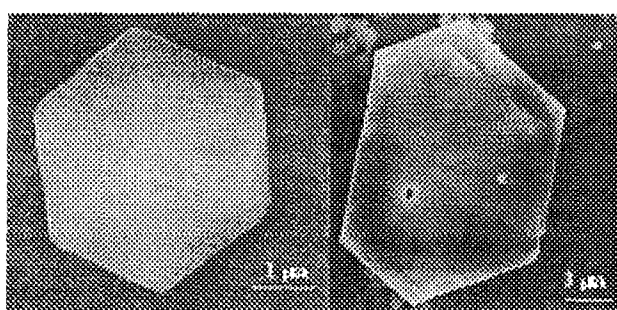


Fig. 4. SEM images of individual gold crystals formed by 4 nm size gold nanoparticles in a SiO_2 coated wafer with immersion times of 1 hour (A) and 3 hours (B).

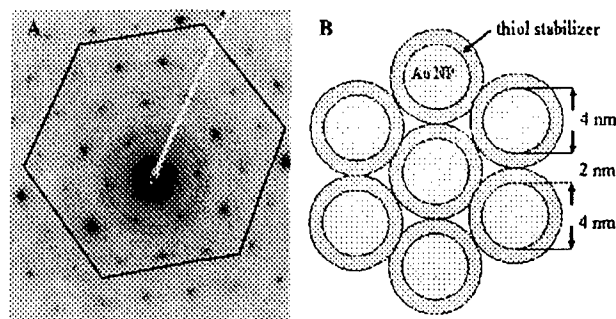


Fig. 5. (A) Transmission electron diffraction pattern of an individual gold crystal formed by 4 nm size gold nanoparticles. (B) Stacking model of Au nanoparticles (treated as hard spheres). Distances calculated from TEM data.

equilibrium between the van der Waals attraction forces and the repulsive hard-sphere interactions. Both forces are isotropic and the array is achieved by increasing the density of the "pseudocrystal," which tends to have a close-packed structure. Transmission electron diffraction (TED) measurements were carried out on some samples. All of the TED patterns recorded from several zones of randomly selected crystals have the same pattern and similar inter-spot distance. The crystals were tilted 20° and the diffraction pattern did not change. A representative TED photograph of these 3D arrays is shown in Figure 5A, exhibiting a 6-fold symmetric arrangement of sharp diffraction spots. Clearly, the hexagonal pattern indicates a 6-fold projected symmetry in the colloidal crystals. Three structures, face-centered-cubic (fcc), body-centered-cubic (bcc), and hexagonal close packing (hcp) exhibit this type of symmetry, therefore the most direct way to distinguish a hexagonal-close-packing system from a cubic-close-packing system is to record the TED from at least two zone axes.¹² Even though more information is needed to conclude what kind of lattice these crystals represent, it is worth mentioning that the crystals obtained by Kimura et al.¹² had similar TED patterns. They combined this information with X-ray diffraction (XRD) and transmission electron diffraction (TED) data to conclude that the Au nanoparticles were arranged in a very long-range translational ordering, forming a hexagonal close-packed superlattice structure. The monodispersive Au nanoparticles obtained here were approximately spherical with an average diameter of 4.0 nm and a particle size distribution of 18%. (The picture of the monolayers used for this calculation is not shown.) The average distance between two particle centers was 6.5 ± 0.7 nm. The particles' average separation was 2.0 ± 0.5 nm, which was similar (taking into account the associated distribution) to the calculated length (1.55 nm) of the alkanethiol, using the following empirical Eq. (1).²³

$$L(\text{nm}) = 0.25 + 0.127n \quad (1)$$

where n is the number of CH_2 groups ($n = 10$). The similarity between the average interparticle distance and the

length of the alkyl chain suggest that the alkyl chains have an all-trans conformation. In this way, close-packing of alkyl chains into an all-trans conformation is achieved by intercalation or interpenetration of individual chains or domains of chains.²⁰ Figure 5B is a representation of the data discussed above in a stacking model of gold nanoparticles treated as hard spheres. It should be noted that in order to form these monodispersed nanoparticles, neither digestive ripening nor size-selective precipitation was used in our procedure. As explained above, dropwise addition of the reducing-agent-containing microemulsion to the gold ion microemulsion appears to provide a simple way to avoid these steps.

In the case where a 1 : 1 reducing agent : gold ion molar ratio was used in the preparation of Au nanoparticles in hexanes, 2D arrays of Au nanoparticles with narrower size distributions were obtained. The average Au particle size was in this case 4.7 nm with a RSD value of 7.5%. The average distance between the nanoparticle centers was calculated to be 6.0 ± 0.5 nm, while the average distance between particles' edges was 2.0 ± 0.3 nm. Figure 6 shows two different zones of the nanoparticle monolayers formed under the conditions last described. When using the same $\text{NaCNBH}_3 : \text{Au}^{+3}$ molar ratio, but in water-in-heptane microemulsions instead of in hexanes, we observed 2D arrays of Au nanoparticles with an average size of 3.8 nm and a relative size dispersion of 5.4%.

Figure 7A shows 2D gold arrays formed when *n*-heptane was used as a solvent. Magnifications of two different zones of the 2D Au arrays are shown in Figures 7B and 7C. The average distance between the particle centers was 5.7 ± 0.4 nm, while the distances between the particles' edges were similar to that obtained in water-in-hexanes microemulsions (1.7 ± 0.4 nm). In both solvents, the particle separation was roughly similar to the calculated length (1.55 nm) of the alkanethiol. The results appear to suggest that, under similar conditions, a more viscous solvent (*n*-heptane) tends to decrease the nanoparticle size, the size distribution and the distance between centers, compared with a less viscous solvent (hexanes).

Precipitation of the Au particles was observed when the molar ratio of reducing agent : gold ion was 1 : 1. This

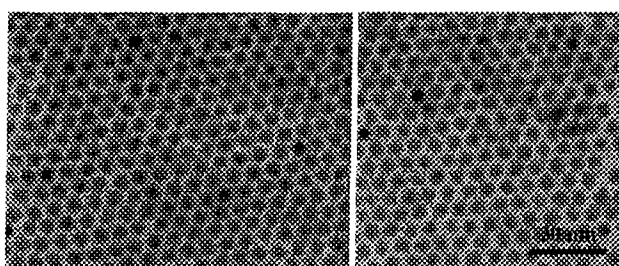


Fig. 6. TEM photographs of two different zones of a gold nanoparticle 2D-array with a particle mean size of 4.7 nm, obtained using water-in-hexanes microemulsions and a $\text{NaCNBH}_3 : \text{gold ion}$ molar ratio of 1.03 : 1. The scale bar applies to both figures.

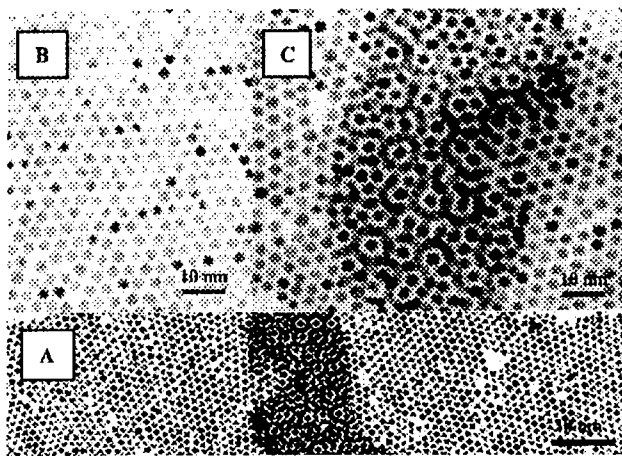


Fig. 7. (A) 2D arrays of gold nanoparticles, 3.8 nm in size obtained using water-in-heptane's microemulsions and a NaCNBH_3 : gold ion molar ratio of 1 : 1. (B) and (C) are magnifications of two different areas of picture A. In picture C we can see that a double layer of particles has been formed.

phenomenon might be related to the narrower particle size distribution calculated from the micrographs compared to the one obtained when a molar ratio of 2.7 : 1 was utilized. Analysis on the precipitate, obtained from systems when lower concentrations of reducing agent in the microemulsions were used, indicated that gold was the main component (97%), showing a polycrystalline structure (data not shown). Our initial hypothesis that charged nanoparticles (due to probably deficient concentration of NaCNBH_3) would lead to a salt formation with counter-ions coming from reaction byproducts was overruled when analysis on the precipitate showed absence of boron, sodium and chlorine. The mechanism of this precipitate formation remains unclear.

For the observed variation in particle size when solvents of slightly different viscosity were used in the preparation of the microemulsions, a possible explanation could be given by referring to the kinetics studies done by Fletcher et al.¹⁷ and by Lopez-Quintela et al.²⁴ Fletcher et al. predicted that the mechanism of material interchange between AOT-stabilized droplets in microemulsion systems for fast reactions is via a fused dimer. The exchange constant of materials inside the fused dimer during collision, K_{ex} , is the rate determinant step, not the collision frequency which is related to the viscosity of the solvent. He also has shown that K_{ex} increases with increasing the carbon number in the solvent and decreases with cyclization, chain-branching and lack of saturation of the hydrocarbon solvent, at a fixed temperature. With this in mind, we should expect an increment in the final particle size when the experiments are carried out in water/AOT/*n*-heptane microemulsions, compared to the mean particle size obtained in water/AOT/hexanes microemulsions. However, it is not what we observed.

Lopez-Quintela et al.²⁴ mentioned that the relationship between the particle size and K_{ex} is more complicated than

described previously, and that the encounter-pair reactant exchange mechanism could take place. From experimental data and Monte Carlo simulations, it was shown that for K_{ex} values lower than $10^7 \text{ M}^{-1}\text{s}^{-1}$, this process takes place by a fused dimer mechanism, while for K_{ex} values larger than $10^8 \text{ M}^{-1}\text{s}^{-1}$, the exchange process takes place by an encounter-pair mechanism. In both cases, the size of the particle increases with the K_{ex} value; however, for intermediate K_{ex} values (10^7 – 10^8), a process defined as a transition between reactant exchange mechanisms takes place; and both mechanisms occur. In this region, the particle size can decrease with the increment of K_{ex} or number of carbons in the solvent.²⁴ This might explain the results obtained in our work, where the mean nanoparticle size decreases, in going from hexanes to *n*-heptane. Further experiments, making use of solvents with longer and shorter carbon chains, are necessary in order to verify if this is the case.

4. CONCLUSIONS

We have shown that by a dropwise addition of the reducing agent (NaCNBH_3) containing microemulsion to the gold ion microemulsion, it is possible to make monodispersive 4 nm size Au nanoparticles without time-consuming size-selective precipitation, colloidal digestive ripening or previous functionalization of AOT. Varying the time that a substrate is immersed in the protected nanoparticles' solution, we were able to tune the size of the deposition, forming 3D crystals of different sizes and shapes. These 3D arrays are very well defined and present a 6-fold projected symmetry structure as shown in the transmission electron (TED) patterns. Although the size distribution of the gold nanoparticles obtained with the 2.7 : 1 reducing-agent : Au-ion molar ratio was relatively large (18%), it appears that the carbon chains of the 1-decanethiol bonded to the gold nanoparticles can fold themselves and arrange among the others to organize the particles to form a long range lattice.

In the case when a less concentrated reducing agent was used, (NaCNBH_3 : gold ion molar ratio 1 : 1) a large amount of precipitate was observed. In the supernatant solution, Au nanoparticles of very uniform size were obtained that could arrange themselves, forming 2D arrays when the solution was evaporated on carbon-coated copper grids. The formation of these highly monodispersive Au nanoparticles might be explained by a "spontaneous" one step size-selective precipitation and the reason for this observations is still unclear. Changing the carbon chain length of the solvent, but working under the same conditions, 2D arrays of monodispersed nanoparticles of different sizes can be obtained. A possible mechanism is given even though further experiments and measurements are necessary in order to clarify the influence of the inter-droplet material exchange on the particle size. This variation of the two-microemulsion approach described here for synthesizing monodispersive gold nanoparticles could be

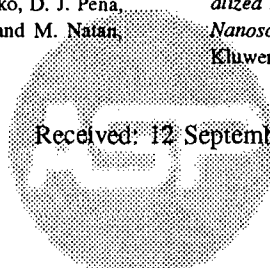
used to synthesize other noble metal nanoparticle arrays that may lead to new materials for electronic and photonic applications.

Acknowledgments: This work was supported by a grant from DOD-AFOSR (F49620-03-1-0361) and by the Idaho DOE-EPSCoR program (DE-FG02-04ER46142). We want to thank Mr. Franklin Bailey for obtaining the TEM, SEM, and TED images and Dr. Mario Arturo Lopez-Quintela and Dr. DeLyle Eastwood for useful discussions.

References and Notes

1. M. A. Hayat, *Colloidal gold: principles, methods, and applications*, Academic Press, San Diego (1989).
2. W. P. Wuelfing and R. W. Murray, *J. Phys. Chem. B* 106, 3139 (2002).
3. N. Krasteva, I. Besnard, B. Guse, R. E. Bauer, K. Mullen, A. Yasuda, and T. Vossmeyer, *Nano Lett.* 2, 551 (2002).
4. Y. J. Kim, R. C. Johnson, and J. T. Hupp, *Nano Lett.* 1, 165 (2001).
5. C. A. Mirkin, *Inorg. Chem.* 39, 2258 (2000).
6. D. L. Klein, P. L. McEuen, J. E. B. Katari, R. Roth, and A. P. Alivisatos, *Appl. Phys. Lett.* 68, 2574 (1996).
7. T. Sato, H. Ahmed, D. Brown, and B. F. G. Johnson, *J. Appl. Phys.* 82, 696 (1997).
8. M. D. Musick, C. D. Keating, L. A. Lyon, S. L. Botsko, D. J. Pena, W. D. Hollaway, T. M. McEvoy, J. N. Richardson, and M. Natan, *J. Chem. Mater.* 12, 2869 (2000).
9. W. P. Wuelfing, F. P. Zamborini, A. C. Templeton, X. G. Wen, H. Yoon, and R. W. Murray, *Chem. Mater.* 13, 87 (2001).
10. G. R. Bawendi, S. Tsubota, T. Nakamura, and M. Haruta, *Catal. Lett.* 44, 83 (1997).
11. J. J. Pietron, R. M. Stroud, and D. R. Rolison, *Nano Lett.* 2, 545 (2002).
12. S. Wang, S. Sato, and K. Kimura, *Chem. Mat.* 15, 2445 (2003).
13. B. L. V. Prasad, S. I. Stoeva, C. M. Sorensen, and K. J. Klabunde, *Langmuir*, 18, 7515 (2002).
14. B. L. V. Prasad, S. I. Stoeva, C. M. Sorensen, S. Uma, P. T. Stoimenov, V. Zaikovski, and K. J. Klabunde, *J. Phys. Chem. B* 107, 7441 (2003).
15. J. Zhang, L. D. Sun, C. Qian, C. S. Liao, and C. H. Yan, *Chinese Sci. Bull.* 46, 1873 (2001).
16. C. E. D. Chidsey, and D. N. Loiacono, *Langmuir* 6, 682 (1990).
17. P. D. I. Fletcher, A. M. Howe, and B. H. Robinson, *J. Chem. Soc. Faraday Trans.* 1, 985 (1987).
18. C. Tojo, M. C. Blanco, and M. A. Lopez-Quintela, *Langmuir* 14, 6835 (1998).
19. M. A. Lopez-Quintela, *Curr. Opinion Coll. Interf. Sci.*, 8, 137 (2003).
20. A. Taleb, C. Petit, and M. P. Pilani, *Chem. Mat.* 9, 950 (1997).
21. A. Mannia, T. Imae, T. Yogo, K. Aoi, and M. Okazaki, *J. Coll. Int. Sci.* 256, 297 (2002).
22. R. P. Bagwe, and K. C. Khilar, *Langmuir* 16, 905 (2002).
23. C. D. Bain, J. Evall, and G. M. Whitesides, *J. Am. Chem. Soc.* 111, 7155 (1989).
24. M. A. López-Quintela, J. Rivas, M. C. Blanco, C. Tojo, *Functionalized Metal Nanoparticles: Synthesis, properties and applications, Nanoscale Materials*, edited by L. M. Liz-Marzan and P. Kamat, Kluwer Academic Publishers, (2003), Chapter 6, p. 135.

Received: 12 September 2005. Revised/Accepted: 26 November 2005.



AMERICAN
SCIENTIFIC
PUBLISHERS

Nanoparticle size

DOI: 10.1002/smll.200600222

Continuous Tuning of Silver Nanoparticle Size in a Water-in-Supercritical Carbon Dioxide Microemulsion**

Carlos A. Fernandez and Chien M. Wai*

Supercritical carbon dioxide (scCO₂) provides an attractive substitute for petroleum-based organic solvents for chemical synthesis since it is nontoxic, environmentally benign, non-flammable, inexpensive, and readily available in large quantities. One unique property of scCO₂ is its tunable solvent strength through manipulation of its density (ρ), which can be controlled by varying the temperature and pressure of the fluid. This property is attractive for studying the formation of nanoparticles using water-in-scCO₂ microemulsions as nanoreactors. Shah et al.^[1] reported the influence of pressure, stabilizer, and precursor concentration in the formation and dispersion of silver nanoparticles obtained by arrested precipitation, where a thiol stabilizer was added together with hydrogen gas (H₂) to a CO₂-soluble metal precursor, silver acetylacetone. In this study, no microemulsion was used for silver nanoparticle synthesis and the reaction time was 3 h. At a thiol/precursor ratio of around 2.5 and a temperature of 80°C, the silver nanoparticles thus synthesized were found to decrease in size with increase in pressure from 4.0 ± 2.1 nm at 207 bar ($\rho = 0.61$ g mL⁻¹) to 1.7 ± 1.1 nm at 259 bar ($\rho = 0.698$ g mL⁻¹). Above that pressure, the average size of the silver nanoparticles remained virtually constant with smaller standard deviations. Synthesis of copper nanoparticles in reverse micelles was performed by Kitchens and Roberts^[2] using compressed liquid and supercritical-fluid alkanes as the bulk solvent. The size of the nanocrystals was found to increase with pressure. In supercritical propane, the median nanoparticle size (the median instead of the mean diameter was used due to the presence of large particle aggregate outliers) increased from 5.4 to 9.0 nm with increasing pressure from 241 to 345 atm at 21°C and a water-to-surfactant molar ratio (W value) of 1.5. The size variation did not show a continuous change and in the pressure range 276 to 317 atm the nanoparticle size remained unaltered. The reaction times in these studies were long (2–3 h) and the size dispersions were large and in

some cases almost as large as the median diameter of the nanoparticles.

Despite the different approaches reported in the literature for studying the pressure dependence of particle size in supercritical fluids, the relationship between the scCO₂ density and the size of the nanoparticles synthesized in water-in-CO₂ microemulsions remains unclear, and the feasibility of continuous tuning of particle size in a wide range of values by variation in the fluid density has not been achieved. Herein, we present our recent results demonstrating, for the first time, that the size of silver nanoparticles synthesized in a scCO₂ microemulsion varies linearly and over a particularly wide range of values with the density of the fluid phase. The observation suggests a simple technique for continuous tuning of the size of nanoparticles synthesized in reverse micelles with scCO₂ as a solvent. This unique technique may have a range of applications for making 2D and 3D arrays of nanoparticles of variable size for new optical materials and for analytical applications, such as ultratrace detection of numerous analytes by size-dependent optical enhancement in surface-enhanced Raman scattering (SERS).^[3–5]

The transmission electron microscopy (TEM) images of the stabilized nanoparticles, obtained by evaporation of an acetone solution containing the nanoparticles on a carbon-coated copper grid, showed relatively monodispersive nanoparticles and a distinct separation of particles by the stabilizing ligand (Figure 1).

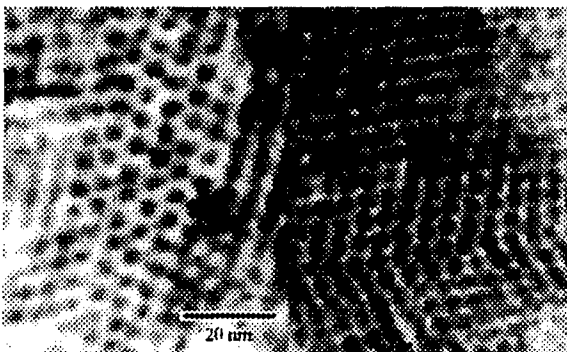


Figure 1. TEM images of perfluorodecanethiol (F-thiol)-protected silver nanoparticles with an average diameter of 3 nm. Left: 2D array showing a distinct separation between nanocrystals. Right: Two superimposed monolayers of nanoparticles. (Scale applies to both micrographs).

[*] C. A. Fernandez, Prof. C. M. Wai
Department of Chemistry
University of Idaho
Moscow, ID 83844 (USA)
Fax: (+1)208-885-6173
E-mail: cwai@uidaho.edu

[**] The authors would like to thank Dr. DeLyle Eastwood for useful discussions and Byunghoon Yoon for synthesizing the fluorinated AOT. This work was supported by a grant from DOD-AFOSR (F49620-03-1-0361) and by the Idaho DOE-EPSCoR program (DE-FG02-04ER46142).

Figure 2 shows the variation of the average size of Ag nanoparticles with fluid pressure when they were synthesized and stabilized according to the procedures described in the Experimental Section at 40°C. The concentration of the surfactant, sodium bis(2,2,3,3,4,4,5,5-octafluoro-1-pentyl)-2-sulfosuccinate (F-AOT, 20 mM), concentration of precursors and stabilizer, the W value ($W = 6$), and the temperature (40°C) in this series of experiments were kept constant and only the pressure of the scCO₂ was varied from 280 to 460 atm. The average size of the Ag nanoparticles

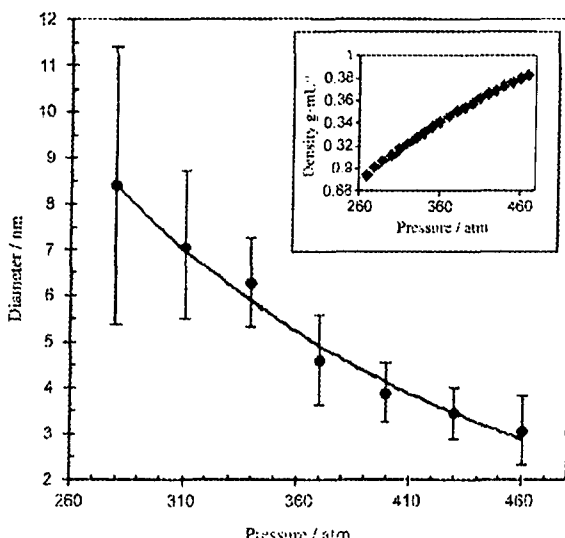


Figure 2. Influence of CO_2 pressure on the average size and size distribution of silver nanoparticles at 40°C , $W=6$, $[\text{F-AOT}]=20\text{ mM}$. Inset: density versus pressure at a fixed temperature of 40°C .

synthesized by the CO_2 microemulsion method decreases continuously from about 8.4 nm at 280 atm to about 3 nm at 460 atm (Figure 2). The slope of the trend line decreases as the pressure increases. The size distribution of the Ag nanoparticles is larger for the particles formed at low pressures. The inset in Figure 2 shows the variation of the density of the CO_2 with the pressure at a constant temperature of 40°C . There is an increment in the density of the solvent as the pressure increases, and the slope of this plot decreases as the pressure reaches higher values.

Figure 3 shows the effect of temperature on the size and the size distribution of the Ag nanoparticles synthesized by the CO_2 microemulsion method. The pressure of this series of experiments was fixed at 280 atm and the temperature was varied from 32 to 65°C . Other parameters including the concentration of the surfactant (in this case 10 mM), precursor and stabilizer concentrations, and the W value ($W=6$) were all kept constant as in the case of the pressure dependence study. The average size of the Ag nanoparticles increases continuously with temperature (see Figure 3). Again, the size distribution is larger for the larger particles formed at higher temperatures. The density of scCO_2 is known to decrease with increasing temperature at a fixed pressure. This is shown in the inserted plot of solvent density versus temperature (at a fixed pressure of 280 atm) in Figure 3.

The pressure (P) and the temperature (T) dependence studies all suggest that the particle size of the Ag nanoparticles is related to the density of the fluid phase within the temperature and pressure ranges used. The cohesive energy density^[6] of the solvent (scCO_2) is higher at increased solvent density (higher P or lower T), which results in better ligand–solvent interactions.^[7] Therefore, at higher pressures or lower temperatures, the surfactant molecules in the micelles may be more solvated and the micelle–micelle inter-

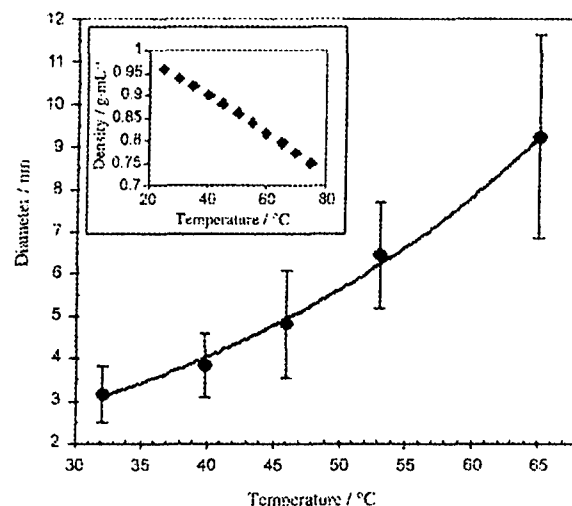


Figure 3. Influence of temperature on the average size and size distribution of silver nanoparticles at a fixed CO_2 pressure of 280 atm, $W=6$, $[\text{F-AOT}]=10\text{ mM}$. Inset: density versus temperature at a fixed pressure of 280 atm.

actions become weaker. Under these conditions, the net effect might be a decrease in the amount of material exchanged during collision, and smaller particles and narrower size distributions are obtained. Another factor to consider is the dependence of the size of the micellar water core on pressure and temperature. Small-angle neutron scattering (SANS) experiments carried out by Xu et al.^[8] showed that an increment in pressure or temperature had an impact on the size of the water droplets. They found that by increasing the pressure from 170 to 380 atm, the size of the water core decreased by 14% at 27°C ($W=5$ and surfactant concentration 27 mM). On the other hand, an increment in the temperature from 26 to 50°C produced a decrease in the water-core radius by 3 to 4% in the range of the surfactant concentration used in their experiments and at $W=5$. The surfactant used in their study was bis[2-(F-hexyl)ethyl] phosphate sodium and ammonium salts. In our study, the stability of the microemulsion with respect to fluid density and the effects of pressure and temperature on the water-core size might both play a role in controlling the final silver nanoparticle size.

Several experiments were carried out with different pressure–temperature combinations, some of them presenting identical fluid densities. For these experiments, where the density was identical but the pressure–temperature conditions were different, the average sizes of the nanocrystals obtained were statistically equivalent. This finding demonstrates that a variation in the temperature or pressure of these water-in- CO_2 microemulsion systems (within the ranges studied) seems to affect the final size of the nanoparticle due *mainly* to a variation in the density of the solvent.

A plot of the average Ag nanoparticle size with the scCO_2 density using different pressure–temperature combinations is shown in Figure 4A for $W=6$. A linear relationship between the average size of the Ag nanoparticle and

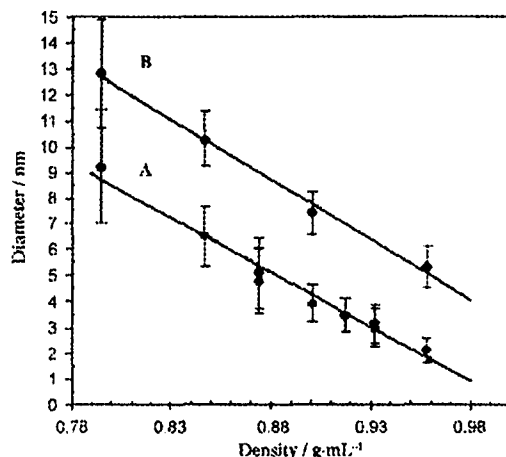


Figure 4. Influence of CO_2 density on the average size and size distribution of silver nanoparticles, $[\text{F-AOT}] = 10 \text{ mM}$. A) $W = 6$. B) $W = 10$.

the density of the fluid phase (in the range 0.79 to 0.96 g mL^{-1}) is observed. The average size of the metal particles varies from 9.3 nm at 0.80 g mL^{-1} to about 1.9 nm at 0.96 g mL^{-1} with a slope of $-0.042 \text{ nm}/(\text{mg mL}^{-1})$. The size dispersion varied from 36 to 12% in all the experiments, and was usually lower at greater densities. According to Figure 4A, continuous tuning of the size of silver nanoparticles synthesized by the CO_2 microemulsion method could be achieved by varying the density of the fluid phase in this range. Figure 4B shows the diameter of the nanocrystals as a function of density for $W = 10$. A linear relationship with a slope of $-0.046 \text{ nm}/(\text{mg mL}^{-1})$, similar to the one obtained for $W = 6$, was observed. The increment in the average size of the nanoparticles with the size of the micelles (W value) in scCO_2 microemulsions is known in the literature.^[9,10] Our results suggest that the size of the nanoparticles follows a linear relationship with the density of the fluid phase independently of the size of the microemulsion. In consequence, by manipulating both the density and W value, the diameter of the nanoparticles could be tuned over an even wider range of values.

Figure 5 shows the variation of the nanoparticle diameter with the fluid density for two different concentrations of surfactant; one of the plots has already been shown in Figure 4A. In both cases, a linear relationship is obtained but there is an increase of 67% in the slope when the concentration of F-AOT increases from 10 to 20 mM . The concentration of silver ion and NaCNBH_3 in the water core is constant in all these experiments, but the population of the CO_2 microemulsion increases in the system. The number of collisions between adjacent reverse micelles would increase as a result, and larger nanoparticles should form.^[11] The size of the nanoparticles decreases by 40 to 60% when the concentration of surfactant is decreased from 20 to 10 mM .

The reaction time is another factor that may influence the size of the Ag nanoparticles synthesized by the CO_2 microemulsion method. As is explained in the Experimental Section, the reason for the choice of 3.5 min to discontinue the reaction was to avoid further aggregation, as indicated

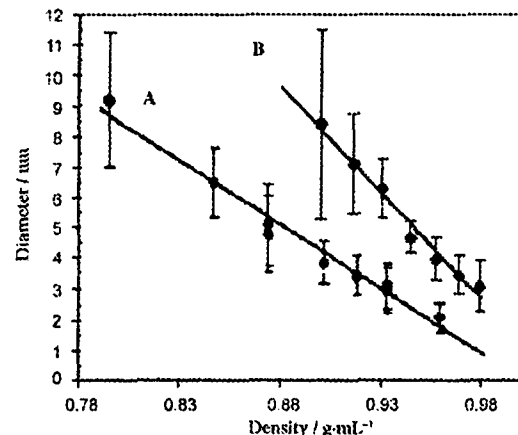


Figure 5. Influence of CO_2 density on the average size and size distribution of silver nanoparticles, $W = 6$. A) $[\text{F-AOT}] = 10 \text{ mM}$. B) $[\text{F-AOT}] = 20 \text{ mM}$.

by our spectroscopic observation (through a red shift and a decrease in the surface plasmon absorption peak) when the reaction time was extended. By increasing the reaction time to 30 min , the average size of the silver nanoparticles (obtained by analysis of the TEM data) increased from 3.9 ± 0.8 to $5.8 \pm 1.6 \text{ nm}$ when scCO_2 at 280 atm and 40°C was employed ($[\text{F-AOT}] = 10 \text{ mM}$, $W = 6$). Tuning of Ag nanoparticles by density variation appears to work well at short reaction times where the exchange-channel mechanism and the micellar-templating effect dominate. For very long reaction times, as the nanoparticles grow larger, the surfactant might act as a dispersant ligand^[2] and sterically stabilize the nanoparticles without involving the microemulsion.

In summary, we have shown that the size of silver nanoparticles synthesized by the scCO_2 microemulsion-templating method can be continuously tuned over a large range of values by density variation of the fluid phase. This approach gave consistent results for two different W values and for two different concentrations of surfactant tested. The variation of the size of the nanocrystals with the density of the solvent (which follows a linear relationship) might depend on the stage of the synthetic process at which the nanoparticles are stabilized. Other parameters such as the nature of the nanoparticles and the solvent may have an effect as well. We are currently applying this method to produce other metallic and semiconductor nanocrystals in scCO_2 .

Experimental Section

The surfactant used in this study, sodium bis(2,2,3,3,4,4,5,5-octafluoro-1-pentyl)-2-sulfosuccinate (F-AOT), was prepared in our laboratory following the procedure of Eastoe et al.^[12] with some modification. The reducing agent sodium cyanoborohydride (NaCNBH_3 ; purity $> 95\%$) was obtained from Aldrich, while the metal precursor silver nitrate (AgNO_3 , $> 99.5\%$) was obtained from ACROS. The stabilizer or protecting agent, 1H,1H,2H,2H-perfluorodecanethiol (F-thiol; $> 99\%$) was purchased from Fluka.

The liquid CO₂ was metered with an ISCO syringe pump (model 260D) and pump controller (series D) and introduced to the high-pressure reactors via stainless-steel tubing (1/16 inch outer diameter, 0.03 inch inner diameter). The high-pressure vessels were heated with a thermal block, and the temperature was kept constant at $\pm 0.1^\circ\text{C}$ and controlled with a J-type sensor and an Omega digital controller. Three homemade high-pressure vessels were utilized. One vessel (volume 18.5 mL) was equipped with a fiber-optic system (path length 3 mm) and connected to a CCD-array UV/Vis spectrometer (Spectral Instruments model Si-440, Tucson, AZ).^[13] The spectrometer was capable of recording a full spectrum from 240 to 900 nm in 2 s. It could also measure the change in absorbance with time at a fixed specific wavelength. The second vessel was a 17-mL high-pressure view cell with sapphire windows. The last one was a 17.5-mL vessel with a movable piston. The high-pressure vessels were connected to each other via 1/16 in. stainless-steel tubing. Each system was isolated from the others by HIP high-pressure valves.

The cloud points for the microemulsion containing Ag⁺ ions and Ag nanoparticles were studied using a view cell connected to a piston (both immersed in a thermal bath) and by visual observation of the phase behavior. At 40 °C, a *W* value of 6, and a surfactant concentration of 20 mM, the cloud point was 125 \pm 2 atm. Above these pressures at 40 °C, the microemulsion was stable and optically transparent. The cloud-point boundary was approximately linear in a pressure versus temperature plot with a slope of 1.25 atm °C⁻¹. Our experiments were performed above the cloud-point pressure to the limit of our high-pressure system (about 450 atm). The variation in density of scCO₂ at different temperatures and pressures is known.^[14]

The silver nanoparticles were synthesized by mixing two water-in-scCO₂ microemulsions, one containing a silver nitrate solution (0.15 M) and the other containing an aqueous solution of NaCNBH₃ (0.35 M). The microemulsion containing the reducing agent was pushed into the silver nitrate microemulsion. Formation of the Ag nanoparticles after mixing was monitored spectroscopically, using the optical fiber cell, by recording the absorption spectra *in situ* every 2 s. A blank measurement was taken before the reaction to provide a spectroscopic baseline, using a water-in-scCO₂ microemulsion containing deionized water. The characteristic absorption peak due to surface plasmon resonance of Ag nanoparticles ($\lambda = 420$ nm) increased to a maximum at about 250 s after mixing, started to decrease gradually in intensity, and reached a plateau in about 62 min. A decrease in its full width at half-maximum ($\Delta(\text{FWHM}) \approx 43$ nm) when going from 3 to 62 min of reaction time was noticed, together with a red shift of 15 nm of the absorption peak wavelength. This, together with the decrease in the peak intensity, should indicate that the concentration of the nanoparticles reached a maximum in the first 4 min and was followed by a decrease in concentration, probably attributable to aggregation.^[15]

Therefore, the F-thiol stabilizer was introduced to the system at exactly 250 s after mixing. The thiol-stabilized Ag nanoparticles were collected in an acetone solution after depressurizing

the system for TEM measurements. The protected Ag nanoparticles were stable in acetone for several days, whereas the unprotected Ag nanoparticles in acetone precipitated after approximately 10 min. TEM images were obtained with a JEOL 1200 EX II transmission electron microscope at an accelerating voltage of 120 kV. Energy-dispersive spectroscopy (EDS) analysis was carried out with a LEO Supra 35 VP field-emission scanning electron microscope. EDS analysis of the stabilized nanoparticles showed only silver, carbon, fluorine, and sulfur in the samples. The average size of the Ag nanoparticles was obtained from the TEM images by counting at least 300 particles using interactive imaging software (Matrox Inspector) from Matrox Electronic Systems (Dorval, Quebec, Canada). An important feature of this software is that it can measure a large number of particles without bias or human error.

Keywords:

emulsions • nanoparticles • silver • supercritical fluids

- [1] P. S. Shah, H. Shabbir, K. P. Johnston, B. A. Korgel, *J. Phys. Chem. B* **2002**, *106*, 12178.
- [2] C. L. Kitchens, C. B. Roberts, *Ind. Eng. Chem. Res.* **2004**, *43*, 6070.
- [3] S. R. Emory, W. E. Haskins, S. Nie, *J. Am. Chem. Soc.* **1998**, *120*, 8009.
- [4] V. N. Pustovit, K. M. Walker, T. V. Shahbazyan in *Proceedings of the NSTI Nanotechnology Conference and Trade Show, Vol. 3* (Eds: M. Laudon, B. Romanowicz), NSTI, Boston, **2004**, p. 395.
- [5] Y. Badra, M. A. Mahmoud, *J. Mol. Struct.* **2005**, *749*, 187.
- [6] J. Burke, *AIC Book and Paper Group Annual, Vol. 3* (Ed: C. Jensen), AIC, Washington, **1984**, p. 13.
- [7] M. L. O'Neill, Q. Cao, M. Fang, K. P. Johnston, S. P. Wilkinson, C. D. Smith, J. L. Kerschner, S. H. Jureller, *Ind. Eng. Chem. Res.* **1998**, *37*, 3067.
- [8] B. Xu, G. W. Lynn, J. Guo, Y. B. Melnichenko, G. D. Wignall, J. B. McClain, J. M. DeSimone, C. S. Johnson, Jr., *J. Phys. Chem. B* **2005**, *109*, 10261.
- [9] H. Ohde, M. Ohde, K. H. Bailey, C. M. Wai, *Nano Lett.* **2002**, *2*, 721.
- [10] S. S. Hong, M. S. Lee, H. S. Hwang, K. T. Lim, S. S. Park, C. S. Ju, G. D. Lee, *Sol. Energy Mater. Sol. Cells* **2003**, *80*, 273.
- [11] L. Magagnin, V. Bertani, P. L. Cavallotti, R. Maboudian, C. Carra-ro, *Microelectron. Eng.* **2002**, *64*, 479.
- [12] I. Eastoe, S. Nave, A. Downer, A. Paul, A. Rankin, K. Tribe, *Langmuir* **2000**, *16*, 4511.
- [13] H. Ohde, F. Hunt, C. M. Wai, *Chem. Mater.* **2001**, *13*, 4130.
- [14] National Institute of Standards and Technology, "Thermophysical Properties of Fluid Systems", can be found under <http://webbook.nist.gov/chemistry/fluid>
- [15] J. Liu, P. Raveendran, Z. Shervani, Y. Ikushima, Y. Hakuta, *Chem. Eur. J.* **2005**, *11*, 1854.

Received: May 5, 2006

Published online on September 14, 2006

Continuous Tuning of Cadmium Sulfide and Zinc Sulfide Nanoparticle Size in a Water-in-Supercritical Carbon Dioxide Microemulsion

Carlos A. Fernandez and Chien M. Wai*^[a]

Abstract: The size and size dispersion of cadmium sulfide and zinc sulfide semiconductor nanoparticles can be continuously tuned over a wide range of values by adjusting the density of the fluid phase in water-in-supercritical CO_2 microemulsions. The average size of the ZnS nanoparticles decreases linearly from approximately 9.1 to 1.9 nm with increasing fluid density from 0.86 to 0.99 g cm^{-3} at a water-to-surfactant ratio (W value) of 10. At a W value of 6, the particle size can be tuned from 7.0 to 1.5 nm in the same density range. In the case of CdS nanocrystals, the

size varied from 7.1 to 2.0 nm when the W value was 10 and from 4.0 to 1.3 nm when the W value employed was 6, in the same density range. Monodisperse CdS and ZnS nanoparticles were synthesized by chemical reaction of cadmium or zinc nitrate with sodium sulfide, using two water-in-supercritical CO_2 microemulsions as nanoreactors followed by protection with a fluorinat-

Keywords: microemulsions • nanoparticles • semiconductors • supercritical carbon dioxide

ed-thiol stabilizer. The stabilizer is introduced at 6 and 16 minutes after the mixing of the two microemulsions where the intensity of the characteristic absorption peak due to the quantum confinement properties of the CdS and ZnS nanoparticles (280 and 360 nm) reaches a maximum, respectively. The supercritical CO_2 microemulsion method represents a simple approach to use a density-tunable solvent for synthesizing size-controlled semiconductor nanoparticles over a broad range of values.

Introduction

Synthesis of semiconductor quantum dots, such as cadmium sulfide and zinc sulfide nanoparticles, have been largely explored during the last decade due to their size-dependent optical, magnetic and electric properties.^[1-3] Luminescence tagging and imaging, medical diagnostics, drug delivery, and nanoelectronics are some of the applications that are being developed with these nanomaterials.^[4-8] One of the approaches utilized to synthesize these nanomaterials is the microemulsion-templated method using compressed gases as solvents. Particularly, supercritical carbon dioxide (sc CO_2) has been used as the bulk solvent in microemulsion systems to prepare semiconductor nanoparticles.^[9] Odhe et al.^[10] prepared CdS and ZnS nanoparticles in sc CO_2 using a microemulsion approach. They showed that the size of the quantum dots can be adjusted with the water-to-surfactant molar ratio or W value.

Supercritical fluids (SCFs) have attracted considerable interest as a reaction medium to synthesize nanoparticles,^[11-14] because the variations in SCF solvent properties, such as density, diffusivity, viscosity, and dielectric constant, can be easily manipulated by changing the system temperature and pressure.^[15,16] In addition to these advantages, sc CO_2 provides an attractive substitute for petroleum-based organic solvents for chemical synthesis since it is nontoxic, environmentally-benign, nonflammable, inexpensive, and readily available in large quantities. The unique property of supercritical fluids, including sc CO_2 , is its tunable solvent strength through manipulation of its density (ρ), which can be easily controlled, as mentioned above, by varying temperature and pressure of the fluid phase. This property is attractive for studying nanoparticles' formation using water-in-sc CO_2 microemulsions as nanoreactors. There are a few reports studying the variation in the size of metallic nanoparticles with the density of the fluid phase. Shah et al.^[17] reported the influence of pressure, stabilizer, and precursor concentration in the formation and dispersion of silver nanoparticles obtained by arrested precipitation, where a thiol stabilizer was added together with hydrogen gas (H_2) to a CO_2 -soluble metal precursor, silver acetylacetone. In this study, no microemulsion was used for silver nanoparticle synthesis and

[a] C. A. Fernandez, Prof. C. M. Wai
Department of Chemistry, University of Idaho
P.O. Box 442343, Moscow, ID 83844-2343 (USA)
Fax: (+1) 208-885-6173
E-mail: cwai@uidaho.edu

the reaction time was 3 h. At a thiol/precursor ratio of around 2.5 and a temperature of 80 °C, the silver nanoparticles thus synthesized were found to decrease in size with increase in pressure from 4.0 ± 2.1 nm at 207 bar ($\rho = 0.61 \text{ g mL}^{-1}$) to 1.7 ± 1.1 nm at 259 bar ($\rho = 0.698 \text{ g mL}^{-1}$). Above that pressure, the average size of the silver nanoparticles remained virtually constant with smaller standard deviations. Synthesis of copper nanoparticles in reverse micelles was performed by Kitchens and Roberts^[18] using compressed liquid and supercritical fluid alkanes as the bulk solvent. The size of the nanocrystals was found to increase with pressure. In supercritical propane, the median nanoparticle size (the median instead of the mean diameter was used due to the presence of large particle aggregate outliers) increased from 5.4 to 9.0 nm with increasing pressure from 241 to 345 atm at 21 °C and a W value of 1.5. The size variation did not show a continuous change and in the pressure range 276 to 317 atm the nanoparticle size remained unaltered. The reaction times in these studies were long (2–3 h) and the size dispersions were large and in some cases almost as large as the nanoparticles' median diameter.

We have recently shown, for the first time, that the size of silver nanoparticles can be tuned over a wide range of values by adjusting the density of scCO₂.^[19] We were able to synthesize silver nanoparticles with sizes ranging from 1.9 to 9.3 nm when W=6 was used and from 5.5 to 13 nm when a higher water-to-surfactant molar ratio (W=10) was employed.

To our knowledge, the variation in size of semiconductor quantum dots with respect to supercritical CO₂ density, have not been explored. In this article, we present a study performed in scCO₂ for synthesizing two well-known semiconductor nanocrystals, CdS and ZnS. We demonstrate that the size of CdS and ZnS nanoparticles synthesized in a scCO₂ microemulsion, varies linearly with the density of the fluid, in a similar fashion silver nanoparticles have proven. The observation suggests a simple technique for continuous tuning the size of semiconductor nanoparticles synthesized in reverse micelles, using scCO₂ as a solvent. This unique technique may have a range of applications for making 2D and 3D arrays of nanoparticles of variable size for new optical materials,^[20,21] biosensor-related applications,^[22–24] and, when passivated with a wider bandgap material, targeting luminescent probes in biological labeling and diagnostics.^[25,26]

Results and Discussion

Figure 1 shows a representative TEM micrograph for the 1*H*,1*H*,2*H*,2*H*-perfluorodecanethiol (F-thiol) stabilized CdS (Figure 1a) and ZnS (Figure 1b) nanoparticles, obtained by evaporation of an acetone solution containing the nanoparticles on a carbon-coated copper grid. The experimental conditions for the nanoparticles shown in Figure 1 were 300 atm, 40 °C for the synthesis of CdS nanoparticles and 350 atm, 40 °C for the synthesis of ZnS nanoparticles. The

surfactant concentration (10 mM), W value (W=10), and precursors concentrations (CdNO₃ or ZnNO₃=0.3 M, Na₂S=0.6 M) were equivalent in both situations. Relatively monodispersive nanoparticles were observed with a distinct separation of particles by the stabilizing ligand.

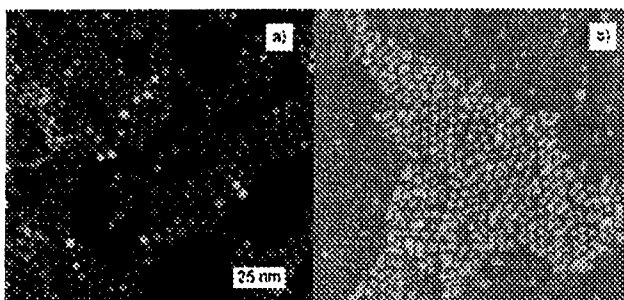


Figure 1. TEM micrographs of the F-thiol-protected a) CdS and b) ZnS nanoparticles with an average diameter of 4.8 and 4.0 nm, respectively. Scale applies to both Figures.

Figure 2 shows the variation of the average size of CdS nanoparticles with the fluid pressure when they were synthesized and stabilized according to the procedures described in the Experimental Section at 40 °C. The concentration of the surfactant, sodium bis(2,2,3,3,4,4,5,5-octafluoro-1-penty)-2-sulfosuccinate (F-AOT, 10 mM), concentration of precursors and stabilizer, the W value (molar ratio of water/surfactant, W=10) and the temperature (40 °C) of these series of experiments were kept constant and only the pressure of the scCO₂ was varied from 220 to 400 atm. The average size of the CdS nanoparticles synthesized by the CO₂ microemulsion method decreases continuously from about 7 ± 1 nm at 220 atm to about 2.9 ± 0.4 nm at 400 atm as shown in Figure 2. The slope of the trend line decreases as the pressure increases. The size distribution of the CdS nanoparticles is larger for the particles formed at low pres-

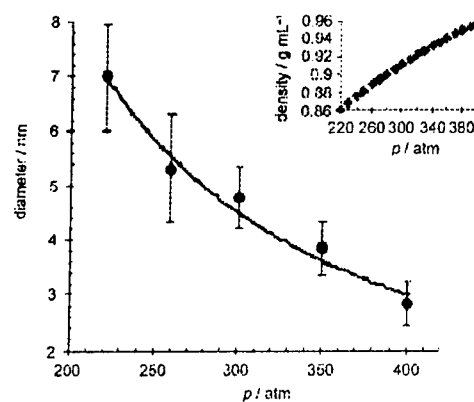


Figure 2. Influence of CO₂ pressure on the average size and size distribution of CdS nanoparticles at 40 °C, W=10, [F-AOT]=10 mM. Insert: Density versus pressure at a fixed temperature of 40 °C.

ures. The insert on Figure 2 shows the variation of the density of the CO_2 with the pressure at a constant temperature of 40°C . There is an increment in the density of the solvent as the pressure increases and the slope of this plot decreases as the pressure reaches higher values. The effect of temperature on the size and size distribution of the CdS nanoparticles synthesized by the CO_2 microemulsion method is shown in Figure 3.

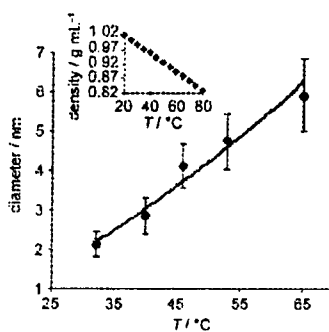


Figure 3. Influence of temperature on the average size and size distribution of CdS nanoparticles at a fixed CO_2 pressure of 400 atm, $W=10$, $[\text{F-AOT}]=10\text{ mM}$. Insert: Density versus temperature at 400 atm.

The pressure of this series of experiments was fixed at 400 atm and the temperature varied from 32 to 65°C . Other parameters including the concentration of the surfactant (in this case, 10 mM), precursors and stabilizer concentrations, and the W value ($W=10$) were all kept constant. The average size of the CdS nanoparticles increases continuously with temperature as shown in Figure 3. Again, the size distribution is larger for the larger particles formed at higher temperatures. The density of scCO_2 is known to decrease with increasing temperature at a fixed pressure and it is shown in the inserted plot of solvent density versus temperature (at a fixed pressure of 400 atm) in Figure 3. These observations may be an indication that the particle size of the CdS nanoparticles is related to the density of the fluid phase within the temperature and pressure ranges of this study. At this point, it is important to introduce the term Cohesive Energy Density (CED),^[27] which is a direct reflection of the degree of van der Waals forces holding molecules together. The CED of the solvent (scCO_2) is a function of the fluid density and is higher at increased solvent density (higher p or lower T).^[28] When the CED of solute and solvent is similar (scCO_2 and the fluorinated surfactant tails in the micelles), their intermolecular attractive forces are comparable. Since the solubility of two materials depends on their intermolecular attractive forces, one might expect that materials with similar CED values would be miscible. Under these conditions, the interactions between solvent–surfactant tails are maximized.^[28] Therefore, at higher pressures or lower temperatures, the fluorinated surfactant molecules in the micelles may be more solvated and the micelle–micelle interactions become weaker. The result might be a decrease

in the amount of materials exchange during collision and smaller particles are obtained.

Another factor to take into account is the influence of the pressure and temperature of the system on the size of the micellar water core. Xu et al.^[29] showed that an increment in pressure has an impact in the size of the water droplets. By means of SANS experiments, they found that the size of the water-core decreased by 14% when the pressure was increased from 170 to 380 atm at 27°C ($W=5$ and surfactant concentration 27 mM). The surfactant used in this study was bis[2-(F-hexyl)ethyl] phosphate salts of sodium, and ammonium. In our study, both parameters, micelles' stability through density and water-core size through pressure, might be playing a role in controlling the final nanoparticle size. In order to identify which parameter would lead this size-controlling role, several experiments were carried out with different pressure–temperature combinations, some of them presenting identical fluid densities. For these experiments, where the density was identical but the pressure–temperature conditions were different, the average sizes of the CdS nanocrystals obtained were statistically equivalent. This demonstrates that a variation in the temperature or in the pressure of these water-in- CO_2 microemulsion systems (within the ranges studied here) seems to affect the final nanoparticle's size due *mainly* to a variation in the density of the solvent.

Figure 4a shows a plot of the average CdS nanoparticle size with the scCO_2 density using different pressure–temperature combinations, for $W=10$. A linear relationship between the average size of the CdS nanoparticles and the density of the fluid phase (in the range 0.86 to 0.99 g cm^{-3}) is observed. The average size of the semiconductor particles varies from $7\pm1\text{ nm}$ at 0.86 g cm^{-3} to about $2.1\pm0.3\text{ nm}$ at 0.99 g cm^{-3} with a slope of $-0.036\text{ nm per (mg mL}^{-1}\text{)}$. The size dispersion varied from 12 to 20% in all the experiments, being in general larger at lower densities. From Figure 4a, it seems possible that a continuous tuning of the CdS nanoparticle size synthesized by the CO_2 -microemulsion method could be achieved by varying the density of the fluid in this range. Figure 4b shows the diameter of the nanocrystals as a function of density for $W=6$, where the size varied from $4.0\pm0.5\text{ nm}$ to $1.3\pm0.2\text{ nm}$. A linear relationship with a slope of $-0.020\text{ nm per (mg mL}^{-1}\text{)}$ similar to the one obtained for $W=10$ was observed. This decrease in the size of the nanocrystals with the decrease in the size of the micellar water-core may be due to the fact that there is a change in the hydration of the ions.^[30] At very low W values, a small number of ions are free from interacting with the negative heads of the F-AOT surfactant at the surface of the micelle. In this way, the ions are less reactive due to the fact that they have to be pulled away from the micelles' anionic walls. In such cases, the precipitation reaction gives rise to a smaller number of nuclei and the average of the final nanocrystal's size is smaller. Conversely, when the water content is larger (larger W values) there are a larger number of "free" ions and an increment in the reaction yield should be observed. Consequently, the number of

nuclei increases, and the size and production of nanocrystals increases. Our results suggest that the nanoparticle's size follows a linear relationship with the density of the fluid phase and that this trend is independent of the W value or size of the microemulsion. In consequence, by manipulating both parameters, density and W value, the diameter of the nanoparticles could be tuned over even a wider range of values.

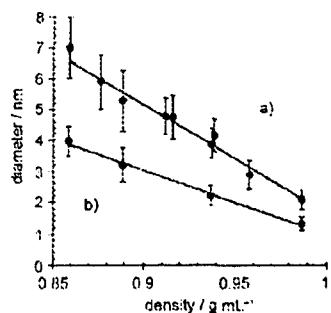


Figure 4. Influence of CO_2 density on the average size and size distribution of CdS nanoparticles, $[\text{F-AOT}] = 10 \text{ mM}$. a) $W = 10$; b) $W = 6$.

The variation of the nanoparticle's diameter with the fluid density was also studied for two different concentrations of surfactant. Figure 5 shows the results, where one of the plots (Figure 5a) was already shown in Figure 4a. In both cases a linear relationship was obtained and the slope of the trend line was $-0.030 \text{ nm per (mg mL}^{-1}\text{)}$ when the concentration of FAOT was 20 mM . An increment in the size of the CdS nanoparticles was observed when a greater surfactant concentration was employed specially at higher densities. The concentration of Cd^{2+} and S^{2-} ions in the water core is constant in all these experiments, but the population of the CO_2 microemulsion increases in the system. The number of collisions between adjacent reverse micelles would increase as a result, and larger nanoparticles should form.^[31]

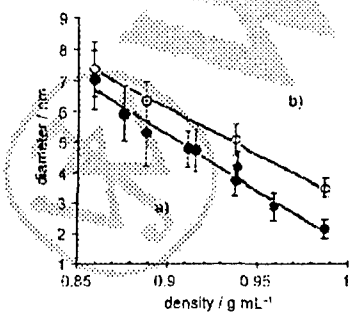


Figure 5. Influence of CO_2 density on the average size and size distribution of CdS nanoparticles, $W = 10$. a) $[\text{F-AOT}] = 10 \text{ mM}$; b) $[\text{F-AOT}] = 20 \text{ mM}$.

Figure 6 shows a representative excitation and emission spectra of the stabilized CdS nanoparticles obtained at two different densities of scCO_2 . A red shift of 14 nm (from 349

to 363 nm) together with an increment in the Full Width at Half Maximum (FWHM) from 48 to 63 nm , was observed in the excitation spectra when the density of the solvent decreased from 0.92 to 0.87 g mL^{-1} ($W = 10 \text{ F-AOT}$ concentration 10 mM). This is related to the observed increment in the average size of the CdS particles from 4.7 ± 0.7 to $6.0 \pm 0.9 \text{ nm}$, when the synthesis of the materials is carried out at lower fluid densities. The emission spectra are associated to the emission of the surface defects, such as electron-hole pair recombination of surface trap states.^[32,33] Yet again, a red shift in the fluorescence wavelength from 440 to 498 nm was observed when the size of the CdS nanoparticles increased in the range described above.

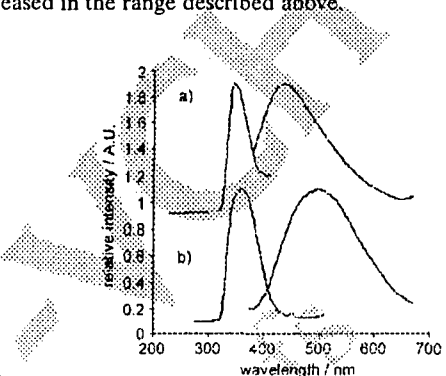


Figure 6. Excitation and emission spectra of CdS nanoparticles obtained at two different fluid densities. a) Spectra of 4.7 nm CdS nanoparticles obtained at a supercritical CO_2 density of 0.92 g mL^{-1} ; b) spectra of 6.0 nm CdS nanoparticles obtained at a supercritical CO_2 density of 0.87 g mL^{-1} .

The variation of the size of ZnS nanoparticles with the fluid density was studied by performing experiments in a similar way to that of the CdS nanoparticles. Figure 7 shows a plot of the variation of ZnS nanoparticles with the density of scCO_2 for two different W values. For W value of 10 (Figure 7a), the size of the nanoparticles decreased from 9 ± 1 to $1.9 \pm 0.3 \text{ nm}$ when the density of the solvent increased from 0.86 to 0.99 g mL^{-1} . The slope of the trend line was $-0.053 \text{ nm per (mg mL}^{-1}\text{)}$. When $W = 6$ was used in the preparation of the microemulsions, the size of the ZnS particles synthesized decreased from 7 ± 1 to $1.5 \pm 0.2 \text{ nm}$ with a slope of $-0.042 \text{ nm per (mg mL}^{-1}\text{)}$, as shown in Figure 7b. The increment in the average size of the nanoparticles with the size of the micelles (W value) in scCO_2 microemulsions is known in the literature,^[34,35] and it was described previously for CdS nanoparticles.

When the surfactant concentration was doubled from 10 to 20 mM , the size of the ZnS particles showed a partially different behavior to the one observed for the CdS nanoparticles. In both conditions, the size of the nanoparticles decreased with an increment in the fluid density with a slope of $-0.044 \text{ nm per (mg mL}^{-1}\text{)}$ for the case of F-AOT concentration of 20 mM and similar to the one observed for a surfactant concentration of 10 mM ($-0.053 \text{ nm per (mg mL}^{-1}\text{)}$). Figure 8 shows this behavior, where one of the plots (Fig-

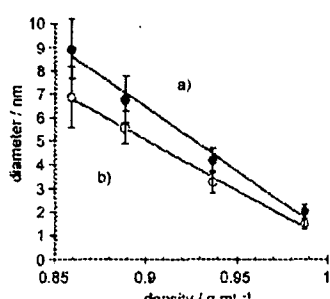


Figure 7. Influence of CO_2 density on the average size and size distribution of ZnS nanoparticles, $[\text{F-AOT}] = 10 \text{ mM}$. a) $W = 10$; b) $W = 6$.

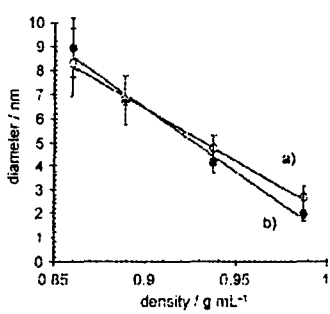


Figure 8. Influence of CO_2 density on the average size and size distribution of ZnS nanoparticles, $W = 10$. a) $[\text{F-AOT}] = 20 \text{ mM}$; b) $[\text{F-AOT}] = 10 \text{ mM}$.

Figure 8b) was already shown on Figure 7. It seems that, in contrast to what we observed for CdS nanoparticles, the size of the nanoparticles might be independent of the surfactant concentration, mainly at lower solvent densities. It is important to mention that Natarajan et al.^[36] by means of a modeling approach, found that the size of the nanoparticles was unaffected by changing the surfactant concentration, keeping constant the W value. He predicted that by keeping the W value constant, while increasing or decreasing proportionally the water and surfactant concentration, the aqueous core volume would remain constant. Therefore, according to his study, the size and size distribution of the nanoparticles should be unaffected. This group cited the experimental case of silver nanoparticles synthesized in water-in-oil microemulsions, where an increment in the surfactant concentration (keeping constant the rest of the parameters, including the W value) produced an increase in the number of particles formed without any changes in the average size. Consequently, the influence of the surfactant concentration on the final nanoparticle size seems to depend on the nanoparticle nature, and solvent and may raise a question whether the collision frequency plays a role in the final particle size at all.

We performed some experiments using different pressure-temperature combinations with similar density values. For these experiments, the average sizes of the ZnS nanocrystals obtained were statistically equivalent, demonstrating

as in the case of CdS nanoparticles, that a variation in the temperature or in the pressure of these water-in- CO_2 microemulsion systems (within the ranges studied here) may affect the final nanoparticle's size due mainly to a variation in the density of the solvent. On Figure 9, the excitation and

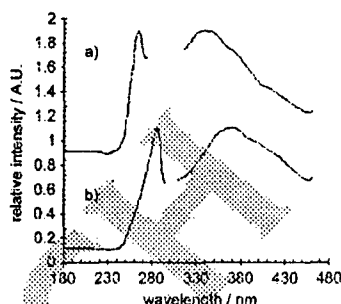


Figure 9. Excitation and emission spectra of ZnS nanoparticles obtained at two different fluid densities. a) Spectra of 2.0 nm ZnS nanoparticles obtained at a supercritical CO_2 density of 0.99 g mL^{-1} ; b) spectra of 6.7 nm CdS nanoparticles obtained at a supercritical CO_2 density of 0.89 g mL^{-1} .

emission spectra of the stabilized ZnS nanoparticles obtained at two different densities of carbon dioxide are shown. A red shift of 23 nm (from 263 to 286 nm) and an increment in the FWHM from 22 to 30 nm , are observed in the excitation spectra when the density of the solvent decreased from 0.99 to 0.89 g mL^{-1} . These results are in agreement with an increment in the average size of the ZnS particles from 2.0 ± 0.3 to $6.7 \pm 0.9 \text{ nm}$, when the synthesis of the materials is carried out at lower fluid densities. Similarly to what we observed for CdS nanoparticles, the emission spectra of ZnS nanoparticles appear to be due to the surface defects^[37,38], with a red shift in the fluorescence wavelength from 340 to 373 nm when the size of the ZnS nanoparticles increased. Fluorinated-thiol seems not to be effective for passivation of the surface defects on CdS and ZnS nanoparticles.

The reaction time is another factor that may influence the size of the CdS and ZnS nanoparticles synthesized by the CO_2 -microemulsion method. In the case of the synthesis of CdS nanoparticles we decided to discontinue the reaction after six minutes to avoid further aggregation as indicated by our spectroscopic observation (through a red shift and a decrease in the surface plasmon absorption peak) when the reaction time was extended (see Experimental Section for details). By increasing the reaction time to 90 minutes, the average size of the CdS nanoparticles (obtained by analysis of the TEM data) increased from 7.0 ± 0.9 to $12 \pm 2 \text{ nm}$ when scCO_2 at 220 atm and 40°C was employed ($[\text{FAOT}] = 10 \text{ mM}$, $W = 10$). Tuning of CdS nanoparticles by density variation appears to work well at short reaction times where the exchange-channel mechanism and the micellar-templating effect dominate. For very long reaction times, as the nanoparticles grow larger, the surfactant might act as a dis-

persant ligand^[18] and sterically stabilizes the nanoparticles without involving the microemulsion. Conversely, in the case of ZnS nanoparticles, the reaction time seems not to affect the final particle size. When the reaction time was extended from 16 to 90 minutes, the size of the nanoparticles remained statistically unchanged. This result is in agreement with the spectroscopic study performed during the synthesis of ZnS nanoparticles, showing an increment in the absorption maximum (at 280 nm) in the first 16 minutes and remaining constant afterwards for at least 120 minutes. The reason for this behaviour is uncertain but might be related to a different mechanism of formation of the nanoparticles and/or to a better stabilization of the ZnS nanoparticles by the micelle system (once they reach the final size) against further aggregation.

Conclusion

In summary, we have shown that the size of CdS and ZnS nanoparticles synthesized by the scCO₂ microemulsion-templating method can be continuously tuned by density variation of the fluid phase, in a similar fashion as we demonstrated previously for Ag nanoparticles.^[19] This approach gave consistent results in both nanomaterials for two different W values and for two different concentrations of surfactant tested. For the case of ZnS nanoparticles, the variation in the size of the nanoparticles with the density of the solvent (which follows a linear relationship) may not depend on the stage of the synthetic process at which the nanoparticles are stabilized. On the other hand, the time at which the stabilization of CdS nanoparticles takes place seems to be crucial to avoid further aggregation. Other parameters like the nature of the nanoparticles and the solvent may affect as well.

This study, together with the one reported for silver nanoparticles,^[19] have shown, that water-in-supercritical CO₂ microemulsions seem to be effective systems for the tunable-size synthesis of a diversity of nanomaterials by varying the density of the fluid.

Experimental Section

The surfactant used in this study, sodium bis(2,2,3,3,4,4,5,5-octafluoro-1-pentyl)-2-sulfoacetate (F-AOT), was prepared in our lab following the procedure by Liu and Erkey^[30] with some modification. Cadmium nitrate (Cd(NO₃)₂) was obtained from Aldrich with purity 99.999%, zinc nitrate (Zn(NO₃)₂) was obtained from Fisher Scientific with a purity of 99.1%, while sodium sulfide (Na₂S > 99.8%) was obtained from Aldrich. The stabilizer or protecting agent, 1H,1H,2H,2H-perfluorodecanethiol (F-thiol) 97% was purchased from Aldrich.

The liquid CO₂ was metered with an ISCO syringe pump (model 260 D) and pump controller (series D) and introduced to the high-pressure reactors via stainless steel tubing (1/16 inch o.d., 0.03 inch i.d.). The high-pressure vessels were heated with a thermal block and the temperature was kept constant at $\pm 0.1^\circ\text{C}$ and controlled with a J-type sensor and an Omega digital controller. Three homemade high-pressure vessels were utilized. One vessel (18.5 mL volume) was equipped with a fiber-optic

system (3 mm path length) and connected to a CCD array UV-VIS spectrometer (Spectral Instruments model SI-440, Tucson, AZ).^[40] The spectrometer is capable of recording a full spectrum from 240 to 900 nm in 2 s. It can also measure the change in absorbance with time at a fixed specific wavelength. The second vessel was a 17 mL high-pressure view cell with sapphire windows. The last one was a 17.5 mL vessel with a movable piston. The high-pressure vessels were connected to each other via 1/16 in stainless steel tubing. Each system was isolated from the others by HIP high-pressure valves.

The cloud points for the microemulsion containing the Cd²⁺ ions, Zn²⁺ ions and the CdS and ZnS nanoparticles were studied using a view-cell connected to a piston (both immersed in a thermal bath) and by visual observation of the phase behavior. At 40°C, a W (water to surfactant ratio) value of 10, and a surfactant concentration of 10 mM, the cloud point of a Cd²⁺ ion (Aqueous concentration 0.3 M) microemulsion was found to be 145 \pm 2 atm. In the case of Zn²⁺ ion (Aqueous concentration 0.3 M) the cloud point was 130 \pm 2 atm under identical conditions. Above these pressures at 40°C, the microemulsion is stable and is optically transparent. The cloud point boundary is approximately linear in a pressure versus temperature plot with a slope of 3.63 atm °C⁻¹ for the case of Cd²⁺ microemulsions and with a slope of 2.50 atm °C⁻¹ for the case of Zn²⁺ microemulsions. Our experiments were performed above the cloud point pressure to the limit of our high pressure system which is about 450 atm. The variation in density of scCO₂ at different temperature and pressure is known.^[41]

The semiconductor nanoparticles were synthesized by mixing two water-in-supercritical CO₂ (scCO₂) microemulsions, one containing a cadmium nitrate solution or zinc nitrate solution (0.3 M) and the other containing an aqueous solution of sodium sulfide (0.6 M). The microemulsion containing the sulfur ion was pushed into the metal ions' microemulsion using the piston cell. Formation of the CdS and ZnS nanoparticles after the mixing was monitored spectroscopically, using the optical fiber cell, by taking the absorption spectra *in situ* every two seconds. A blank measurement was taken before the reaction to provide a spectroscopic baseline, using a water-in-scCO₂ microemulsion containing deionized water. The characteristic absorption peak due to the quantum confinement properties of CdS nanoparticles ($\lambda \approx 330$ nm) was found to increase to a maximum at about 6 min after the mixing, and started to decrease gradually in intensity and reached a plateau in about 125 minutes. A red shift of 33 nm (330 to 363 nm) of the absorption peak wavelength, when going from 6 to 90 min of reaction time was noticed. This, together with the decrease in peak intensity, should indicate that the concentration of the nanoparticles reaches a maximum in the first 6 min and it is followed by a decrease in their concentration, probably attributable to aggregation.^[42] In the case of ZnS nanoparticle synthesis, the characteristic absorption peak appeared at 280 nm and it was found to increase and reach a plateau after 16 min. At that point of the reaction the peak intensity was constant (remaining in that way for more than 120 min). It seems that, unlike the CdS nanoparticles, ZnS nanoparticles do not experience further aggregation after they reach the final size.

In the case of CdS nanoparticle synthesis, the F-thiol stabilizer (1H,1H,2H,2H-perfluorodecanethiol) was introduced to the system, via a six-port injector valve, at exactly 6 min after the mixing; while in the case of ZnS nanoparticle synthesis, the stabilizer was added after the first 16 min. The F-thiol-stabilized CdS or ZnS nanoparticles were collected in an acetone solution after depressurizing the system for TEM measurements. The protected semiconductor nanoparticles are stable in acetone or ethanol for several days and the unprotected CdS and ZnS nanoparticles in either solvent would precipitate after approximately 15 min. TEM images were obtained with a JEOL 1200 EX II transmission electron microscope at an accelerating voltage of 120 kV. EDS analysis was carried out with a LEO Supra 35 VP Field Emission Scanning Electron Microscope (FESEM). EDS analysis of the stabilized nanoparticles showed only cadmium or zinc, carbon, oxygen, fluorine, sulfur and sodium in the samples. The last one may be coming originally from the sodium sulfide precursor. The average size of the nanoparticles was obtained from the TEM micrographs by counting at least 300 particles using interactive imaging software (Matrox Inspector) from Matrox Electronic Systems

(Dorval, Quebec, Canada). An important feature of this software is that it can measure a large number of particles without bias or human error.

Acknowledgements

This work was supported by a grant from DOD-AFOSR (F49620-03-1-0361) and by the Idaho DOE-EPSCoR program (DE-FG02-04ER46142).

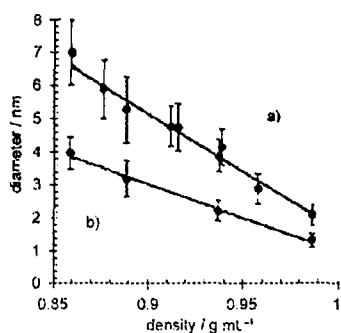
- [1] A. P. Alivisatos, *Science* **1996**, *271*, 933–937.
- [2] C. Tojo, M. C. Blanco, M. A. Lopez-Quintela, *Langmuir* **1997**, *13*, 4527–4534.
- [3] R. Rosetti, R. Hull, J. M. Gibson, L. E. Brus, *Chem. Phys.* **1985**, *92*, 100, 552–559.
- [4] a) C. M. Niemeyer, *Angew. Chem.*, **2001**, *113*, 4254–4287; b) C. M. Niemeyer, *Angew. Chem. Int. Ed.* **2001**, *40*, 4128–4158.
- [5] C. A. Mirkin, *Inorg. Chem.* **2000**, *39*, 2258–2272.
- [6] S. R. Whaley, D. S. English, E. L. Hu, P. F. Barbara, A. M. Belcher, *Nature* **2000**, *405*, 665–668.
- [7] D. Ishii, K. Kinbara, Y. Ishida, N. Ishii, M. Okochi, M. Yohda, T. Aida, *Nature* **2003**, *423*, 628–632.
- [8] M. J. Meziani, Y.-P. Sun, *J. Am. Chem. Soc.* **2003**, *125*, 8015–8018.
- [9] J. D. Holmes, P. A. Bhargava, B. A. Korgel, K. P. Johnston, *Langmuir* **1999**, *15*, 6613–6615.
- [10] H. Ohde, M. Ohde, F. Bailey, H. Kim, C. M. Wai, *Nano Lett.* **2002**, *2*, 721–724.
- [11] P. S. Shah, J. D. Holmes, R. C. Doty, K. P. Johnston, B. A. Korgel, *J. Am. Chem. Soc.* **2000**, *122*, 4245–4246.
- [12] P. S. Shah, J. D. Holmes, K. P. Johnston, B. A. Korgel, *J. Phys. Chem. B* **2002**, *106*, 2545–2551.
- [13] P. S. Shah, S. Husain, K. P. Johnston, B. A. Korgel, *J. Phys. Chem. B* **2002**, *106*, 12178–12185.
- [14] J. P. Cason, K. Khambaswadkar, C. B. Roberts, *Ind. Eng. Chem. Res.* **2000**, *39*, 4749–4755.
- [15] M. A. McHugh, V. J. Krukonis, *Supercritical Fluid Extraction*, 2nd ed., Butterworth-Heinemann, Boston, MA, 1994.
- [16] M. Poliakoff, P. King, *Nature* **2001**, *412*, 125.
- [17] P. S. Shah, H. Shabbir, K. P. Johnston, B. A. Korgel, *J. Phys. Chem. B* **2002**, *106*, 12178–12185.
- [18] C. L. Kitchens, C. B. Roberts, *Ind. Eng. Chem. Res.* **2004**, *43*, 6070–6081.
- [19] C. A. Fernandez, C. M. Wai, *Small* **2006**, *2*, 1266–1269.
- [20] J.-P. Boilot, J. Biteau, A. Brun, F. Chaput, T. D. De Moraes, B. Darrauq, T. Gacoin, K. Lahlil, J.-M. Leht, Y. Levy, L. Malier, G.-M. Tsivgoulis, *Mater. Res. Soc. Symp. Proc.* **1998**, *519*, 227.
- [21] J. Y. Kim, H. Hiramatsu, F. E. Osterloh, *J. Am. Chem. Soc.* **2005**, *127*, 15556–15561.
- [22] V. Pardo-Yissar, E. Katz, J. Wasserman, I. Willner, *J. Am. Chem. Soc.* **2003**, *125*, 622–623.
- [23] M. L. Curri, A. Agostiano, G. Leo, A. Mallardi, P. Cosma, M. D. Monica, *Mater. Sci. Eng. C* **2002**, *10*, 449–452.
- [24] E. Katz, A. N. Shipway, I. Willner, *Nanoscale Materials* (Eds.: L. M. Liz-Marzan, P. Kamat), Kluwer, **2003**, pp. 5–78.
- [25] S. Santra, P. H. Holloway, R. A. Mericle, H. Yang, G. A. Walter, *PCT Int. Appl.* number **2005**, 103 pages.
- [26] T.-C. Liu, Z.-L. Huang, H.-Q. Wang, Y.-D. Zhao, Q.-M. Luo, *Proc. SPIE-Int. Soc. Opt. Eng.* **2006**, 6026.
- [27] J. Burke, *AIC Book and Paper Group Annual*, Vol. 3 (Ed: C. Jensen), publisher, city, **1984**, pp. 13.
- [28] M. L. O'Neill, Q. Cao, M. Fang, K. P. Johnston, S. P. Wilkinson, C. D. Smith, J. L. Kerschner, S. H. Jureller, *Ind. Eng. Chem. Res.* **1998**, *37*, 3067–3079.
- [29] B. Xu, G. W. Lynn, J. Guo, Y. B. Melnichenko, G. G. Wignall, J. B. McClain, J. M. DeSimone, C. S. Jr., Johnson, *J. Phys. Chem. B* **2005**, *109*, 10261–10269.
- [30] L. Motte, I. Lisicki, M. P. Pilati, in *Hydrogen Bond Networks* (Eds.: J.-C. Dore, M. C. Bellissent-Funel), NATO publisher, **1994**, pp. 447.
- [31] L. Magagni, V. Bertoni, P. L. Cavalotti, R. Maboudian, C. Carraro, *Microelectronic Engineering*, **2002**, *64*, 479–478.
- [32] W. Xu, Y. Liao, D. L. Akins, *J. Phys. Chem. B* **2002**, *106*, 11127–11131.
- [33] B. Liu, G. Q. Xu, L. M. Gan, C. H. Chew, W. S. Li, Z. X. Shen, *J. Appl. Phys.* **2001**, *89*, 1059.
- [34] H. Ohde, M. Ohde, K. H. Bailey, C. M. Wai, *Nano Lett.* **2002**, *2*, 721–724.
- [35] S. S. Honga, M. S. Leea, H. S. Hwangb, K. T. Lim, S. S. Parka, C. S. Jua, G. D. Leea, *Solar Energy Materials Sol. Cells* **2003**, *80*, 273–282.
- [36] U. Natarajan, K. Handique, A. Mehra, J. R. Bellare, K. C. Khilar, *Langmuir* **1996**, *12*, 2670–2678.
- [37] H. C. Warada, S. C. Ghosh, B. Hemtanona, C. Thanachayanontb, J. Dutta, *Sci. Technol. Adv. Mater.* **2005**, *6*, 296–301.
- [38] E. A. Turner, Y. Huang, J. F. Corrigan, *Eur. J. Inorg. Chem.* **2005**, 4465–4478.
- [39] Z.-T. Liu, C. Erkey, *Langmuir* **2001**, *17*, 274–277.
- [40] H. Ohde, F. Hunt, C. M. Wai, *Chem. Mater.* **2001**, *13*, 4130–4135.
- [41] National Institute of Standards and Technology, “Thermophysical Properties of Fluid Systems”, can be found under: <http://webbook.nist.gov/chemistry/flui>
- [42] J. Liu, P. Raveendran, Z. Shervani, Y. Ikushima, Y. Hakuta, *Chem. Eur. J.* **2005**, *11*, 1854–1860.

Received: September 1, 2006
Published online: **11**, 2007

Nanoparticles

C. A. Fernandez,
C. M. Wai* ■■■-■■■

Continuous Tuning of Cadmium Sulfide and Zinc Sulfide Nanoparticle Size in a Water-in-Supercritical Carbon Dioxide Microemulsion



Simply supercritical: The supercritical CO_2 microemulsion method represents a simple approach to use a density-tunable solvent for synthesizing size-controlled semiconductor nanoparticles over a broad range of values. The influence of CO_2 density on the average size and size distribution of, for example, CdS nanoparticles is shown.



Deposition of Metal Nanoparticles on Carbon Nanotubes via Hexane Modified Water-in-CO₂ Microemulsion at Room Temperature

Joanna Shaofen Wang, Horng-Bin Pan, and Chien M. Wai*

Department of Chemistry, University of Idaho, Moscow, Idaho 83844, USA

Carbon nanotube-supported metallic nanoparticles (Pd, Rh, and bimetallic Pd-Rh) with diameters in the range 2–10 nm can be synthesized by hydrogen reduction of metal ions dissolved in the water core of a CO₂ microemulsion in liquid CO₂ at room temperature. The microemulsion is stabilized by sodium bis(2-ethylhexyl)sulfosuccinate (AOT) and dissolved in liquid CO₂ with the aid of hexane as a modifier. The metal nanoparticles synthesized in the microemulsion can be deposited on surfaces of multi-walled carbon nanotubes (MWCNTs) by stirring in the liquid CO₂ phase. This simple method produces uniformly distributed metal nanoparticles on surfaces of the MWCNTs with high yields. The carbon nanotube-supported Pd/Rh bimetallic nanoparticles exhibit high catalytic activities for hydrogenation of aromatic compounds and can be reused without losing catalytic activity.

Keywords: Deposition, Metal Nanoparticles, Carbon Nanotubes, Liquid CO₂, Water-in-CO₂ Microemulsion.

1. INTRODUCTION

Direct deposition of metals on multi-walled carbon nanotubes (MWCNTs) using supercritical carbon dioxide (SeCO₂) as a medium has been shown to result in uniformly dispersed metal nanoparticles on CNT surfaces.^{1–5} CNT-supported metal nanoparticles often exhibit high catalytic activities for a number of chemical and electrochemical reactions which are significant for chemical synthesis and for low temperature fuel cell applications.^{6–9} The SeCO₂ deposition process typically involves hydrogen reduction of CO₂-soluble metal precursors such as metal- β -diketonates at moderately high temperatures in the presence of MWCNTs. For instance, hydrogen reduction of palladium (II)-hexafluoroacetylacetone, Pd(hfa)₂, in SeCO₂ requires 80 °C to form Pd nanoparticles on surfaces of MWCNTs.¹ Reduction of Rh(acac)₃, Pt(acac)₂, and Ru(acac)₃ (acac, acetylacetone) by hydrogen in SeCO₂ requires even higher temperatures, around 250 °C, in order to deposit these metal nanoparticles on surfaces of MWCNTs.^{1,2,10} In addition to the temperature requirement, availability of CO₂-soluble precursors for the direct SeCO₂ deposition method may also be a problem for some metals. We have recently developed a method which uses common inorganic metal salts as precursors dissolved in a

water-in-CO₂ microemulsion for making metal nanoparticles followed by their deposition on carbon nanotubes in liquid CO₂. According to our study, hydrogen reduction of metal ions and formation of metal nanoparticles in the water core of the microemulsion can be accomplished in liquid CO₂ at room temperature. When the microemulsion solution containing metal nanoparticles is in contact with the CNTs by stirring, metal nanoparticles can be deposited homogeneously on the surfaces of the nanotubes. The yield of metal nanoparticles deposited on the CNT surfaces is generally high, and about 70% of the metal ions dissolved in the microemulsion could end up as metal nanoparticles on the CNT surfaces. The synthesized metal-CNT samples were washed with methanol and sonicated several times to remove the metal particles that were not attached or not strongly adhered to the CNT surfaces before characterization. Approximately 70% of the initial metal ions could be deposited as metal nanoparticles on the CNT surfaces according to our chemical analysis of the washed samples. Bimetallic nanoparticles can also be deposited on CNT surfaces using this method by starting with a mixture of two different metal salts in the water core of the microemulsion. Our procedures of synthesizing single Pd and Rh nanoparticles and binary Pd/Rh nanoparticles in liquid CO₂ are given in this paper. Some results of hydrogenation reactions with aromatic compounds catalyzed by the MWCNT-supported metal nanoparticles are also given to illustrate their high activities.

*Author to whom correspondence should be addressed.

2. EXPERIMENTAL PROCEDURES

The microemulsion was prepared in hexane using an aqueous solution containing desired metal ions and sodium *bis*(2-ethylhexyl)sulfosuccinate (AOT) as a surfactant. Using hexane as a co-solvent, the AOT microemulsion becomes soluble in liquid CO₂. The amount of hexane used in our procedure was around 8.5–10% by volume in liquid CO₂. This amount of hexane forms one phase with liquid CO₂ at room temperature. The stability of the AOT microemulsion in liquid CO₂ with different amounts of hexane was investigated using a 20 mL high-pressure view-cell with quartz windows. A typical procedure started with 54 μ L of 0.1 M Na₂PdCl₄, 133 mg of AOT (15 mM, $W = [H_2O]/[AOT] = 10$), and 2 mL (10% of cell volume) of hexane placed in the view-cell. A magnetic stirrer was used to mix the solution to form AOT microemulsion at room temperature. Liquid CO₂ was introduced into the view-cell with continuous stirring for 1 hour for each pressure to dissolve the hexane solution containing the AOT microemulsion. The microemulsion became optically transparent at 160 atm or higher pressures with 10% of hexane in liquid CO₂. We chose 200 atm as the pressure for synthesizing metal nanoparticles in this method.

For hydrogen reduction of metal ions, a reservoir composed of 12 atm of H₂ in 180 atm of CO₂ was introduced into the high pressure view cell placed with a hexane solution containing an AOT microemulsion with a known metal ion concentration. The final pressure of the system was charged to 200 atm by adding CO₂ from an ISCO pump. The system at that pressure was agitated with a magnetic stirrer for an hour. After investigation of phase behavior and stability of water-in-CO₂ microemulsion, experiments were then performed with a stainless-steel reaction cell with a volume of 35.3 mL.

To make CNT supported Pd nanoparticles, 98 μ L of 0.1 M Na₂PdCl₄ at $W = [H_2O]/[AOT] = 10$, 234 mg of AOT (15 mM), 3.0 mL of hexane, and 3~5 mg of treated MWCNTs were placed in a mini glass beaker and a magnetic stirrer was used to agitate this water-in-oil microemulsion for 20 min. After that, the beaker was loaded into the 35.3 mL stainless-steel reactor. This was followed by the hydrogen reduction process described in the previous paragraph. Microemulsions at this stage can be formed when MWCNTs are mixed with metal ion solution, AOT, and hexane according to our visual observation of a blackish transparent phase without liquid droplets using a high-pressure view cell.

Hexane serves two purposes in the CNT-supported metal nanoparticles synthesis. First, it is used as a co-solvent for dissolution of the AOT microemulsion in liquid CO₂. Alkane with a medium chain length, such as hexane, is known to increase the solubility of AOT and assist surfactant aggregation in supercritical CO₂. Second, hexane is used as a solvent to collect the CNT-supported metal nanoparticles synthesized in the system. As the pressure

of the system is reduced, a single reversed micellar phase becomes unstable and two phases are formed consisting of an AOT-hexane-rich liquid phase and a predominant CO₂ upper phase. The nanoparticles attached CNT can be retained by AOT-hexane-rich liquid phase on the bottom. This makes the recovery of the CNT-supported metal nanoparticle products easy to accomplish. Without a liquid solvent, the CNTs would be dispersed on the walls of the reaction system that is difficult to recover quantitatively. Our choice of 8.5–10% of hexane (of cell volume) in liquid CO₂ for the synthetic process was based on the fact that this amount of hexane would accomplish both purposes.

To make CNT supported bimetallic Pd/Rh nanoparticles, 49 μ L of 0.1 M Na₂PdCl₄ and 49 μ L of 0.1 M RhCl₃ at $W = [H_2O]/[AOT] = 10$, 234 mg of AOT (15 mM), 3 mL of hexane, and 3~5 mg of treated MWCNTs were added to a mini glass beaker and loaded into the 35.3 mL volume stainless-steel reactor. The hydrogen reduction process is identical to that described previously for the single metal nanoparticles synthesis.

The MWCNTs (NanoLab, Inc., Newton, MA) were functionalized before metal deposition as described in the literature.^{1,2} Transmission electron microscopy (TEM) images of the decorated CNT were taken using a Jeol TEM 1200 microscope equipped with an Oxford ISIS system. To obtain TEM images, the as-synthesized nanoparticles were dispersed in ethanol under sonication for 1 min and were then deposited on a carbon coated copper grid. X-ray photoelectron spectroscopy (XPS) analysis was performed using a Kratos AXIS 165 multi-technique electron spectrometer to confirm the presence of metal nanoparticles. X-ray diffraction (XRD) patterns were obtained using a Siemens D5000. Energy dispersive X-ray spectroscopy (EDS) was performed using LEO SUPRA 35 VP (FESEM). A 300 MHz NMR (Bruker AMX 300) was used for identification of products from hydrogenation reactions catalyzed by the CNT-supported nanoparticle catalysts.

3. RESULTS AND DISCUSSION

The stabilities of water-in-liquid CO₂ microemulsions at different pressures have been reported by several research groups.^{11–15} The surfactants used in the previous studies are typically fluorinated ones which are soluble in liquid or supercritical CO₂. However, fluorinated surfactants are often expensive, difficult to obtain, and sometimes toxic. One of the common surfactants widely used in the formation of water-in-oil microemulsions is the anionic surfactant sodium *bis*(2-ethylhexyl)sulfosuccinate (AOT), which unfortunately is not soluble in CO₂. Because of high cost and potential toxicity of fluorinated surfactants, approaches for stabilizing water-in-CO₂ microemulsions using co-surfactants or co-solvents have been developed.^{16–19} The binary hexane-CO₂ phase behavior has been studied previously.^{20–22} Our experiments indicate that with hexane with 8.5–10% by volume of CO₂ in liquid CO₂ at pressures

>160 atm, the AOT microemulsion with a *W* value around 10 is stable for metal nanoparticle synthesis at room temperature. The synthesized nanoparticles can be transferred to the surfaces of CNTs by rigorous mixing. Upon slow depressurization of the system, the CNT-supported metal nanoparticles would remain in the separated hexane phase and could be easily collected for further cleaning, characterization, and applications.

Direct hydrogenation of the Pd^{2+} containing microemulsion in hexane with 5 mg of CNT and 3 mL of hexane would result in large Pd clusters not uniformly distributed on the CNT surfaces. If a smaller CNT to hexane ratio was used (e.g., 5 mg CNT in 50 mL of hexane), then uniformly distributed Pd nanoparticles could be formed using the water-in-hexane microemulsion method. One function of the liquid CO_2 in our method is to replace the large amount of hexane required for dispersion and deposition of Pd nanoparticles on the CNT surfaces.

Typical TEM images of the Pd, Rh, and Pd/Rh nanoparticles synthesized using water-in- CO_2 microemulsions in hexane modified liquid CO_2 are present in Figure 1. Figures 1a, 1b, and 1c are Pd, Rh (monometallic) and Pd/Rh (bimetallic) nanoparticles, respectively. As expected, characteristic spherical Pd, Rh, and Pd/Rh nanoparticles with narrow size distributions are observed. The little spherical dark spots which represent the Pd, Rh, or Pd/Rh nanoparticles are closely attached to the CNT surfaces. The nanoparticles have a size distribution range of approximate 2–10 nm. Particle size and size distribution are probably

controlled by both the *W* value ($[\text{H}_2\text{O}]/[\text{AOI}]$) of the microemulsion and the surface curvature of the carbon nanotubes. Using our method, the particle size range is similar to those reported recently using a water-in-oil microemulsion for depositing metal nanoparticles on carbon nanotubes.²³ Without the microemulsion, reduction of a metal salt solution in a solvent such as methanol dissolved in liquid CO_2 , would result in large metal clusters. For example, when 98 μL of 0.1 M Na_2PdCl_4 solution in 0.5 mL methanol plus the CNTs were placed in the reaction cell with 12 atm of H_2 and a total pressure ($\text{H}_2 + \text{CO}_2$) = 200 atm, the resulting Pd particles on the CNT surface are shown in Figure 1d. Without the microemulsion, the dispersion of metal ions in condensed CO_2 phase is probably unattainable and the size of the resulting metal particles is uncontrollable.

The curvature of the carbon nanotubes is considered a controlling factor for attachment of a certain range of metal nanoparticles to the nanotube surfaces using a direct supercritical fluid deposition method.¹¹ Larger particles probably would fall off from the nanotube surfaces during the deposition process for MWCNTs with smaller diameters.

Two possible mechanisms are probably responsible for the formation of metal nanoparticles on CNT surfaces using the CO_2 microemulsion method. In the first mechanism, the reduced metal atoms aggregate in the water core of the microemulsion forming nanoparticles in the fluid phase. In the second mechanism, collisions between the microemulsions would alter the metal nanoparticle size

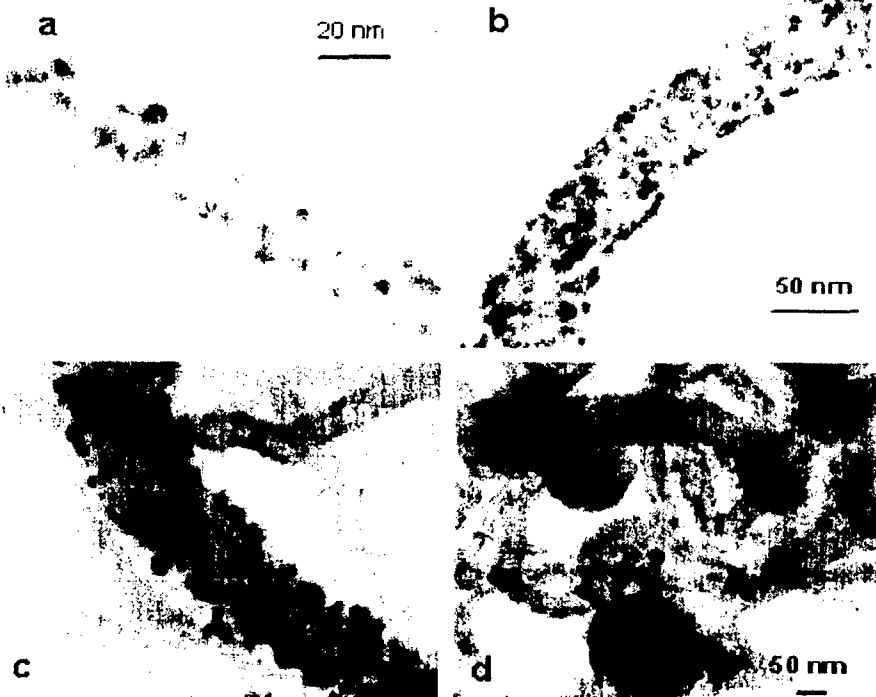


Fig. 1. TEM images of metallic nanoparticles deposited on MWCNTs using the microemulsion method. a: Pd; b: Rh; c: Pd/Rh; d: Na_2PdCl_4 in CH_3OH with CNTs and H_2/CO_2 without microemulsion.

through exchange of materials during collision. The metal nanoparticles could be stabilized by adhesion to the CNT surfaces. If the size of the metal nanoparticles is too large for attachment to the CNT surface, these nanoparticles would fall off due to the curvature limitation. The variation in particle size distribution of the metal particles observed on CNT surfaces probably is a combination of these two mechanisms.

The EDS spectra of the CNT-supported monometallic nanoparticles (Pd and Rh) indicate that Pd and Rh nanoparticles exhibit distinctive peaks which are consistent with the energy channels of palladium and rhodium elements. The method of making monometallic nanoparticles in liquid CO_2 using water-in- CO_2 microemulsions is also suitable for making bimetallic nanoparticles. The composition of different metals can be controlled by simply varying the starting concentration of the metal-ion solution.⁸ By using two metal ion solutions, e.g., Na_2PdCl_4 and RhCl_6 , to make the microemulsion, the average composition of the bimetallic nanoparticles deposited on the CNTs would be close to the ratio of the Pd:Rh present in the initial salt solution. For instance, when PdCl_4^{2-} and Rh^{4+} solutions with the initial concentration of 0.1 M and 0.2 M, respectively, were used in 1:1 volume ratio for the preparation of the microemulsion, the final Pd:Rh ratio in the resulting nanoparticles was 1:1.94.

XRD spectra also confirm that the nanoparticles on MWCNTs in Figure 1a (TEM) are Pd metal located at 2θ values of 40.114° (Fig. 2, top). The CNT-supported Rh nanoparticles are also identified by XRD with 2θ values of 41.068° consistent with Rh metal (Fig. 2, middle). Diffraction peaks of binary Pd/Rh nanoparticles shift to higher 2θ values with respect to the characteristic peaks of pure Pd. The shift in 2θ corresponds to a decreased lattice constant for Pd due to the incorporation of a Rh atom. For the Pd/Rh bimetallic system, the 1:1 atom ratio is equivalent to 50 atom% of Pd and the shift in 2θ would be proportional to the atomic percentage of Pd and Rh according

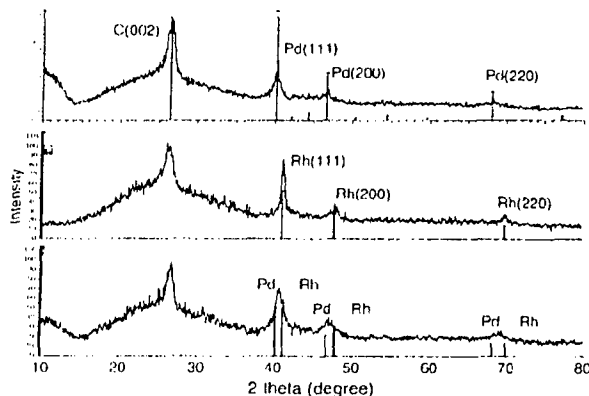


Fig. 2. XRD spectra of Pd (top), Rh (middle), and Pd/Rh (bottom) nanoparticles deposited on MWCNTs using the microemulsion method in liquid CO_2 .

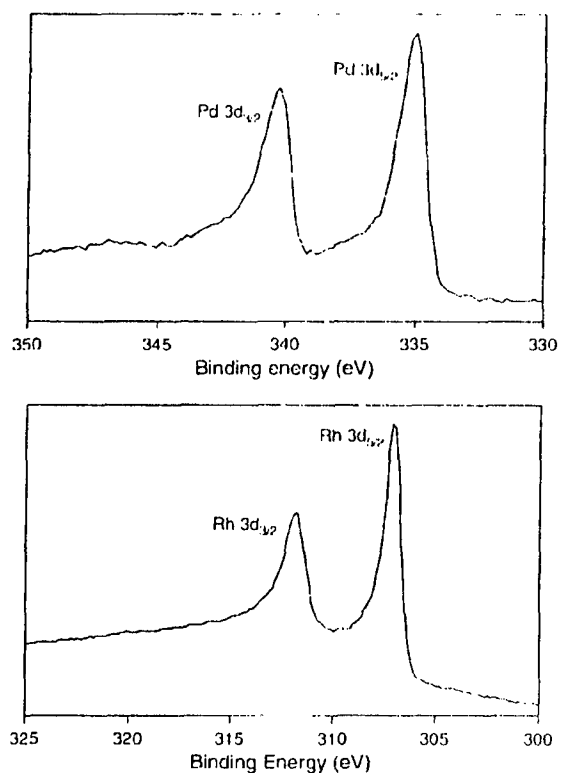


Fig. 3. XPS spectrum of Pd $3d_{5/2}$ and $3d_{3/2}$ from CNT-supported Pd nanoparticle synthesized by the microemulsion method (top); XPS spectrum of Rh $3d_{5/2}$ and $3d_{3/2}$ from CNT-supported Rh nanoparticle synthesized by the microemulsion method (bottom)

to the Vegard Law.^{24–25} Our XRD data (Fig. 2, bottom) appear consistent with the predicted 2θ of 40.591° for the Pd/Rh mixture and support the formation of Pd and Rh crystallites. The 2θ diffraction peak at 26.4° is a carbon peak (002) from MWCNTs.

XPS spectra also indicate the monometallic Pd and Rh nanoparticles on CNTs are palladium (Fig. 3, top) and rhodium (Fig. 3, bottom) metals. The CNT-supported Pd and Rh nanoparticles show Pd and Rh zero-valent metals with $3d_{5/2}$ at 335.1 and 307.1 eV, respectively, as shown in Figure 3. The binding energies of the spectral lines 335.1 eV for the Pd $3d_{5/2}$ peak and 340.3 eV for the Pd $3d_{3/2}$ peak are in agreement with those reported in the literature for the zero-valent Pd metal (Pd $3d_{5/2}$ for 335.2 eV, and Pd $3d_{3/2}$ for 341.1 eV, respectively).^{26–28} Again, the binding energies of the spectral lines at 307.1 eV for the Rh $3d_{5/2}$ peak and 311.8 eV for the Rh $3d_{3/2}$ peak are consistent with those reported zero-valent state of Rh element (Rh $3d_{5/2}$ for 307.2 eV,²⁹ and Rh $3d_{3/2}$ for 312.0 eV,³⁰ respectively). The XPS spectra shown in Figure 3 are also similar to those reported for the metallic Pd and Rh nanoparticles deposited on the surfaces of CNTs using the direct supercritical CO_2 deposition method.²

The catalytic activities of the CNT-supported nanoparticles including Pd, Rh, and Pd/Rh were tested for

Table I. Comparison of catalytic activities of Pd and Rh nanoparticles deposited on MWCNTs in hydrogenation of naphthalene

Reactant	Catalyst	Conversion%	Tetralin	Decalin
Naphthalene	Pd/Rh CNT	100	0	100
Naphthalene	mixture	43	3	40
	Pd/CNT/ Rh CNT			
Naphthalene	Pd/CNT	0.7	0.7	0
Naphthalene	Rh/CNT	100	73	27
Naphthalene	Pd/C (10%)	1	1	0
Naphthalene	Rh/C (5%)	0.2	0.2	0

10 mg of nanoparticle CNT and 20 mg of naphthalene in hexane at 10 atm H₂, measured by ¹H NMR

hydrogenation of naphthalene under 10 atm H₂ at room temperature in hexane. Ten mL of *n*-hexane, 10 mg of a CNT catalyst and 20 mg of naphthalene were added into an Erlenmeyer flask which was then placed in a high-pressure stainless steel vessel with a magnetic stirrer. Hydrogen gas (10 atm pressure) was bubbled through the system for 1 hour. The results are given in Table I. Compared with CNT-supported Pd nanoparticles, CNT-supported Rh nanoparticles show a much higher activity for catalytic hydrogenation of naphthalene under the same experimental conditions. The results from ¹H NMR analysis indicated that if using CNT-supported Rh nanoparticles, the products of tetralin and decalin converted from naphthalene were 73% and 27%, respectively, while with Pd/CNT, it showed a low catalytic activity (0.7% conversion of tetralin). When using CNT-supported bimetallic Pd/Rh (1:1) nanoparticles, only one product, decalin (located at 1.2–1.8 ppm as shown in Fig. 4) was detected and naphthalene disappeared completely (100% conversion).

When a mixture (1:1) of monometallic Pd/CNT and Rh/CNT was used as the catalyst, conversion of tetralin and decalin from naphthalene was 3% and 40%, respectively, with a total conversion of 43%. The catalytic

activity of the bimetallic Pd/Rh nanoparticles apparently is much higher than a mixture of two monometallic nanoparticles. Catalytic hydrogenation of naphthalene was also studied using a commercial Pd/carbon (Pd 10%) and a Rh/carbon (Rh 5%) catalyst. The conversion of naphthalene catalyzed by Pd/C and Rh/C was 1%, and 0.2%, respectively, under the same experimental conditions, as shown in Table I.

The CNT-supported nanoparticle catalyst can be recycled after hydrogenation reactions. If a small amount of methanol was added to the reaction flask and stirred for 10 min, the CNT catalyst would stay in the methanol phase (bottom phase) with hexane containing the products in the upper phase. After drying the methanol solution in a hood, the CNT-supported metal nanoparticle catalyst could be recovered and reused for the next cycle of catalysis. The CNT-supported Pd/Rh nanoparticle catalyst was reused 5 times without losing activity.

4. CONCLUSIONS

This study has demonstrated that CNT-supported metallic nanoparticles can be synthesized via a water-in-CO₂ microemulsion in hexane modified liquid CO₂ at room temperature. This method requires only common inorganic metal salts as starting materials. Hexane is used as a cosolvent to dissolve the AOT microemulsion and as a solvent to collect the synthesized CNT-supported nanoparticle catalysts. The amount of hexane used in this method is significantly less than that required for the water-in-hexane microemulsion method.

TEM, EDS, XRD, and XPS analyses confirm the formation of monometallic (Pd, Rh) and bimetallic (Pd/Rh) nanoparticles stabilized on MWCNTs. The Pd/Rh bimetallic nanoparticles are more effective catalysts than monometallic nanoparticles for hydrogenation of aromatic compounds such as naphthalene in an organic solvent. This inorganic route of synthesizing and stabilizing nanoparticles on MWCNTs via a water-in-CO₂ microemulsion, in principle, can be applied to study many bimetallic and/or multi-metallic nanoparticle systems. It may lead to development of new catalysts for chemical and electrochemical process that may have a wide range of potential applications from organic synthesis to fuel cell applications.

Acknowledgment: This work was supported by a grant from DOD-AFOSR (F49620-03-1-0361).

References and Notes

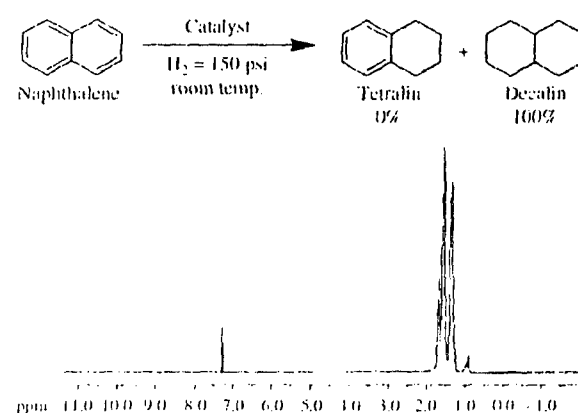


Fig. 4. ¹H NMR spectrum of the hydrogen reduction product (decalin) from naphthalene catalyzed by the CNT-supported Pd/Rh nanoparticles. (10 mg of Pd/Rh-CNT and 20 mg of naphthalene at H₂ pressure 10 atm in hexane at room temperature, reaction time 1 hour)

1. X. R. Ye, Y. Lin, and C. M. Wai, *Chem. Commun.* 642 (2003)
2. X. R. Ye, Y. Lin, C. Wang, M. H. Engelhard, Y. Wang, and C. M. Wai, *J. Mater. Chem.* 14, 908 (2004)
3. R. Giordano, P. Serp, P. Kallek, Y. Kihn, J. Schreiber, C. Marhic, and J. L. Duvail, *Eur. J. Inorg. Chem.* 4, 610 (2003)
4. X. R. Ye, Y. Lin, C. M. Wai, J. B. Tallot, and S. H. Jin, *J. Nanosci. Nanotechnol.* 5, 964 (2005).

5. X. R. Ye, H. F. Zhang, Y. Lin, L. X. Wang, and C. M. Wu, *J. Nanosci. Nanotechnol.* 4, 83 (2004).
6. Y. Lin, X. Cui, H. C. Yen, and C. M. Wu, *J. Phys. Chem. B* 109, 13410 (2005).
7. X. R. Ye, Y. Lin, C. Wang, and C. M. Wu, *Adv. Mater.* 15, 316 (2003).
8. N. Zheng and K. Y. Chan, *J. Mater. Chem.* 12, 1203 (2002).
9. Y. Lin, Y. Huang, X. X. Ding, C. Cheng, C. Tang, and S. R. Q. J. Nanosci. Nanotechnol. 5, 932 (2005).
10. C. H. Yen, X. Cui, H. B. Pan, S. Wang, Y. Lin, and C. M. Wu, *J. Nanosci. Nanotechnol.* 5, 1853 (2005).
11. T. Eastoe, A. Downer, P. Alison, D. C. Steyler, E. Ramsey, T. Pentol, and R. K. Heenan, *Phys. Chem. Chem. Phys.* 2, 5335 (2000).
12. T. Eastoe, B. M. H. Cazelles, D. C. Steyler, T. D. Holmes, A. R. Pitt, T. J. Wear, and R. K. Heenan, *Langmuir* 13, 6980 (1997).
13. T. D. Holmes, D. C. Steyler, G. D. Rees, and B. H. Robinson, *Langmuir* 14, 6371 (1998).
14. C. T. Jr. Lee, P. A. Pashas, K. J. Ziegler, K. P. Johnston, H. J. Dat, H. D. Cochran, Y. B. Melnichenko, and G. D. Wignall, *J. Phys. Chem. B* 104, 11094 (2000).
15. J. S. Keiper, R. Simhan, and J. M. DeSimone, *J. Am. Chem. Soc.* 124, 1831 (2002).
16. G. J. McEwan, K. P. Johnston, and S. M. Howdle, *Am. Inst. Chem. Eng. J.* 40, 543 (1994).
17. M. Zhong, B. Hao, H. Yan, and D. Y. Peng, *Fluid Phase Equilibria* 134, 175 (1997).
18. J. M. Dobbs, J. M. Wong, R. J. Lahiere, and K. P. Johnston, *Ind. Eng. Chem. Res.* 26, 56 (1987).
19. J. Lin, B. Han, F. Zhang, F. Xu, G. Li, W. Wu, and G. Yang, *Fluid Phase Equilibria* 211, 265 (2003).
20. I. Leder and C. A. Traub, *J. Chem. Eng. Data* 20, 323 (1975).
21. S. T. Cai, H. D. Cochran, and P. T. Cummings, *J. Phys. Chem. B* 103, 3485 (1999).
22. M. Mukhopadhyay and S. V. Daler, *J. Supercrit. Fluids* 29, 223 (2004).
23. B. Yoon and C. M. Wu, *J. Am. Chem. Soc.* 127, 17174 (2005).
24. M. Watanabe, M. Uchida, and S. Motoo, *J. Fluorinated Chem.* 39, 395 (1987).
25. J. Park and J. Cheon, *J. Am. Chem. Soc.* 123, 8713 (2001).
26. I. Hedman, M. Klasson, R. Nilsson, C. Nordling, M. P. Sorokina, I. Klyushnikova, S. A. Neimomov, V. A. Trapeznikov, and V. G. Zyrakov, *Phys. Scripta* 4, 195 (1971).
27. Y. Baer, P. E. Heden, I. Hedman, M. Klasson, C. Nordling, and K. Siegbahn, *Phys. Scripta* 1, 55 (1970).
28. A. Tressaud, S. Khatton, H. Touhara, and N. Watanabe, *Z. Anorg. Allg. Chem.* 540, 541, 291 (1986).
29. C. D. Wagner, W. M. Riggs, L. E. Davis, J. B. Moulder, and G. E. Muilenberg, *Handbook of X-Ray Photoelectron Spectroscopy*, Perkin-Elmer Corporation, Physical Electronics Division, Eden Prairie, Minn. 55344 (1992).
30. J. F. Moulder, W. F. Stickle, P. E. Sobol, and K. D. Bomben, *Handbook of X-ray Photoelectron Spectroscopy*, edited by J. Chastan, Perkin-Elmer, Eden Prairie, MN (1992).

Received: 19 October 2005; Revised/Accepted: 1 May 2006

PtRu/Carbon Nanotube Nanocomposite Synthesized in Supercritical Fluid: A Novel Electrocatalyst for Direct Methanol Fuel Cells

Yuehe Lin* and Xiaoli Cui†

Pacific Northwest National Laboratory, 902 Battelle Boulevard, P.O. Box 999, Richland, Washington 99352

Clive H. Yen and Chien M. Wai*

Department of Chemistry, University of Idaho, Moscow, Idaho 83844

Received May 12, 2005. In Final Form: September 2, 2005

Platinum/ruthenium nanoparticles were decorated on carbon nanotubes (CNT) in supercritical carbon dioxide, and the nanocomposites were characterized by transmission electron microscopy (TEM) and X-ray diffraction (XRD). TEM images show that the particles size is in the range of 5–10 nm, and XRD patterns show a face-centered cubic crystal structure. Methanol electrooxidation in 1 M sulfuric acid electrolyte containing 2 M methanol were studied on PtRu/CNT (Pt, 4.1 wt%; Ru, 2.3 wt%; molar ratio approximately Pt/Ru = 45:55) catalysts using cyclic voltammetry, linear sweep voltammetry, chronoamperometry, and electrochemical impedance spectroscopy. All the electrochemical results show that PtRu/CNT catalysts exhibit high activity for methanol oxidation which resulted from the high surface area of carbon nanotubes and the nanostructure of platinum/ruthenium particles. Compared with Pt/CNT, the onset potential is much lower and the ratio of forward anodic peak current to reverse anodic peak current is much higher for methanol oxidation, which indicates the higher catalytic activity of PtRu/CNT. The presence of Ru with Pt accelerates the rate of methanol oxidation. The results demonstrated the feasibility of processing bimetallic catalysts in supercritical carbon dioxide for fuel cell applications.

Introduction

Direct methanol fuel cells (DMFC) are considered as one of the most promising options to solve the future energy problem because of their high energy conversion efficiency, low pollutant emission, low operating temperature, and simplicity of handling and processing of liquid fuel.^{1,2} Electrocatalysts with higher activity for methanol oxidation at room temperature are critically needed to enhance their performance for commercial device applications. It is well-known that platinum is the only single-component catalyst that shows a significant activity for methanol oxidation. Pure platinum, however, is readily poisoned by CO, the byproduct in methanol electrooxidation. Considerable efforts have been devoted to design and synthesize Pt-based alloy catalysts with higher poison tolerance and greater methanol oxidation activity. Improved activity has been observed by alloying platinum with one or two other elements such as Ru,^{3–10} Sn,^{11,12} Ni,^{13,14} Os,^{15,16} Bi,¹⁷ Pb,¹⁸

* To whom correspondence should be addressed. E-mail: yuehe.lin@pnl.gov (Y.L.); cmai@uidaho.edu (C.M.W.). Tel: 509-376-0529 (Y.L.). Fax: 509-376-5106 (Y.L.).

† Permanent address: Department of Materials Science, Fudan University, Shanghai, 200433, China.

- (1) Ario, A. S.; Srinivasan, S.; Antonucci, V. *Fuel Cells* 2001, 1, 133.
- (2) Chan, K. Y.; Ding, J.; Ren, J. W.; Cheng, S. A.; Tsang, K. Y. *J. Mater. Chem.* 2004, 14, 505.
- (3) Holstein, W. L.; Rosenfeld, H. D. *J. Phys. Chem. B* 2005, 109, 2176.
- (4) Lu, Q.; Yang, B.; Zhuang, L.; Lu, J. *J. Phys. Chem. B* 2005, 109, 1715.
- (5) Jambunathan, K.; Jayaraman, S.; Hillier, A. C. *Langmuir* 2004, 20, 1856.
- (6) Park, K.-W.; Choi, J.-H.; Ahn, K.-S.; Sung, Y.-E. *J. Phys. Chem. B* 2004, 108, 5989.
- (7) Liu, Z.; Ling, X.; Su, X.; Lee, J. Y. *J. Phys. Chem. B* 2004, 108, 8234.

In,¹⁸ Sb,¹⁸ Mn,¹⁸ Ru, and W²³ or oxides RuO₂,^{24–27} WO₃,²⁸ CuO and NiO,²⁹ IrO₂,³⁰ and so on. Numerous attempts

- (8) Yajima, T.; Uchida, H.; Watanabe, M. *J. Phys. Chem. B* 2004, 108, 2654.
- (9) Moore, J. T.; Corn, J. D.; Chu, D.; Jiang, R.; Boxall, D. L.; Kenik, E. A.; Lukehart, C. M. *Chem. Mater.* 2003, 15, 3320.
- (10) Lizcano-Valbuena, W. H.; Azevedo, D. C.; Gonzalez, E. R. *Electrochim. Acta* 2004, 49, 1289.
- (11) Sirk, A. H. C.; Hill, J. M.; Kung, S. K. Y.; Birss, V. I. *J. Phys. Chem. B* 2004, 108, 689.
- (12) Koper, M. T. M.; Shubin, T. E.; Van Santen, R. A. *J. Phys. Chem. B* 2002, 106, 686.
- (13) Steigerwalt, E. S.; Deluga, G. A.; Lukehart, C. M. *J. Phys. Chem. B* 2002, 106, 760.
- (14) Viswanathan, R.; Hou, G.; Liu, R.; Bare, S. R.; Modica, F.; Mickelson, G.; Segre, C. U.; Leyarovska N.; Smotkin, E. S. *J. Phys. Chem. B* 2002, 106, 3458.
- (15) Fachini, E. R.; Diaz-Ayala, R.; Casado-Rivera, E.; File, S.; Cabrera, C. R. *Langmuir* 2003, 19, 8986.
- (16) Wu, G.; Li, L.; Xu, B. *Electrochim. Acta* 2004, 50, 1.
- (17) Gonzalez, M. J.; Peters, C. H.; Wrighton, M. S. *J. Phys. Chem. B* 2001, 105, 5470.
- (18) Casado-Rivera, E.; Volpe, D. J.; Alden, L.; Lind, C.; Downie, C.; Va'zquez-Alvarez, T.; Angelo, A. C. D.; DiSalvo, F. J.; Abruna, H. D. *J. Am. Chem. Soc.* 2004, 126, 4043.
- (19) Park, K.-W.; Choi, J.-H.; Sung, Y.-E. *J. Phys. Chem. B* 2003, 107, 5851.
- (20) Liu, F.; Lee, J. Y.; Zhou, W. *J. Phys. Chem. B* 2004, 108, 17959.
- (21) Moore, J. T.; Chu, D.; Jiang, R.; Deluga, G. A.; Lukehart, C. M. *Chem. Mater.* 2003, 15, 1119.
- (22) Huang, J.; Yang, H.; Huang, Q.; Tang, Y.; Lu, T.; Akinsb, D. L. *J. Electrochem. Soc.* 2004, 151, A1810.
- (23) Umeda, M.; Ojima, H.; Mohamedi, M.; Uchida, I. *J. Power Sources* 2004, 136, 10.
- (24) Villalba, H. M.; Mattos-Costa, F. I.; Bulhoes, L. O. S. *J. Phys. Chem. B* 2004, 108, 12898.
- (25) Liu, H.; Iglesia, E. *J. Phys. Chem. B* 2005, 109, 2155.
- (26) Yang, L. X.; Allen, R. G.; Scott, K.; Christensen, P. A.; Rey, S. *Electrochim. Acta* 2005, 50, 1217.
- (27) Suffredini, H. B.; Tricoli, V.; Avaca, L. A.; Vatistas, N. *Electrochim. Commun.* 2004, 6, 1025.
- (28) Park, K.-W.; Ahn, K.-S.; Nah, Y.-C.; Choi, J.-H.; Sung, Y.-E. *J. Phys. Chem. B* 2003, 107, 4352.

are underway to improve its performance, but binary PtRu/C is still considered as a CO-tolerant benchmark anode catalyst for use in DMFC.

PtRu is a promising catalyst for methanol oxidation in DMFC. It is well-known that the preparation technique is one of the key factors to determine its catalytic activity. Numerous approaches including impregnation and chemical reduction,^{4,7,10,31,32} electrodeposition,^{5,33,34} and the sputtering method⁶ have been developed in order to generate clusters on the nanoscale and with greater uniformity on the carbon supports. The PtRu nanoparticles can be prepared by chemical reduction with formic acid¹⁰ or the impregnation method,⁴ a microwave-assisted polyol process⁷ using metal precursors H₂PtCl₆ and RuCl₃. Chemical methods are the most widely used in the synthesis of metal or mixed-metal nanoparticles. However, conventional preparation techniques based on wet impregnation and chemical reduction of the metal precursors are often time consuming and labor intensive. In addition, these procedures often do not provide adequate control of particle shape and size. The physical methods mainly proceed in a vacuum through atomization of metals by thermal evaporation or sputtering. There is some difficulty for reactive components to penetrate into the pores of supports to achieve effective catalysis and to form high-performance electrodes in a fuel cell. In contrast, more commonly, a high surface support such as Vulcan 72 carbon is often used as a support for catalysts. It is still necessary to study the synthesis of nanoscale particles with high activity as electrocatalytic materials.

The use of supercritical fluids (SCF) for the synthesis and processing of nanomaterials has gained considerable interest in recent years.^{35–49} SCF exhibits an attractive combination of the solvent properties of a gas and a liquid. It can dissolve solutes such as a liquid and yet possess low viscosity, high diffusivity, and zero surface extension like a gas. Furthermore, the solvent strength of SCF can be varied by manipulating fluid temperature and pressure, thus allowing a degree of control and rapid separation of

products, which is impossible using conventional solvents. It provides a rapid, direct, and clean approach to preparing nanomaterials and nanocomposites. These special and unique features make SCF an attractive medium for delivering reactant molecules to areas with high aspect ratios, complicated surfaces, and poorly wettable substrates. Supercritical carbon dioxide (scCO₂) allows reactive components to penetrate inside the porous materials themselves, partitioning into the inner regions of the porous supports.⁴⁹ Through hydrogen reduction of metal- β -diketone complexes in scCO₂, multiwalled carbon nanotubes can be decorated by metal nanoparticles with uniformity to achieve nanocomposites.^{46–50} In previous papers, we have demonstrated high activity for oxygen reduction reactions of Pd/CNT³¹ and Pt/CNT³² processed in SCF. Recently, platinum⁵³ and ruthenium⁶⁴ nanoparticles were successfully loaded on carbon aerogel in scCO₂. In principle, a number of metal precursors can be used as starting materials in SCF and metal alloys can be coated on CNT to form nanocomposites. Cu–Pd alloy nanoparticles attached to SiC nanowires through hydrogen reduction of a mixture of Cu(hfa)₂·xH₂O and Pd(hfa)₂·xH₂O [hfa = hexafluoroacetylacetone] in scCO₂ have been obtained.⁵⁰ In this paper, platinum/ruthenium alloy nanoparticles were decorated on carbon nanotubes in scCO₂ and the nanocomposites were characterized by transmission electron microscopy (TEM) and X-ray diffraction (XRD). The PtRu/CNT powder was loaded on the glassy carbon electrode through a casting process, and the electrocatalytic activity for methanol oxidation was investigated in 1 M H₂SO₄ at room temperature using electrochemical methods such as cyclic voltammetry (CV), linear sweep voltammetry (LSV), chronoamperometry (CA), and electrochemical impedance spectroscopy (EIS). Its catalytic performance was compared with that of Pt/CNT synthesized in scCO₂.

2. Experimental Section

- (29) Gu, Z.; Hohn, K. L. *Ind. Eng. Chem. Res.* 2004, 43, 30.
- (30) Chen, A.; La Russa, D. J.; Miller, B. *Langmuir* 2004, 20, 9695.
- (31) Spinacé, E. V.; Neto, A. O.; Linardi, M. *J. Power Sources* 2004, 129, 121.
- (32) Che, G.; Lakshmi, B. B.; Martin, C. R.; Fisher, E. R. *Langmuir* 1999, 15, 750.
- (33) Mastragostino, M.; Missiroli, A.; Soavi, F. *J. Electrochem. Soc.* 2004, 151, A1919.
- (34) Missiroli, A.; Soavi, F.; Mastragostino, M. *Electrochim. Solid-State Lett.* 2005, 8, A110.
- (35) Johnston, K. P.; Shah, P. S. *Science* 2004, 303, 482.
- (36) Shah, P. S.; Hanrath, T.; Johnston, K. P.; Korgel, B. A. *J. Phys. Chem. B* 2004, 108, 9574.
- (37) Ye, X.; Wai, C. M.; Zhang, D. Q.; Kranov, Y.; Mellroy, D. N.; Lin, Y.; Engelhard, M. *Chem. Mater.* 2003, 15, 83.
- (38) Michel, P. *Curr. Opin. Solid State Mater. Sci.* 2003, 7, 319.
- (39) Cansell, F.; Aymonier, C.; Loppinet-Serani, A. *Curr. Opin. Solid State Mater. Sci.* 2003, 7, 331.
- (40) Knez, Z.; Weidner, E. *Curr. Opin. Solid State Mater. Sci.* 2003, 7, 353.
- (41) Shariati, A.; Peters, C. J. *Curr. Opin. Solid State Mater. Sci.* 2003, 7, 371.
- (42) Tomasko, D. L.; Han, X. M.; Liu, D. H.; Gao, W. H. *Curr. Opin. Solid State Mater. Sci.* 2003, 7, 407.
- (43) Breckman, E. J. *J. Supercrit. Fluids* 2004, 28, 121.
- (44) Hakuta, Y.; Hayashi, A.; Arai, K. *Curr. Opin. Solid State Mater. Sci.* 2003, 7, 341.
- (45) Ye, X.; Lin, Y.; Wang, C. M.; Engelhard, M. H.; Wang, Y.; Wai, C. M. *J. Mater. Chem.* 2004, 14, 908.
- (46) Ye, X.; Lin, Y.; Wang, C. M.; Wai, C. M. *Adv. Mater.* 2003, 15, 316.
- (47) Ye, X.; Zhang, H.; Lin, Y.; Wang, L. S.; Wai, C. M. *J. Nanosci. Nanotech.* 2004, 4, 82.
- (48) Ye, X.; Lin, Y.; Wai, C. M. *Chem. Commun.* 2003, 642.
- (49) Morley, K. S.; Mart, P. C.; Webb, P. B.; Berry, A. R.; Allison, F. J.; Moldovan, G.; Brown, P. D.; Howdle, S. M. *J. Mater. Chem.* 2002, 12, 1898.

2.1. Reagents. Multiwalled carbon nanotubes (>95% purity, diameter 20–50 nm, length 1–5 μ m) were purchased from NanoLab, Inc. (Newton, MA). Nafion (perfluorinated ion-exchange resin, 5 wt% solution) was obtained from Aldrich. Sulfuric acid was purchased from Fisher Chemicals, and ultrapure water (~18.3 M Ω cm) was used to prepare the solutions. A platinum precursor (Pt(acac)₂ [acac = acetylacetone]) and a ruthenium precursor (Ru(acac)₂) were purchased from Aldrich and used as received. High-purity hydrogen, carbon dioxide, and nitrogen gas were used in the experiments.

2.2. Decorating PtRu Nanoparticles on Carbon Nanotubes. The CNT were treated as described in previous reports.⁴⁶ The PtRu/CNT catalyst was synthesized by using the following procedures: The CNT (20 mg) and the metal precursors Pt(acac)₂ (20 mg) and Ru(acac)₂ (20 mg) with a small amount of methanol (2 mL) as a modifier were all loaded in a high-pressure reaction cell (10 mL) located in a oven at 200 °C. Pt(acac)₂ and Ru(acac)₂ have a low solubility in scCO₂. Addition of methanol modifies the polarity of CO₂ and enables dissolution of the Pt and Ru precursors in the fluid phase. Carbon dioxide gas was introduced into the reaction cell and was pressurized to 80 bar in order to make the gas become a supercritical fluid. Hydrogen gas at 10 bar was initially filled in the H₂ + CO₂ mixer cell, and CO₂ gas of 120 bar

- (50) Lin, Y.; Ye, X.; Wai, C. M. Nanostructured Materials Synthesized In Supercritical Fluid. In *Dekker Encyclopedia of Nanoscience and Nanotechnology*; Schwarz, J. A., Contescu, C., Putye, K., Ed.; Marcel Dekker: New York, 2004; pp 2595–2607.
- (51) Lin, Y.; Cui, X.; Ye, X. *Electrochim. Commun.* 2005, 7, 267.
- (52) Lin, Y.; Cui, X.; Yen, C.; Wai, C. M. *J. Phys. Chem. B* 2005, 109, 14110.
- (53) Saquing, C. D.; Cheng, T.; Aindow, M.; Erkey, C. *J. Phys. Chem. B* 2004, 108, 7716.
- (54) Zhang, Y.; Kang, D.; Aindow, M.; Erkey, C. *J. Phys. Chem. B* 2005, 109, 2617.

was then added to the cell. After 1 h of waiting for the precursors to completely dissolve in the scCO₂, the H₂ + CO₂ gas was introduced into the reaction cell by pressurizing it to 160 bar. The reductions (Pt²⁺ to Pt⁰ and Ru²⁺ to Ru⁰) were fast and took only 15 min. After the reaction cell was depressurized, PtRu/CNT powder could be recovered and then was washed 5 times using methanol and ultrasonication for 30 min each time. The phase behavior of the CO₂ and methanol mixture at 160 bar and 200 °C was observed in a high-pressure view-cell. Complete dissolution of the metal precursors and methanol in scCO₂ (one phase) was observed. The detailed procedures for the preparation of Pt/CNT were described in our previous report.⁵²

2.3. Electrode Preparation and Modification. A 0.5 wt% Nafion solution was prepared by diluting the 5 wt% Nafion solution with water. Catalyst powder was dispersed ultrasonically in 0.5% Nafion solution to obtain a homogeneous black suspension solution with 1 mg/mL PtRu/CNT or Pt/CNT, and a 5 μL aliquot of this solution was pipetted onto glassy carbon (GC, 3 mm in diameter, BAS, West Lafayette, IN) electrode surface. Before the surface modification, the GC electrode was polished with 0.3 and 0.05 μm alumina slurries, washed with water and acetone, and finally subjected to ultrasonic agitation for 1 min in ultrapure water and dried under an air stream. The coating was dried at room temperature in the air for 1 h. The catalyst should be homogeneously dispersed, and the same procedures for experiments should be controlled in order to obtain reproducible results. The modified electrode surface was then washed carefully with ultrapure water before measurement.

2.4 Apparatus. TEM images of the decorated CNT were taken using a JEOL JEM 2010 microscope equipped with an Oxford ISIS system. The operating voltage on the microscope was 200 keV. All images were digitally recorded with a slow-scan CCD camera (image size 1024 × 1024 pixels), and image processing was carried out using a Digital Micrograph (Gatan). To obtain TEM images, the as-synthesized platinum–ruthenium-modified CNT powder was dispersed in ethanol solution by ultrasonication for 1 min and then deposited on a Cu–carbon grid. Powder XRD patterns of the samples were recorded on Siemens D5000 diffractometer using Cu Kα radiation. The Pt/Ru ratios were obtained by energy-diffusive X-ray (EDS) analysis.

CV, LSV, and CA experiments were performed with a CHI 660 electrochemical workstation (CH Instruments, Inc, Austin, Texas). EIS was performed with a Solartron 1287 potentiostat, a Solartron 1260 frequency response analyzer, and the software Z-Plot. The amplitude of modulation potential for the EIS measurements was 10 mV, and the frequency was varied from 100 kHz to 0.02 Hz in a solution of 2 M CH₃OH and 1 M H₂SO₄. All electrochemical experiments were carried out with a conventional three-electrode system. The working electrode was glassy carbon coated with Pt/CNT or PtRu/CNT composite films. An Ag/AgCl (saturated by KCl solution) reference electrode was used for all electrochemical measurements, and all the potentials were reported versus this reference electrode. A platinum wire was used as a counter electrode. To obtain reproducible and reliable results, a fresh methanol solution was used for every measurement. All the electrochemical experiments were carried out at room temperature.

3. Results and Discussion

3.1. TEM and XRD Characterization of PtRu/CNT.

Figure 1A shows the typical TEM micrograph of PtRu/CNT electrocatalysts prepared in scCO₂. The nanoparticles show a good distribution on the surface of CNT, and the particles have an average size of 5–10 nm. It is well known that energy-diffusive X-ray spectrum (EDS) analysis can quantify the elements it detects. A quantitative analysis can be performed by a standard or a standardless analysis. A standardless analysis quantifies the elements by calculating the area under the peak of each identified element and, after taking account for the accelerating voltage of the beam to produce the spectrum, performs calculations to create sensitivity factors that will convert the area under the peak into weight or atomic percent. The EDS (Figure 1B) indicates the Pt and Ru content in

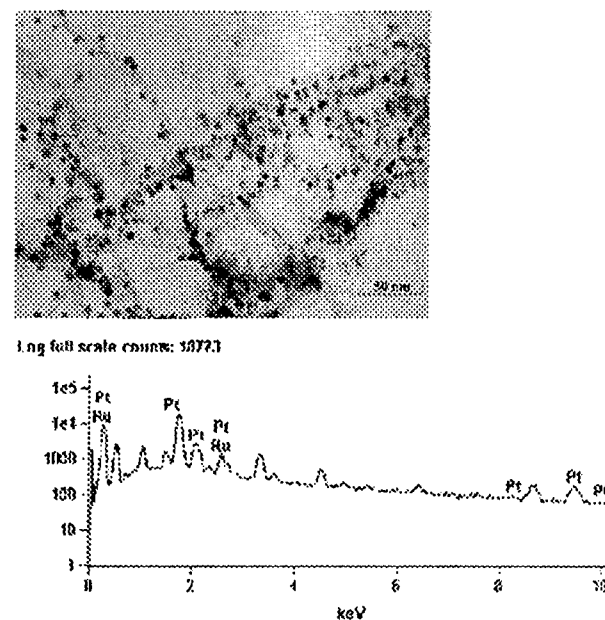


Figure 1. (A) Typical TEM image of CNT decorated by platinum/ruthenium nanoparticles synthesized in scCO₂. The scale bar is 50 nm. (B) EDS spectra of PtRu/CNT nanocomposite.

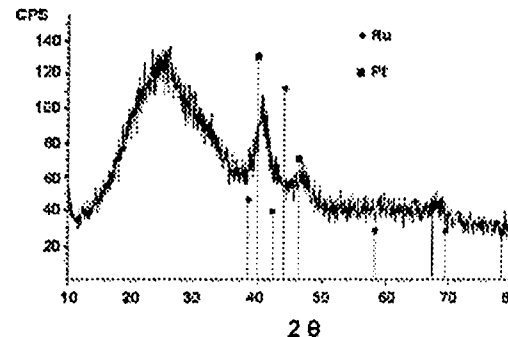


Figure 2. X-ray diffractogram of PtRu/CNT electrocatalysts synthesized in scCO₂.

the nanocomposite is 4.1% and 2.3 wt% and the molar ratio is approximately Pt/Ru = 45:55, respectively.

The as-prepared electrocatalyst was also characterized by powder XRD, as shown in Figure 2. XRD is a bulk analysis that reveals the crystal structure, lattice constants, and crystal orientation of the supported catalysts. According to previous reports, pure Pt has a face-centered cubic (fcc) crystal structure.⁵⁵ With the addition of Ru, which has a hexagonal closed-packed (hcp) crystal structure, the diffraction peaks of the PtRu will start to broaden and shift to higher 2θ values.⁷ Our result, as shown in Figure 2, is very consistent with those literature reports for PtRu. It has been reported that only the Pt fcc peaks appeared in XRD spectra for PtRu alloys containing up to 52 wt% Ru.^{56,57} The broad peak at 2θ = 25° is associated with the graphite-like structure of the CNT support.^{58,59} The peaks at 2θ ≈ 40° and 47° may be associated with the (111) and (200) planes, respectively, of the fcc structure

(55) Solla-Gullon, J.; Vidal-Iglesias, F. J.; Montiel, V.; Aldaz, A. *Electrochim. Acta*, 2004, 49, 5079.
 (56) Chu, D.; Gilman, S. J. *Electrochim. Soc.* 1996, 143, 1685.
 (57) Deivaraj, T. C.; Lee, J. Y. *J. Power Sources* 2005, 142, 43.
 (58) Wu, T.; Lin, Y.; Liao, C. *Carbon* 2005, 43, 734.
 (59) Li, W.; Liang, C.; Zhou, W.; Qiu, J.; Zhou, Z.; Sun, G.; Xin, Q. *J. Phys. Chem. B* 2003, 107, 6292.

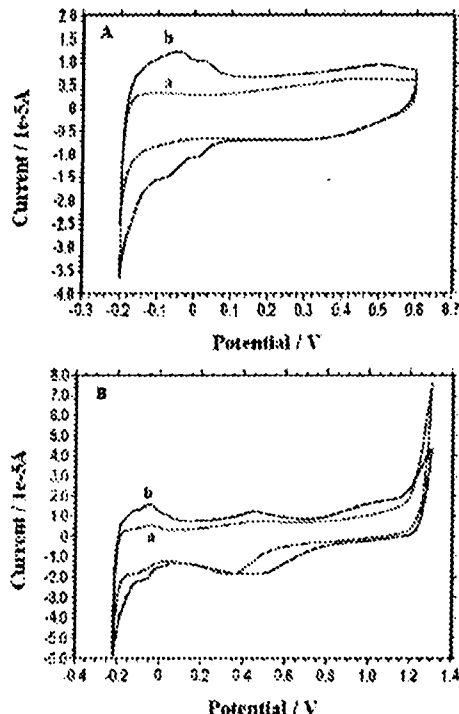


Figure 3. Cyclic voltammograms in 0.5 M H_2SO_4 solution saturated by N_2 for Pt/CNT (a) and PtRu/CNT (b) electrode in different scan range at 20 mV/s.

of platinum and characteristic of PtRu alloys. The broadened peaks in the XRD pattern are another characteristic of the nanometer scale which is consistent with the results of TEM. All the results validate the effectiveness of the experimental protocols in producing nanosized bimetallic nanoparticles on the surface of the CNT.

3.2. Electrochemical Performance of PtRu/CNT. Cyclic voltammograms scanning at different ranges for PtRu/CNT (a) and Pt/CNT (b) electrodes in a solution of 0.5 M H_2SO_4 saturated by nitrogen are presented in Figure 3. The potential sweep rate was 20 mV/s. It is reasonable that different features appeared for these two electrodes. Comparing with Pt/CNT electrode, the well-defined hydrogen adsorption-desorption peaks disappeared, as seen in short-range CV curves because of the presence of ruthenium (Figure 3A). At the same time, the reduction peak shifts negatively due to the slow kinetics of reduction Ru oxides which can be observed during the negatively going potential sweep (Figure 3B). This feature of this curve is consistent with those of the CV curves for the PtRu electrode.^{6,60}

3.3. Electrocatalytic Activity for Methanol Oxidation Reaction. The electrocatalytic activity for methanol oxidation of PtRu/CNT prepared in scCO₂ was characterized by CV in an electrolyte of 1 M H_2SO_4 and 2 M CH_3OH at 50 mV/s, and the resulting voltammograms are shown in Figure 4. Figure 4 shows the results of Pt/CNT (A) and PtRu/CNT (B, C) electrodes for the electrooxidation of methanol. Before recording cyclic voltammograms, the electrode was soaked in the test solution for 10 min to allow the system reaching a stable state. The potential scan starts from its open circuit potential positively to 1.0 V then to ~ 0.1 V and then it cycles between ~ 0.1 and 1.0 V for PtRu/CNT electrode. The cyclic voltammograms of PtRu/CNT are different from those obtained on a Pt/CNT

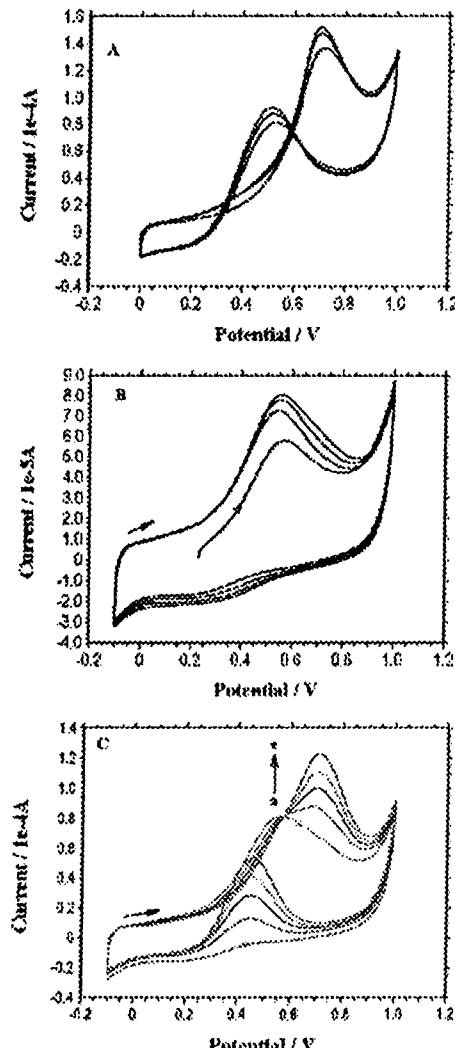


Figure 4. Cyclic voltammograms of room-temperature methanol oxidation on Pt/CNT (A), cycles 1–3 and PtRu/CNT (B, C), electrodes cycle 1–4 (B), and cycles 5, 10, 15, 20, 25 from a to e (C), respectively, at 50 mV/s in 1 M H_2SO_4 , 2 M CH_3OH .

electrode. The onset of methanol oxidation occurs at about 0.05 V at the electrode of PtRu/CNT. The lower onset potential indicates clear evidence for superior electrocatalytic activity for methanol oxidation. There are large changes in the potential cycles over time. The early cycles exhibit a low peak current and lower peak potential in the forward scan, and there is almost no peak during the reverse potential scan. As the number of cycles increases, the potential for the peak current in the forward scan shifts to higher values and the peak potential increases greatly. The forward anodic peak potential shifts more positively from cycle to cycle. By the sixth cycle, the forward peak potential is located at about 0.57 V and a broadened peak centered at 0.45 V appeared in the reverse scan. Then, anodic peaks appeared in both the forward and backward scans. Significant changes can be observed between the cycles 6 and 25, as shown in Figure 4C. The peak potential in the reverse scan moves to higher voltages, and the peak current increases. This phenomenon may result from the leaching of ruthenium during the cycling of the electrode between oxidizing and reducing potentials. At last, the cyclic voltammogram of the catalyst was found to have become similar to that of pure Pt/CNT, indicating excessive loss of Ru. Previous results have been shown

Table 1. Onset Potential, Peak Potential, and I_f/I_b Ratios of Different Catalysts

catalysts	onset potential	forward peak potential	I_f/I_b ratios	ref
Pt/CNT	0.25	0.69 ^a	1.42 ^a	this work
PtRu/CNT	0.05	0.57 ^b	5.33 ^b	this work
Pt/C	0.31 ^c	0.69 ^c	0.87	7
Pt ₆₂ Ru ₃₈ /C	0.02 ^c	0.62 ^c	2.30	7

^a Data were obtained on the basis of the second cycle of cyclic voltammograms at 50 mV/s. Potentials are versus Ag/AgCl. ^b Data were obtained on the basis of the sixth cycle of cyclic voltammograms at 50 mV/s. ^c These potentials are versus a saturated calomel electrode (SCE).

that similar performance was observed on a commercial E-TEK catalyst PtRu/C on carbon paper, as reported in a recent paper.³ The loss of ruthenium was confirmed by TEM and X-ray microanalysis in the commercial catalyst.³ More-detailed experiments are necessary to give a suitable and reasonable explanation.

Methanol oxidation on PtRu/CNT and Pt/CNT was compared in the following aspects to indicate their catalytic performance: onset potential of methanol, anodic peak potential, and ratio of the forward anodic peak current to the reverse anodic peak current. All related data and a comparison with the data from references are listed in Table 1.

The ratio of the forward anodic peak current (I_f) to the reverse anodic peak current (I_b) can be used to describe the catalyst tolerance to accumulation of carbonaceous species. High I_f/I_b value implies relatively complete oxidation of methanol to carbon dioxide. As shown in Table 1, the ratio was estimated to be 1.42 for the Pt/CNT electrode from the second cycle at 50 mV/s. The ratio for PtRu/CNT was obtained from the sixth cycle to be 5.33 which is much larger than Pt₆₂Ru₃₈ prepared by other method. Such a high value indicates that most of the intermediate carbonaceous species were oxidized to carbon dioxide in the forward scan on the PtRu/CNT electrode. These experimental results highlight the high activity for methanol oxidation on PtRu/CNT prepared from scCO₂. The high activity may result from the high surface area of CNT and the nanostructure of platinum/ruthenium.

It should be noted that such a comparison is not very precise because the catalytic activity is related to many factors such as surface area, particle size, preparation technique, pretreatment and homogeneity of alloys, etc. Despite this, it has been conclusively shown that the use of CNT and the catalysts processed in scCO₂ increase the anode activity and greatly reduce the effect of CO poisoning which can be confirmed from the larger I_f/I_b ratios. At the same time, the onset potential and peak potential of PtRu/CNT occur at significantly lower values compared to that of pure Pt/CNT, indicating the high activity of PtRu/CNT.

Linear sweep voltammograms were recorded for both PtRu/CNT (a) and Pt/CNT (b) electrodes in 1 M H₂SO₄ containing 2 M CH₃OH at 10 mV/s, as shown in Figure 5. As expected at the PtRu/CNT electrode, higher current is observed compared to a Pt/CNT electrode.

Chronoamperometric curves were measured at 0.4 V for PtRu/CNT (a) and Pt/CNT (b) electrodes, as shown in Figure 6. For this experiment, a potential step from the open circuit potential to 0.8 V was used. After 2 s, the potential was stepped to 0.3 V for 2 s, then stepped to 0.4 V, and the current-time curve was recorded for 3600 s. As shown, the methanol oxidation current at PtRu/CNT electrode is higher than that at Pt/CNT electrodes, though both electrodes present current decay in current-time measurement.

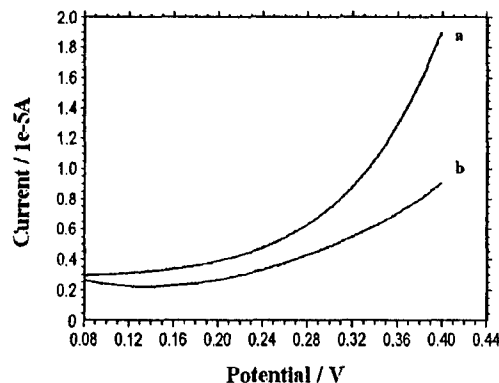


Figure 5. A comparison of methanol oxidation activity based on linear sweep voltammograms at PtRu/CNT (a) and Pt/CNT (b) at 10 mV/s.

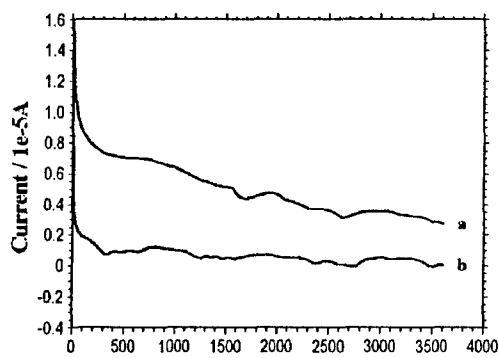


Figure 6. Current-time curves at 0.4 V for PtRu/CNT (a) and Pt/CNT (b) electrode in 1 M H₂SO₄, 2 M CH₃OH.

All the CV, LSV, and CA experimental results above show that the PtRu/CNT electrode has a higher activity for methanol oxidation than that at Pt/CNT electrodes. These results are consistent with the results of PtRu catalysts prepared by other methods. The higher activity can be explained by the bifunctional mechanism proposed by Watanabe and Motoo.⁶¹ It was assumed that Ru promotes the oxidation of the strongly bound CO_{ad} on Pt by supplying an oxygen source (Ru—OH_{ad}).

3.4. EIS Studies for PtRu/CNT and Pt/CNT Electrodes. EIS is a powerful tool which can provide a wealth of information for electrode reactions. It has been applied to the studies of fuel cell electrodes in recent reports.^{16,30,62,63} Here, we employed EIS to further investigate the activity of these two electrodes toward methanol electrooxidation. Figure 7 presents the Nyquist plots for Pt/CNT (□) and PtRu/CNT (○) electrodes measured in 2 M CH₃OH + 1 M H₂SO₄ solutions at 0.4 V. Semicircles with different diameters appeared in the tested frequency range for both electrodes. The resistance and capacitance of the coating can be obtained from the analysis of EIS spectra by using the software of Z-view based on an equivalent electric circuit, as shown in Figure 8 as suggested in the literature.^{30,63} In this $R_s(R_{ct}CPE)$ circuit, R_s represents the uncompensated solution resistance, similar results were obtained for these two electrodes. R_{ct} represents the charge-transfer resistance while the meaning of constant phase element (CPE) is depending on the parameter of CPE-P. If CPE-P is near 1, then the CPE

(61) Watanabe, M.; Motoo, S. *J. Electroanal. Chem.* 1975, 60, 267.

(62) Easton, E. B.; Pickup, P. G. *Electrochim. Acta* 2005, 50, 2469.

(63) Peng, X.; Koneczk, K.; Nigro, S.; Chen, A. *Chem. Commun.* 2004, 2872.

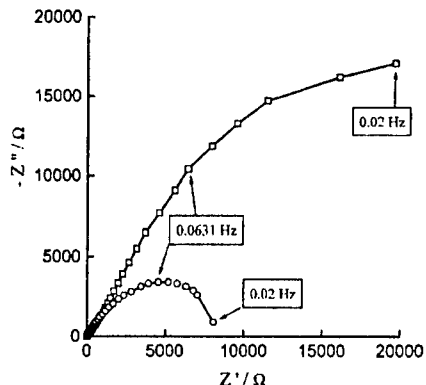


Figure 7. Complex plane plots of electrochemical impedance spectroscopy of PtRu/CNT (○) and Pt/CNT (□) electrodes at 0.4 V in 1 M H_2SO_4 , 2 M CH_3OH .

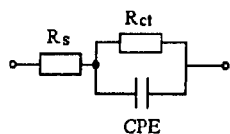


Figure 8. Equivalent circuit used to fit the impedance spectra presented in Figure 7.

Table 2. Impedance Components for Pt/CNT (□) and PtRu/CNT (○) Electrodes by Fitting the Experimental Data using Z-view Software Based on the Equivalent Circuit, as shown in Figure 8

electrode	R_{ct}/Ω		CPE-T/ μF		CPE-P	
	value	error %	value	error %	value	error %
Pt/CNT	1.30×10^5	16.08	148.2	1.2	0.66	0.34
PtRu/CNT	1.02×10^4	3.03	198.1	1.6	0.73	0.46

can be considered as a capacitor. The parallel combination of the charge-transfer resistance and CPE take into account the thin film and the methanol adsorption and oxidation. The parallel combination (R_{ct} CPE) leads to a depressed semicircle in the corresponding Nyquist impedance plot. The values for all the parameters R_{ct} , CPE-T, CPE-P, and their associated % error determined by the fitting of the experimental EIS data are summarized in Table 2. As seen in Table 2, the charge-transfer resistance is one order lower for the electrode of PtRu/CNT than

that of Pt/CNT, which reflects the higher electrocatalytic activity for PtRu/CNT. The value of CPE-P is around 0.7 for these two electrodes. There would be deviations if it is considered as a capacitor, which reflects the complication of solid/liquid interface.^{16,62} More detailed study is necessary to illustrate the process of methanol electrooxidation on the electrode of PtRu/CNT.

4. Conclusions

In summary, we have successfully deposited platinum/ruthenium nanoparticles on CNT surfaces in scCO_2 . A better electrocatalytic performance of bimetallic alloy PtRu on the surface of CNT from scCO_2 is observed for the methanol oxidation which demonstrated by electrochemical studies including CV, LSV, CA, and EIS. The higher I_f/I_b value and lower onset potential for methanol oxidation show that the PtRu/CNT exhibit higher activity than that of the Pt/CNT, which can be explained from the bifunctional mechanism described previously. The high catalytic activity has been attributed to the large surface area of CNT and the decrease of the overpotential for methanol oxidation. The results presented in this paper demonstrate that the scCO_2 deposition method developed in this work is highly efficient in preparing bimetallic electrocatalysts based on CNT and suggested the use of the electrocatalysts as promising candidates for the development of better fuel cells.

Acknowledgment. This work is supported by a laboratory directed research and development program at Pacific Northwest National Laboratory (PNNL) and grants from the Electric Power Research Institute (E2-P261/C8273) and AFOSR (F49620-03-1-0361). The research described in this paper was performed partially at the Environmental Molecular Sciences Laboratory (EMSL), a national scientific user facility sponsored by the U.S. Department of Energy's Office of Biological and Environmental Research and located at PNNL. PNNL is operated by Battelle for the U.S. Department of Energy under Contract No. DE-AC05-76RL01830. The authors would like to thank the reviewers for their valuable comments which improve the quality of the manuscript greatly.

LA051272O

Microemulsion-Templated Synthesis of Carbon Nanotube-Supported Pd and Rh Nanoparticles for Catalytic Applications

Byunghoon Yoon and Chien M. Wai*

Department of Chemistry, University of Idaho, Moscow, Idaho 83844

Received August 23, 2005; E-mail: cwai@uidaho.edu

Palladium nanoparticles stabilized and dispersed by water-in-oil microemulsions are very active catalysts for hydrogenation of olefins in organic solvents.¹ However, recycling nanoparticle catalysts stabilized in water-in-oil microemulsions is experimentally difficult. Carbon nanotubes (CNTs), due to their unusual properties, are promising carbonaceous materials for supporting catalytic nanoparticles.² Because of their small sizes, CNT-supported catalytic nanoparticles can be uniformly dispersed in organic solvents by stirring. Recycling CNT-supported catalytic nanoparticles can be accomplished by gravitational sedimentation. Known methods for depositing catalytic nanoparticles on CNTs including supercritical fluid, solid-state, or aqueous reactions usually require high temperatures or pressures.³ Water-in-oil microemulsions have been used as templates for synthesizing nanoparticles. Ingelsten et al. reported a method of depositing Pt nanoparticles synthesized in a water-in-oil microemulsion on alumina.⁴ The microemulsion was destabilized by adding tetrahydrofuran to release the metal nanoparticles for deposition. The process was slow, and agglomeration of the Pt nanoparticles occurred during the deposition. Hanaoka et al. also used a water-in-oil microemulsion to synthesize Rh nanoparticles by hydrogen reduction and followed this step by depositing them on silica.⁵ There is no report in the literature regarding microemulsion-templated deposition of metal nanoparticles on CNT surfaces. The feasibility of using a water-in-oil microemulsion for synthesizing Pd and Rh nanoparticles followed by their direct deposition on CNT surfaces was investigated recently in our laboratory. This simple approach turns out to be very effective for making CNT-supported catalytic metal nanoparticles that are uniformly anchored on CNT surfaces with a narrow size distribution. The synthetic process can be carried out at room temperature and requires only water-soluble metal salts as starting materials. Hydrogen gas can be used as a reducing agent to convert Pd^{2+} and Rh^{3+} ions to their elemental states leading to nanoparticles formation within the microemulsion.¹ Deposition of metal nanoparticles on CNT surfaces is achieved by stirring CNTs in the microemulsion solution. This method of making CNT-supported nanoparticles, including monometallic, bimetallic, or even multimetallic ones, provides a simple way of studying a variety of nanoscale metal catalysts of different compositions.

The functionalized multiwalled carbon nanotubes (fMWCNTs) were prepared by a method known in the literature.⁶ Formation of metal nanoparticles in a water-in-hexane microemulsion using sodium bis(2-hexylethyl)sulfosuccinate (AOT) as the surfactant and hydrogen gas as the reducing agent was described in a previous article.¹ The fMWCNTs were added to the water-in-hexane microemulsion solution, and the metal nanoparticles formed in the microemulsion could be transferred to the CNT surfaces in 30 min of stirring. Transmission electron microscope (TEM) images of the Pd, Rh, and Pd/Rh nanoparticles deposited on the surfaces of the fMWCNTs are shown in panels a, b, and c of Figure 1, respectively.

The Pd and Rh nanoparticles deposited on the fMWCNTs have size distributions in the range of about 2–10 nm and are dispersed

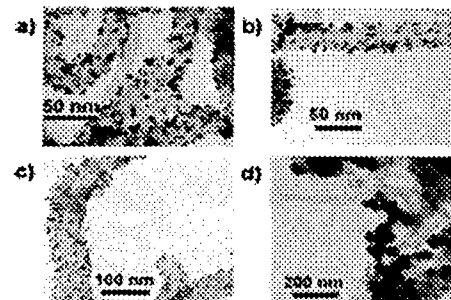


Figure 1. TEM images of the microemulsion-templated synthesis of CNT-supported metal nanoparticles: (a) Pd/CNTs, (b) Rh/CNTs, (c) Pd/Rh bimetallic nanoparticles from the microemulsion methods, and (d) Pd/CNTs from an aqueous Na_2PdCl_4 solution.

on the substrate surfaces. Without the microemulsion, direct deposition of Pd or Rh on the fMWCNTs by hydrogen reduction of an aqueous Na_2PdCl_4 or $RhCl_3$ solution, respectively, resulted in metal particles about 1 order of magnitude larger and clumped together as shown in Figure 1d. This result was also observed when a palladium(II) hexafluoroacetylacetone [Pd(hfa)₂] was reduced in hexane with hydrogen in the presence of the fMWCNTs. The TEM images demonstrate that the microemulsions are responsible for making metal nanoparticles on the surfaces of the fMWCNTs. The nanoparticles also could not be induced by the TEM beam because virtually no Rh nanoparticles were observed after exposing Rh^{3+} soaked fMWCNTs in our TEM.⁷

In X-ray photoelectron spectroscopy (XPS) analyses of the CNT-supported metal nanoparticles, 12.69 wt % of Pd and 17.33 wt % of Rh were found in the Pd/CNT and in the Rh/CNT catalyst, respectively. On the basis of the amounts of the metal salts used in the preparation of the microemulsion, we estimated that about 43% of palladium from Na_2PdCl_4 and 58% of rhodium from $RhCl_3$ were deposited as metallic nanoparticles on the surfaces of the fMWCNTs in the synthetic process. Repeated washing with methanol 5 times to remove the AOT from the CNT-supported metal nanoparticles was required to purify the nanoparticles. After the washing, no sulfur peak was detected in the CNT-supported nanoparticle samples by energy-dispersive X-ray spectroscopy (EDX) and XPS. The asymmetric and symmetric stretching of the SO_2 group of the AOT was also not detected in the CNT samples by FT-IR. After 10 repeated uses of the catalyst for hydrogenation of *trans*-stilbene as in eq 1, TEM images showed little change in the distribution and size of the Pd nanoparticles deposited on the CNT surfaces and the catalyst did not show detectable loss of activity. An X-ray diffraction (XRD) pattern of the CNT-supported Pd catalyst (given in the Supporting Information) revealed the $Pd(111)$ peak at $2\theta = 40.20 \pm 0.05^\circ$, and the Rh/CNT catalyst showed the $Rh(111)$ peak at $2\theta = 41.15 \pm 0.05^\circ$, consistent with the metallic Pd and Rh data in the literature.

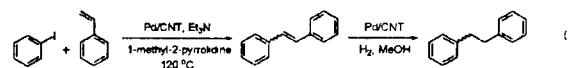
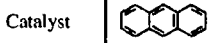
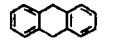
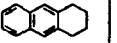
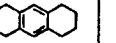


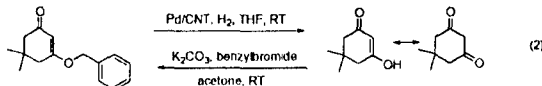
Table 1. Catalytic Hydrogenation of Anthracene Using CNT-Supported Nanocatalysts

Catalyst				
Rh/C ^a	>99 %	ND	ND	ND
Rh/CNT ^b	23.8 %	4.1 %	62.4 %	9.7 %
Pd/CNT ^b	19.1 %	80.9 %	ND	ND
Pd-Rh/CNT ^c	ND	7.3 %	ND	92.7 %

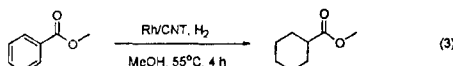
^a 0.0300 g of 5 wt % Rh. ^b 0.0100 g of the CNT-supported metal nanoparticles. ^c 6.3 wt % Pd and 6.9 wt % Rh. All catalysts were used after drying in the oven for 1 h at 100 °C, and stirring speed was optimized at 600 rpm. Anthracene (0.0178 g, 0.1 mmol) with the nanocatalyst was stirred for 30 min under 10 atm of H₂ pressure in methanol at 25 °C. The conversion yield was determined by NMR and HPLC (C₁₈ column, MeOH/H₂O = 4:1). ND = not detectable.

To test activities of the CNT-supported Pd nanoparticles, iodobenzene and styrene were selected for the Heck coupling reaction. The coupling product was obtained with 94% of the isolated yield after 3 h of the reaction shown in eq 1. A conventional palladium/carbon catalyst (10 wt % Pd from Aldrich) was also used for this coupling reaction under the same conditions, and the Heck coupling product (*trans*-stilbene) with 53% conversion yield was detected after 24 h. The particle size of the commercial Pd catalyst showed a very large variation, typically about 2 orders of magnitude larger than the CNT-supported nanoparticles. It was reported that the pore size, acid–base properties, and impurities of the conventional carbon supports could influence the metal particle distributions.⁸ The conversion of *trans*-stilbene to 1,2-diphenylethane was about 99% after 10 min of reaction using 1 atm of H₂ gas at 25 °C. Using the commercial Pd/C catalyst, it would require 1 h to achieve the same degree of hydrogenation of *trans*-stilbene under the same conditions. The high catalytic activity of the CNT-supported Pd nanoparticles in forming a new carbon–carbon bond via the Heck coupling is potentially significant for organic synthesis applications.

The debenzylation of the protected group is conventionally carried out with Pd as a catalyst. To test the effectiveness of the Pd/CNT catalyst, we synthesized O-alkylated 5,5-dimethyl-1,3-cyclohexanedione derivatives as shown in eq 2.⁹ After 3 h using the Pd/CNT catalyst, the debenzylation products were obtained with 95% of yield (eq 2). In case of the commercial Pd/C catalyst, less than 10% of the starting materials were converted to the debenzylated products after 9 h of reaction under the same conditions. The CNT-supported Pd nanoparticles are obviously much more active than the commercial Pd/C catalyst for the debenzylation process.



In another case, methyl benzoate in methanol was essentially all converted (>99%) to methyl cyclohexanecarboxylate after 4 h of reaction with the Rh/CNT nanoparticles under the conditions specified in eq 3.



A comparison of the catalytic activity between a commercial Rh/C (5 wt % of Rh from Strem Chemicals) catalyst and the Rh/CNT nanoparticles was made for hydrogenation of anthracene (Table 1). No conversion of anthracene was detected with the commercial Rh/C catalyst after 2 h of reaction at 25 °C with 10 atm of H₂. For the CNT-supported Rh nanoparticles, none of the

starting material anthracene was detected by TLC, NMR, and HPLC after 1 h of reaction under the same conditions.

An interesting observation is that when a mixture of Pd²⁺ and Rh³⁺ ions was used as the starting material in the water core of the microemulsion for the synthesis, the resulting Pd/Rh nanoparticles deposited on the fMWCNTs (Figure 1c) are more active than the single metal nanoparticles prepared in the same way for catalytic hydrogenation of anthracene. Using CNT-supported Pd or Rh monometallic nanoparticles, the conversion yield of anthracene to 1,2,3,4,5,6,7,8-octahydroanthracene was less than 10%. The corresponding product was obtained at 92.7% with CNT-supported Pd/Rh nanoparticles under the same conditions (Table 1). The CNT-supported Pd/Rh catalyst was found to contain 6.3 ± 0.1 wt % Pd and 6.9 ± 0.4 wt % Rh in EDX and XPS analyses. The XRD data showed a single peak for the Pd/Rh nanoparticles deposited on the fMWCNTs with a 2θ value between that of the Pd (2θ = 40.20°) and Rh (2θ = 41.15°) metal nanoparticles. XPS spectra of the Pd/Rh catalyst revealed the presence of Pd(3d_{5/2}) and Pd(3d_{3/2}) peaks at 335.4 and 340.7 eV, respectively, and Rh(3d_{5/2}) and Rh(3d_{3/2}) peaks at 307.2 and 311.9 eV, respectively.

According to a recent report, bimetallic nanoparticles may have a number of different morphologies that would not show changes in XPS spectra.¹⁰ The enhanced catalytic activity of the CNT-supported Pd/Rh bimetallic system could be due to certain arrangements of the Pd and Rh nanoclusters on the nanoparticles' surfaces. The Pd/Rh nanoparticles synthesized by the microemulsion method described in this communication are probably bimetallic in nature with an unknown morphology.

In conclusion, the fMWCNT-supported Pd, Rh, and Rh/Pd nanoparticle catalysts can be prepared easily with high yields using water-in-oil microemulsions containing metal ions as starting materials. Metal nanoparticles are formed by hydrogen reduction of metal ions in the water core with 1 atm H₂ gas at 25 °C. The CNT-supported Rh nanoparticles are active catalysts for hydrogenation of arenes, and the CNT-supported bimetallic Pd/Rh nanoparticles show an unusually high catalytic activity for hydrogenation of anthracene. This simple and novel synthetic technique for making CNT-supported monometallic and bimetallic nanoparticles may have a wide range of catalytic applications for chemical syntheses.

Acknowledgment. This work was supported by a grant from DOD-AFOSR (F49620-03-1-0361).

Supporting Information Available: Experimental details and XRD data. This material is available free of charge via the Internet at <http://pubs.acs.org>.

References

- (1) Yoon, B.; Kim, H.; Wai, C. M. *Chem. Commun.* 2003, 1040–1041.
- (2) Sun, J.; Gao, L.; Iwasa, M. *Chem. Commun.* 2004, 832–833.
- (3) (a) Ye, X.-R.; Lin, Y.; Wang, C.; Engelhard, M. H.; Wang, Y.; Wai, C. M. *J. Mater. Chem.* 2004, 14, 908–913. (b) Xue, B.; Chen, P.; Hong, Q.; Lin, J.; Tan, K. L. *J. Mater. Chem.* 2001, 11, 2378–2381. (c) Wang, Y.; Shah, N.; Huffman, G. P. *Energy Fuels* 2004, 18, 1429–1433.
- (4) Ingelström, P.; Beziat, J. C.; Bergkvist, K.; Palmqvist, A.; Skoglundh, M.; QiuHong, H.; Falk, L. K. L.; Holmberg, K. *Langmuir* 2002, 18, 1811–1818.
- (5) Hamaoka, T.; Hayashi, H.; Tago, T.; Kishida, M.; Wakabayashi, K. *J. Colloid Interface Sci.* 2001, 235, 235–240.
- (6) Matsumoto, T.; Komatsu, T.; Arai, K.; Yamazaki, T.; Kijima, M.; Shimizu, H.; Takasawa, Y.; Nakamura, J. *Chem. Commun.* 2004, 840–841.
- (7) Hagen, C. M.; Vieille-Petit, L.; Laurenczy, G.; Suss-Fink, G.; Finke, R. G. *Organometallics* 2005, 24, 1819–1834.
- (8) Neri, G.; Rizzo, G.; Milone, C.; Galvagno, S.; Musolino, M. G.; Capannelli, G. *Appl. Catal., A* 2003, 249, 303–311.
- (9) (a) Yoon, B. Master's thesis, Kyung Hee University, Seoul, Korea, 1998. (b) Hmiciar, P.; Fabianova, K. *Chem. Zvesti* 1976, 30, 520–529.
- (10) He, J.; Ichinose, I.; Kunitake, T.; Nakao, A.; Shiraike, Y.; Toshima, N. *J. Am. Chem. Soc.* 2003, 125, 11034–11038.

JA055530F

Recyclable and Ligandless Suzuki Coupling Catalyzed by Carbon Nanotube-Supported Palladium Nanoparticles Synthesized in Supercritical Fluid

Horng-Bin Pan, Clive H. Yen, Byunghoon Yoon,
Masaki Sato, and Chien M. Wai

Department of Chemistry, University of Idaho, Moscow, Idaho, USA

Abstract: Carbon nanotube-supported palladium nanoparticles prepared by a supercritical fluid deposition method show high activities for catalyzing Suzuki coupling reactions, and the catalysts can be recycled and reused at least six times without losing activity.

Keywords: Carbon nanotube, palladium nanoparticles, supercritical fluid, Suzuki coupling

INTRODUCTION

The palladium-catalyzed Suzuki coupling reactions between arylboronic acids and aryl halides are widely used in organic syntheses.^[1] Both homogeneous and heterogeneous catalysts have been used for the coupling reactions. In general, heterogeneous catalysis is less effective than homogeneous catalysis but has advantages, including easy separation of catalysts for recycling. The efficiency of heterogeneous catalysis can be improved by employing nanoparticle catalysts because of their extremely large surface-to-volume ratios. An early study using palladium nanoclusters stabilized by tetraalkylammonium salts or by poly(vinylpyrrolidone) (PVP) as catalysts for Suzuki coupling reactions was reported by Reetz and coworkers.^[2]

Received in the USA April 19, 2006

Address correspondence to Chien M. Wai, Department of Chemistry, University of Idaho, Moscow, ID 83844, USA. E-mail: cwai@uidaho.edu

Recent reports showed that the shape of catalytic metal nanoparticles stabilized by PVP could affect catalysis, and near-spherical palladium nanoparticles were very effective for catalyzing the Suzuki coupling reactions.^[3] Because metal nanoparticles are generally unstable, exploration of appropriate supports for stabilizing catalytic nanoparticles is a key factor for their successful applications in heterogeneous catalysis. Carbon nanotubes provide a new type of support for stabilizing catalytic nanoparticles. Because of their small sizes, carbon nanotubes can be uniformly dispersed in a solution by mechanical stirring, thus increasing contacts between the reactants and the catalyst. Attaching metal nanoparticles to carbon nanotubes in aqueous solutions usually involves tedious processes with little control of particle size and distribution. A simple method of depositing metal nanoparticles on surfaces of multiwalled carbon nanotubes (MWCNT) using supercritical fluid carbon dioxide as a medium was reported recently.^[4] The method involves chemical reduction of a metal precursor dissolved in supercritical carbon dioxide in the presence of carbon nanotubes. Condensation and aggregation of the reduced metal lead to formation of metal nanoparticles on surfaces of curved carbon substrates. Near-spherical palladium nanoparticles with narrow size distributions can be formed on carbon nanotube surfaces. The curvature of the nanotubes is probably responsible for the formation of metal nanoparticles of a certain size range due to the contact angles allowed by the substrate surface during condensation.^[4] The catalytic activities of carbon nanotube-supported metal nanoparticles prepared by this method for organic reactions, including coupling reactions, have not been investigated. We have recently studied a number of Suzuki coupling reactions in methanol catalyzed by multiwalled carbon nanotube-supported palladium nanoparticles (Pd/MWCNT) prepared by a supercritical fluid deposition method. Very efficient Suzuki coupling reactions were observed under moderate temperatures without expensive ligands, and the Pd/MWCNT catalyst could be easily recycled for repeated use without losing activity. This new type of palladium catalyst appears to offer opportunities for a wide range of applications including organic syntheses and chemical manufacturing processes.

EXPERIMENTAL

The Pd/MWCNT catalyst was prepared according to a procedure described in a previous report.^[4] The method involved hydrogen reduction of palladium (II)-hexafluoroacetylacetone in supercritical fluid CO_2 in the presence of MWCNT at 80°C and 150 atm. After preparation, the samples were washed and sonicated in methanol and then dried for characterization. Transmission electron microscopy (TEM) images showed spherical particles attached to the surfaces of carbon nanotubes, and XPS (X-ray photon spectroscopy) showed that the Pd (3d_{5/2}) and Pd (3d_{3/2})

peaks at 335.3 eV and 340.6 eV, respectively, were consistent with the literature data for zero-valent metallic palladium. Energy dispersive X-ray fluorescence (EDS) was used for quantitative analysis of the Pd metal loading in our carbon nanotube catalysts, which was about 3% by weight. A commercial palladium/carbon black (Pd/C) catalyst was obtained from Aldrich.

General Procedures for Suzuki Coupling Reactions

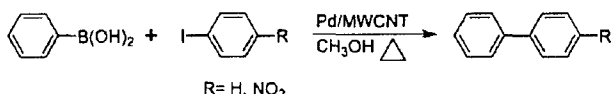
A 100 mL, three-necked, round-bottomed flask with a magnetic stirring bar was charged with Pd/MWCNT (10 mg, 3% Pd by weight), phenylboronic acid (1.1 mmol), aryl halide (1.0 mmol), sodium acetate (2.2 mmol), and methanol (25 mL). The mixture was vigorously stirred under reflux conditions in the open air. The extent of reaction was monitored by thin-layer chromatography (TLC) and 300 MHz nuclear magnetic resonance (NMR) spectroscopy (Bruker AMX 300).

After the reaction completion, the Pd/MWCNT settled down to the bottom of the flask. The organic layer was carefully removed. The solution was added with water and extracted with dichloromethane. The combined organic solution was dried with anhydrous MgSO_4 and concentrated in *vacuo*. The residue was purified by flash chromatography on silica gel with ethyl acetate–hexane = 1:10 as the eluent to give the desired products. The products were identified by comparison with ^1H NMR with those of authentic samples. The Pd/CNT was recovered almost quantitatively. After washing with methanol, the catalyst was reused for the next coupling experiment.

RESULTS AND DISCUSSION

The results of Suzuki coupling between phenylboronic acid and 1-iodo-4-nitrobene catalyzed by the Pd/MWCNT are shown in Table 1. In entry 1, after 30 min of reaction at 65°C, the isolated yield showed at least 94% conversion to the product (nitro-biphenyl) with a turnover frequency (TOF) of 709 h^{-1} . In comparison with a commercially available Pd/C catalyst, the TOF of the commercial catalyst for the same reaction under the same conditions was only 30 h^{-1} , about 24 times slower. Similarly, in the case of coupling between phenylboronic acid and iodobenzene, it required about 2 h to reach 95% of conversion. The TOF of MWCNT-supported Pd catalyst was also higher than that found with the commercial Pd/C catalyst by about a factor of 7 (Table 1).

The Suzuki cross-coupling reactions between phenylboronic acid and iodobenzene catalyzed by PVP-Pd colloidal in 40% EtOH aqueous solution under reflux conditions (temperature of boiling 40% EtOH about 80°C) were reported by Li et al.^[5] The reaction required 12 h to reach 95%

Table 1. Comparison of Pd/MWCNT with conventional Pd/C for Suzuki coupling

Entry	Aryl halide	Rxn time (h)	Product	Isolated yield %	TOF/h
1	1-Iodo-4-nitrobenzene	0.5 ^a	R=NO ₂	93 ^a	709
2	1-Iodo-4-nitrobenzene	3.5 ^b	R=NO ₂	94 ^b	30
3	Iodobenzene	2 ^a	R=H	95 ^a	177
4	Iodobenzene	4 ^b	R=H	95 ^b	27

^a10 mg Pd/CNT(3%) as described in the experimental section.

^b10 mg of conventional palladium catalyst on activated carbon (Pd content 10%, dry wt.) was used after dried in a oven for 2 h at 100°C.

conversion, and the Pd nanoparticles were agglomerated after one cycle, resulting in a loss of catalytic activity.

The speed of the coupling reaction depends on the nature of the substituted aryl halide. Table 2 shows the results of Suzuki coupling of phenylboronic acid and aryl halides with different substitution groups. With electron-withdrawing substitution groups (−NO₂, −COCH₃), the reaction rate is faster than nonsubstituted aryl halide. On the contrary, for the electron-donating groups (−OCH₃), the reaction rate is slower than nonsubstituted aryl halide. Aryl bromide is slower than corresponding aryl iodide for the coupling reaction with phenylboronic acid, but the reaction still proceeds well

Table 2. Pd/MWCNT catalyzed Suzuki coupling of phenylboronic acid with aryl halides

Entry	Aryl halide	Rxn time (h)	Product	Isolated yield %	TOF/h
1	4-Iodoacetophenone	0.75		94	473
2	4-Bromoacetophenone	1.5		94	236
3	4-Iodoanisole	3.5		92	118
4	2-Iodothiophene	2.5		94	142
5	1,4-Diiodobenzene	5		95	71
6	1-Bromo-4-nitrobenzene	1		92	355
7	Bromobenzene	3.5		95	101

Table 3. Suzuki coupling reaction of 4-iodobenzene and phenylboronic acid using recycled Pd/MWCNT as catalyst

Pd/CNT	Conversion %	Isolated yield %
Fresh	>99	94
1st reused	>99	96
2nd reused	>99	95
3rd reused	>99	94
4th reused	>99	95
5th reused	>99	96
6th reused	>99	96

with good conversion using the Pd/CNT catalyst. In a previous report, Kabalka et al. used a large amount of palladium black (50 mg) as catalyst for Suzuki coupling with aryl bromides, and the substrates were found ineffective.^[6] In entry 4, coupling between 2-iodothiophene and phenylboronic acid was also studied, and the reaction proceeded well, as shown in Table 2. However, coupling of 1,4-diiiodobenzene with 2 molecules of phenylboronic acid to form triphenyl is the slowest reaction observed in this study, requiring 5 h to reach 95% conversion.

The activity of the recycled Pd/MWCNT was tested by the reaction of 4-iodobenzene with phenylboronic acid. As shown in Table 3, the activity of the MWCNT-supported Pd catalyst remained almost unchanged even after recycling six times. TEM micrographs of the recycled Pd/MWCNT catalysts showed little change of the particle density on the MWCNT surfaces, but some larger particles up to 40 nm were observed after six uses.

CONCLUSION

In summary, we have shown that Pd/MWCNT made by a supercritical fluid deposition method can efficiently catalyze the Suzuki coupling reactions without expensive ligands and can be reused many times without loss of catalytic activity. Biaryl structures are present in a variety of common natural products,^[7] conjugated polymers,^[8] and liquid crystalline materials^[8,9] that require Suzuki coupling reactions for synthesis. The Pd/CNT catalyst described in this report should have a wide range of applications in organic synthesis and design for durable nanoparticle catalysis.

ACKNOWLEDGMENTS

This work was supported by U. S. Air Force Office for Scientific Research (AFOSR) (F49620-03-1-0361).

REFERENCES

1. (a) Miyaura, N.; Suzuki, A. Palladium-catalyzed cross-coupling reactions of organoboron compounds. *Chem. Rev.* **1995**, *95*, 2457–2483; (b) Suzuki, A. Recent advances in the cross-coupling reactions of organoboron derivatives with organic electrophiles. *J. Organomet. Chem.* **1999**, *576*, 147–168; (c) Kotha, S.; Lahiri, K.; Kashinath, D. Recent applications of the Suzuki–Miyaura cross-coupling reactions in organic synthesis. *Tetrahedron* **2002**, *58*, 9633–9695; (d) Moreno-Manas, M.; Pleixats, R. Formation of carbon–carbon bonds under catalysis by transition-metal nanoparticles. *Acc. Chem. Res.* **2003**, *36*, 638–643.
2. Reetz, M. T.; Breinbauer, R.; Wanninger, K. Suzuki and Heck reaction catalyzed by preformed palladium clusters and palladium/nickel bimetallic clusters. *Tetrahedron Lett.* **1996**, *37*, 4499–4502.
3. Narayanan, R.; El-Sayed, M. A. Effect of colloidal nanocatalysis on the metallic nanoparticle shape: The Suzuki reaction. *Langmuir* **2005**, *21*, 2027–2033.
4. (a) Ye, X. R.; Lin, Y. H.; Wai, C. M. Decorating catalytic palladium nanoparticles on carbon nanotubes in supercritical carbon dioxide. *Chem. Commun.* **2003**, 642–643; (b) Ye, X. R.; Lin, Y. H.; Wang, C.; Engelhard, M. H.; Wang, Y.; Wai, C. M. Supercritical fluid synthesis and characterization of catalytic metal nanoparticles on carbon nanotubes. *J. Mater. Chem.* **2004**, *14*, 908–913.
5. (a) Li, Y.; Hong, X. M.; Collard, D. M.; El-Sayed, M. A. Suzuki cross-coupling reactions catalyzed by palladium nanoparticles in aqueous solution. *Org. Lett.* **2000**, *2*, 2385–2388; (b) Narayanan, R.; El-Sayed, M. A. Effect of catalysis on the stability of metallic nanoparticles: Suzuki reaction catalyzed by PVP–palladium nanoparticles. *J. Am. Chem. Soc.* **2003**, *125*, 8340–8347.
6. Kabalka, G. W.; Namboodiri, V.; Wang, L. Suzuki coupling with ligandless palladium and potassium fluoride. *Chem. Commun.* **2001**, 775.
7. Nicolaou, K. C.; Bulger, P. G.; Sarlah, D. Palladium-catalyzed cross-coupling reactions in total synthesis. *Angew. Chem. Int. Ed.* **2005**, *44*, 4442–4489.
8. Hoeben, F. J. M.; Jonkheijm, P.; Meijer, E. W.; Schenning, P. H. J. About supramolecular assemblies of π -conjugated systems. *Chem. Rev.* **2005**, *105*, 1491–1546.
9. (a) Shen, D.; Pegenaue, A.; Diele, S.; Wirth, I.; Tschierske, C. Molecular design of nonchiral bent-core liquid crystals with antiferroelectric properties. *J. Am. Chem. Soc.* **2000**, *122*, 1593–1601; (b) Kishikawa, K.; Harris, M. C.; Swager, T. M. Nematic liquid crystals with bent-rod shapes: Mesomorphic thiophenes with lateral dipole moments. *Chem. Mater.* **1999**, *11*, 867–871.

Fluorescence of Aromatic Amines and Their Fluorescamine Derivatives for Detection of Explosive Vapors

DELYLE EASTWOOD,* CARLOS FERNANDEZ, B. YUNGHOON YOON,
CHRYSSTAL N. SHEAFF, and CHIEN M. WAI

Department of Chemistry, University of Idaho, P.O. Box 442343 Moscow, Idaho 83844-2343

Nitroaromatics (such as dinitrotoluene, trinitrotoluene, and nitrobenzene) found in explosive vapors from buried landmines can be reduced to aminoaromatics by a novel process involving Pd metal nanocatalysts prepared in supercritical fluid carbon dioxide and supported on multi-walled carbon nanotubes. These aminoaromatics are fluorescent and, if desired, the fluorescence yield can be increased and the fluorescence maxima shifted further toward the red by reaction with appropriate derivatizing agents such as fluorescamine. Corrected spectra for these chemicals and their derivatives are included. Subpicomolar detection limits have already been achieved using a laboratory spectrofluorometer with a 150 W Xe arc lamp. Using lasers as excitation sources, this approach has the potential for developing a field sensor competitive with other methods currently used for detecting explosive vapors from land mines.

Index Headings: Aminoaromatics; Explosive vapors; Fluorescence; Nitroaromatics; Palladium nanoparticles.

INTRODUCTION

Thousands of forgotten buried landmines exist all over the world. It is also common knowledge that plastic landmines and improvised explosive devices (IEDs) are causing many casualties in Iraq. Most of these mines contain TNT (2,4,6-trinitrotoluene). TNT is also commonly the analyte of most interest near munitions factories or storage areas. Some of the techniques for detection assume metallic mines or require very expensive instrumentation or are otherwise unreliable. The best detection, especially for plastic mines, involves detection of a mixture of vapors leaking from the mines. These are impurities or degradation products such as 2,4-dinitrotoluene (DNT),¹ which are more volatile than TNT by at least a couple of orders of magnitude. Other dinitrotoluenes or other aromatic nitrated species such as TNT, nitrotoluene, or nitrobenzene may be present, but can be handled similarly to the procedure described in this paper. For this application very low levels of vapors, lower than parts-per-trillion levels, must be measured. References on the chemistry of explosives and related field detection are included.²⁻⁶ Several electronic "noses" using different techniques have also been proposed and perhaps the most promising is "FIDO" which uses fluorescent polymers developed by T. Swager³ and incorporated in an electronic nose by Nomadics Company (Stillwater, OK). In this case the nitroaromatics such as DNT quench specially synthesized fluorescent polymers. Fluorescence quenching may not be specific enough for some forensic applications, and also the fluorescent polymer may not be reliable and reproducible enough, as well as being expensive to produce in bulk. In any case, after a reduction step, direct fluorescence of the aromatic amines or their derivatives provides an alternative approach,

providing greater specificity, which might have advantages for certain applications. An environmental high-performance liquid chromatography (HPLC) method with fluorescence detection for aminoaromatics in soil has been reported.⁷ This is a laboratory method and requires the use of more solvent. To the extent that we are talking about explosive vapors rather than soil or ground water samples, most matrix and quenching effects are eliminated. As stated in Guilbault,⁸ aromatic nitro compounds are not good candidates for analysis by fluorescence spectroscopy unless they are converted chemically into fluorescent compounds with amino groups by chemical reduction. Fluorescence spectra of aminoaromatics have been reported in the literature.⁸⁻¹⁰ Kasha^{11,12} has discussed the theory of fluorescence for chemicals like the aromatic amines.

The current paper includes an updated, corrected set of fluorescence spectra using the purest aromatic amines available including aniline, o- and p-toluidines, 2,4- and 2,6-diaminotoluene, and 2,4,6-triaminotoluene. For the sort of mixture of explosive vapors in which we are most interested, 2,4-DNT, which can be reduced to 2,4-DAT, has been reported as the major specie.¹ Fluorescent fluorescamine derivatives of aromatic amines are known^{8,13} and we also include several examples for these aromatic amine derivatives. Recently, a Siberian group^{14,15} proposed a scheme for reducing nitroaromatics to aminoaromatics as a similar way of measuring explosive vapors, but they used different reducing agents, included no spectra of the aminoaromatics, and gave only one example of a spectrum of a fluorescamine derivative. Our proposed technique uses catalysis by metallic (Pd) nanoparticles¹⁶⁻¹⁸ synthesized in supercritical fluid carbon dioxide or water-in-hexane microemulsion and supported on carbon nanotubes to efficiently reduce the nitroaromatics to aminoaromatics, which are fluorescent themselves. UV-VIS fluorescence is the best and simplest ultratrace technique, being capable with laser excitation as an option of even single molecule detection. This fluorescence technique can be made extremely sensitive (fluorescence derivatization with reagents such as fluorescamine can make the derivatized amines even more highly fluorescent) and the fluorescence can be shifted further to the red where there is less background fluorescence. In this paper we discuss the fluorescence spectra and chemistry required as a framework for proving such a field sensor feasible. Initial tests were made with a spectrofluorometer (Spex FluoroMax-3TM) having a 150 watt Xe arc lamp for tunability. A small laser may be substituted for extra sensitivity, once the desired wavelength (for the fluorescamine derivative of DAT at about 391 nm) is determined. These measurements are designed to show that direct detection of aromatic amines or their derivatives can provide an alternative approach for measuring explosives to fluorescence quenching of nitroaromatic components of explosives.

Received 21 April 2006; accepted 8 June 2006.

* Author to whom correspondence should be sent. E-mail: delyle@uidaho.edu.

EXPERIMENTAL

Instrumentation. Standard fluorescence measurements of the aminoaromatics and their derivatives with fluorescamine were used to generate excitation and emission spectra using a Spex (HORIBA Jobin Yvon) analytical grade spectrofluorometer (FluoroMax-3TM) with a 150 watt Xe arc lamp. The instrument was calibrated by measuring the spectrum of the xenon lamp for the excitation monochromator (wavelength calibration and intensity), measuring the water Raman (intensity), and a Starna standard of ovalene in polymethylmethacrylate (PMMA) for the emission monochromator (wavelength calibration and intensity). Wavelength accuracy was better than 1 nm and the water Raman was initially above manufacturer's specifications in intensity, indicating that the xenon lamp was more intense than expected. Excitation and emission spectra were measured using several excitation and detection wavelengths and several bandwidths (typically 5 or 10 nm), all of which were narrow compared to the broad emission and excitation spectra for the aromatic amines or their derivatives. Fluorescence references applicable to these types of samples are included for reference.^{19,20} For the aromatic amines, monochromator bandwidths were 5.0 nm, 1 nm increments, and 0.1 second integration time. For the derivatized aromatic amines, monochromator bandwidths of 10 nm, 1 nm increments, and integration time of 0.1 second were used to lower the detection limit. Starna fused silica 1 cm path length cells were used with right-angle excitation for the solutions. For a few solutions, absorption spectra were recorded for comparison with the excitation spectra using a Spectral Instruments, Inc (Tucson, AZ) charge-coupled device (CCD) array UV-VIS spectrophotometer with fiber optics. ¹H nuclear magnetic resonance (NMR) spectra were measured on a Bruker (AMX300, CDCl₃) spectrometer at room temperature. Data were recorded as chemical shift values in ppm on the δ scale, multiplicity, integration, and coupling constants.

Reagents. The reagents were all used as received and were the highest grade obtainable. Only ethanol (200 proof USP or from Aldrich for microbiology) was used as solvent for the measurements reported here. Nitric acid (singly distilled from Aldrich) and HPLC grade water, also from Aldrich, were used for cell cleaning. Dinitrotoluene (2,4-DNT) was used from Sigma-Aldrich for the reduction reaction described below to produce diaminotoluene (2,4-DAT). 2,4-DAT was first obtained from Sigma-Aldrich (98%) and later from AccuStandard Inc (99.4%), 2,6-diaminotoluene (2,6-DAT) (99.7%) was also obtained from AccuStandard. Triaminotoluene (2,4,6-TAT) and aniline (aminobenzene) as likely typical minor components of an explosive vapor mixture after reduction were also obtained from AccuStandard Inc. O-Toluidine (97% or better) and p-toluidine (97% or better), also likely minor components of an explosive vapor mixture after reduction, were obtained from Sigma. A fluorescence derivatization agent fluorescamine (98%) was obtained from Molecular Probes, now a division of Invitrogen Inc. Although fluorescamine is supposed to be completely non-fluorescent in the absence of reactive amines, so that a surplus would not matter, it was found to be weakly fluorescent, presumably due to an unidentified impurity. Finally, fluorescein from Fluka (now affiliated with Sigma-Aldrich) was used to check the limit of detection of the instrument in a basic (NaOH) solution. For thin-layer chromatography (TLC) analysis, a Sigma-Aldrich TLC plate

(silica gel with gypsum binder and fluorescent indicator) was used.

Synthesis of Catalyst. Catalytic nanoparticles of Pd were prepared in house for the reduction of nitro compounds such as DNT and other aromatic compounds as discussed in more detail in previous publications.¹⁶⁻¹⁸ The water-in-hexane microemulsions were prepared at 25 °C by mixing 0.1 M of Na₂PdCl₄ solution (0.864 mL) with 200 mL of n-hexane and sodium dioctyl sulfosuccinate (AOT, 1.7782 g, 4 mmol), which gave a W value of 12;¹⁸ W value is defined as the water to the surfactant molar ratio ([water]/[surfactant]). Multi-walled carbon nanotubes (MWCNTs) (1.0 g, 60–100 nm in diameter, Nanostructure & Amorphous Materials Inc, Los Alamos, NM) were pretreated by sonication in 14 M HNO₃ for 1 h and then refluxed for 12 h in a mixture of HNO₃ (50 mL, 14 M) and H₂SO₄ (98 % 50 mL). The treated MWCNTs (0.030 g) were added to the microemulsion solution with continuous stirring. Hydrogen gas at 1 atm was then bubbled through the solution for 30 min to reduce the Pd²⁺ ions dissolved in the water core of the microemulsion. It is known that hydrogen gas can cause reduction of Pd²⁺ ions in aqueous solutions to their elemental state.¹⁷ After hydrogen reduction, the CNT-supported metal nanoparticles would precipitate to the bottom of the flask without stirring. The CNT-supported Pd nanoparticle catalyst was collected from the flask, washed with methanol, and dried in an oven for hydrogenation experiments.

Formation and Derivatization of DAT starting with 2,4-DNT. 2,4-Dinitrotoluene (0.0182 g, 0.1 mmol) in 10 mL of ethanol (10⁻² M) with Pd/CNT (0.010 g) was stirred and then hydrogen was bubbled through the solution for 2 min at room temperature to make sure that DNT conversion to DAT was complete; TLC (eluent; 25% ethyl acetate and 75% n-hexane) was checked under UV light (254 nm) and then visualized by ninhydrin agent (red color). No starting materials were detected by TLC (DNT, R_f value = 0.45) and the product was DAT; ¹H NMR (300 MHz, CDCl₃): δ = 6.83 (s, 1H), δ = 6.11 (d, 2H, J = 8.4 Hz), δ = 3.50 (s, 4H), δ = 2.08 (s, 3H).

To increase the fluorescence yield, DAT was reacted with fluorescamine reagent: 10⁻⁷ M DAT and 4 × 10⁻⁷ M fluorescamine (diluted down by a factor of 10 from the ethanol solution of 10⁻⁶ M DAT and 4 × 10⁻⁶ M fluorescamine (4 × 0.00278 mg), in 10 mL of ethanol and the solution was shaken for 2 min (longer than needed) at room temperature (RT). The solution was diluted by a factor of 10 after detection of fluorescence peaks and then this dilution procedure was repeated to reach 10⁻¹² M of the solution. These DAT derivatives and other solutes being measured by fluorescence were stored in amber glass vials and further protected from ambient room light by aluminum foil to reduce risk of photoreactivity.

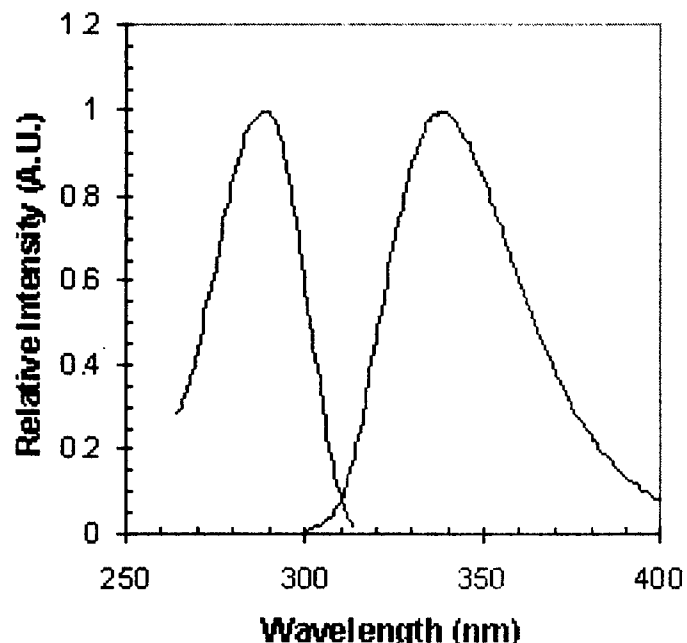
RESULTS AND DISCUSSION

A summary of the data for excitation and emission spectral peaks for the aromatic amines and their fluorescamine derivatives are given in Tables I and II. Figures 1–8 show the actual excitation and emission fluorescence data for the corrected and solvent-subtracted spectra: (Fig. 1) aniline, (Fig. 2) p-toluidine and o-toluidine, (Fig. 3) 2,6-DAT and 2,4-DAT, (Fig. 4) 2,4,6-TAT, (Fig. 5) aniline + fluorescamine, (Fig. 6) p-toluidine + fluorescamine and o-toluidine + fluorescamine, (Fig. 7) 2,4-DAT + fluorescamine at concentrations ranging from 10⁻⁸ M to 10⁻¹² M, and (Fig. 8) 2,4,6-TAT +

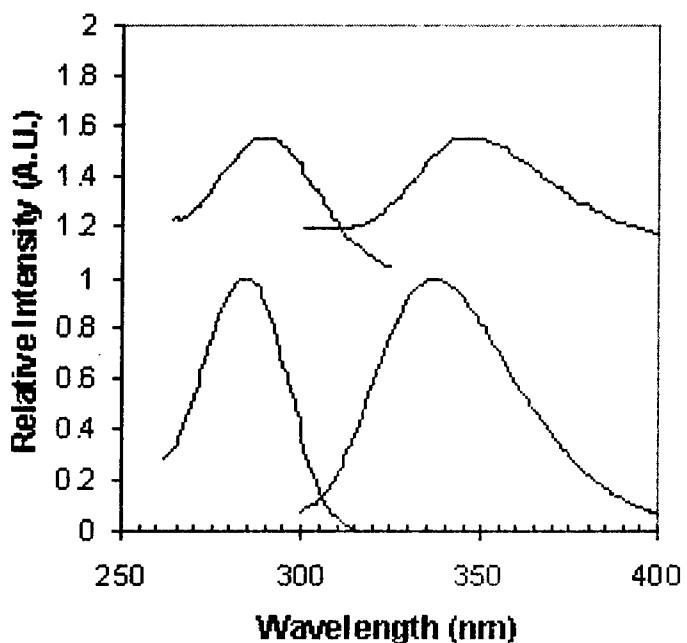
TABLE I. Fluorescence data for aromatic amines.

Chemical	Excitation (nm)	Emission (nm)	Comments
Aniline	285	341	Ex & Em 10^{-6} M, bandwidths 5.0 nm
p-Toluidine	290	346	Ex & Em 10^{-6} M, bandwidths 5.0 nm
o-Toluidine	282	339	Ex & Em 10^{-6} M, bandwidths 5.0 nm
2,4-DAT (Diaminotoluene)	283	343	Ex & Em 10^{-6} M, bandwidths 5.0 nm
2,6-DAT (Diaminotoluene)	287	336	Ex & Em 10^{-5} M, bandwidths 5.0 nm
2,4,6-TAT (Triaminotoluene)	294	347	Ex & Em 10^{-4} M, bandwidths 5.0 nm

fluorescamine. The aromatic amines shown in Figs. 1–4 are likely fluorescent impurities in a mixture of explosive vapors after reduction, with 2,4-DAT being the major component. The aniline fluorescence spectrum was previously recorded in Ref. 9. The fluorescent derivatives of these compounds with fluorescamine¹³ were also measured (Figs. 5–8) and in the case of 2,4-DAT as a function of several concentrations. DAT + fluorescamine led to a detection limit of 10^{-12} M when exciting at 392 nm (Fig. 7). The measured spectra, as are typical of aromatic phenols and amines, are broad (full-width at half-maximum (FWHM) of 56 nm for the emission spectra of 2,4-DAT 10^{-6} M) and without vibrational structure. They all have an excitation peak in the range of 280–300 nm and an emission peak between 330 and 350 nm. Although these spectra are similar, they can probably be distinguished by using synchronous luminescence and pattern recognition techniques, which we plan to discuss in follow-up publications. The excitation and emission spectra of the fluorescamine derivatives are red-shifted, broader (FWHM of 86 nm for the emission spectrum of 2,4-DAT at 10^{-9} M), and more intense. The emission intensity of a 10^{-6} M solution of DAT + fluorescamine derivative was found to be several orders of magnitude greater than a 10^{-6} M solution of DAT under the same experimental conditions (same bandwidths). The excitation peaks appear in a range of 380 to 410 nm. (For excitation purposes in a field instrument or sensor, it is preferable to

FIG. 1. Excitation and emission spectra of aniline 10^{-6} M. Bandwidth: 5 nm.

excite as far towards the blue as possible, where better and cheaper sources exist.) The emission spectra of the fluorescamine derivatives show a single peak in the range of 480 to 510 nm. The instrumental conditions are given in each figure caption. For some compounds it was necessary to narrow the bandwidths to avoid entering the nonlinear saturation region for the photon-counting photomultiplier tube (PMT) detector, which was above 2.5 million counts per second (cps). All spectra were analyzed at least in duplicate; most were measured in triplicate or higher. Spectral peak heights for 2,4-DAT + fluorescamine were linear over the concentration range of 10^{-10} to 10^{-12} M, but were not linear above this concentration

FIG. 2. Excitation and emission spectra of (top) p-toluidine 10^{-6} M and (bottom) o-Toluidine 10^{-6} M. Bandwidths: 5 nm.

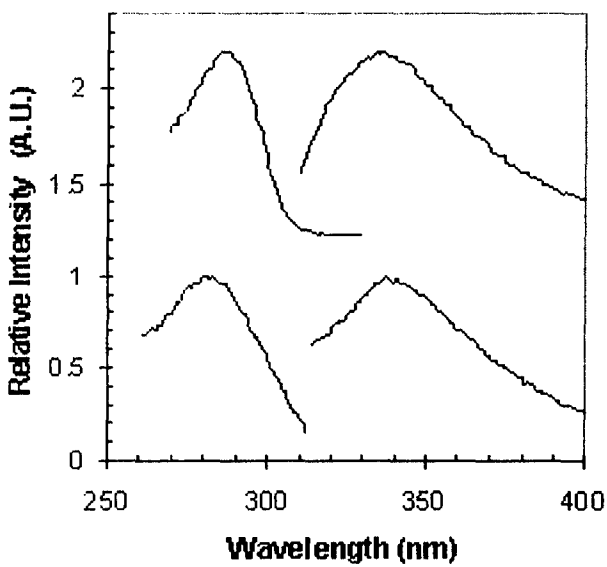


FIG. 3. Emission and excitation spectra of (top) 2,6-DAT 10^{-6} M and (bottom) 2,4-DAT 10^{-6} M. Bandwidths: 5 nm.

even with solvent blank subtraction. In addition, a slight blue shift in the emission peak of 2,4-DAT after ethanol subtraction was observed as the concentration of DAT decreased probably due to a slight under-correction of the solvent blank on a very weak signal. 2,4-DAT was linear over the concentration range of 10^{-4} to 10^{-6} M. Provided the data are sufficiently reproducible, a calibration curve can be constructed even outside the linear range. For six replications of 2,4-DAT + fluorescamine at 10^{-6} M, the relative standard deviation was 11%. Most of the spectra are normalized to the highest fluorescence emission peak in the figure. Table I gives fluorescence spectral data for aromatic amines including

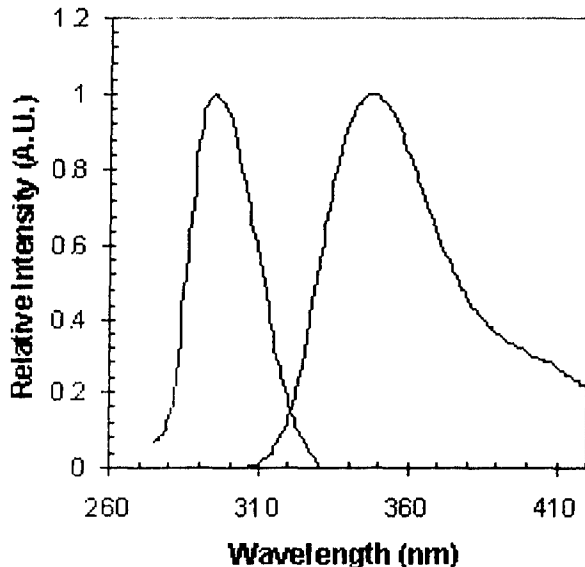


FIG. 4. Emission and excitation spectra of 2,4,6-TAT 10^{-4} M. Bandwidths: 5 nm.

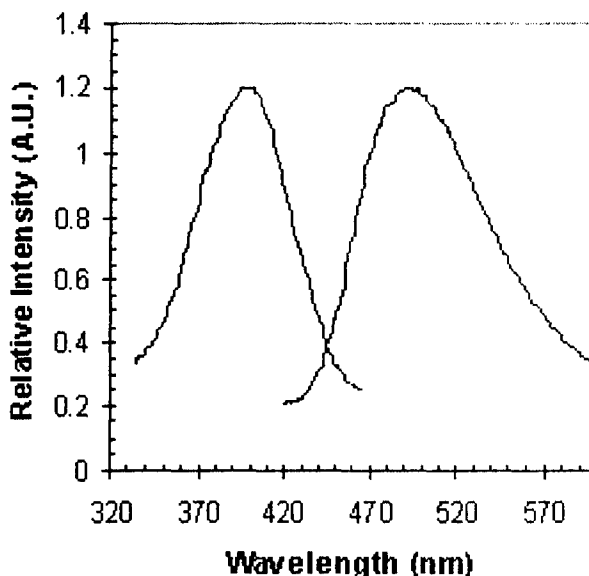


FIG. 5. Emission and excitation spectra of Aniline + Fluorescamine 10^{-8} M. Bandwidths: 10 nm.

excitation and emission peak positions, instrumental bandwidths, and concentrations (aniline, p-toluidine, o-toluidine, 2,4-DAT, 2,6-DAT, and 2,4,6-TAT). Table II gives fluorescence spectral data for derivatized aromatic amines including excitation and emission peak positions, instrumental bandwidths, and concentrations (fluorescamine derivatives of aniline, p-toluidine, o-toluidine, 2,4-DAT, 2,6-DAT, and 2,4,6-TAT).

Fluorescein standard (quantum yield approximately 0.9) in a basic solution was measured to give a detection limit of 10^{-12} M. This result was similar to what Spex had claimed for this

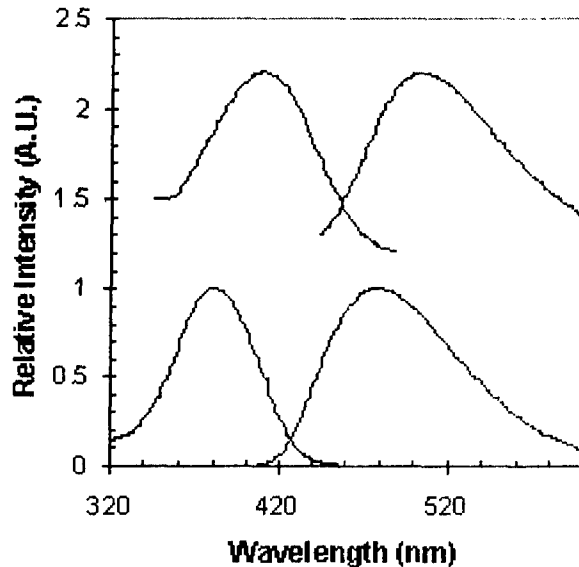


FIG. 6. Emission and excitation spectra of (top) p-Toluidine + Fluorescamine 10^{-6} M and (bottom) o-Toluidine + Fluorescamine 10^{-6} M. Bandwidths: 5 nm.

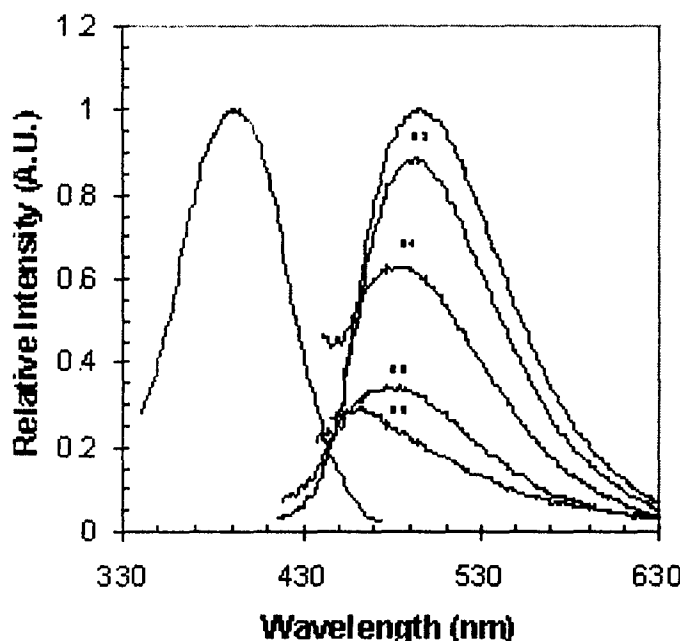


Fig. 7. Emission and excitation spectra of 2,4-DAT + Fluorescamine at 10^{-8} M, 10^{-9} M (multiplied by 3), 10^{-10} M (multiplied by 4), 10^{-11} M (multiplied by 5), and 10^{-12} M (multiplied by 5) in consecutive order (solvent blank subtracted). Bandwidths: 10 nm.

instrument for fluorescein in a recent application note.²¹ A FluoroLog-3TM instrument with a cooled PMT (which would further reduce instrumental noise and scattered light) can detect as low as 50 femtoMol of fluorescein.²¹

Recent experiments in our laboratory, using small stainless steel tubing with a diameter of 3 mm and a length of 13 cm packed with carbon nanotube-supported palladium nanoparticles for conversion of DNT to DAT in air with saturated DNT vapors and hydrogen gas (bubbling through an ethanol solution containing 10^{-6} M fluorescamine at 0.7 L per min at room temperature), showed that 1 min of flow was enough to detect the fluorescence emission of DAT-fluorescamine derivative in the solution.

CONCLUSION

The purpose of this preliminary paper was to show, using a commercial instrument, the feasibility of developing a fluorescence method or miniaturized field sensor for detection of explosive vapors as an alternative to fluorescence quenching methods currently being field tested. We have included a corrected updated UV-VIS fluorescence spectral library (Figs. 1–4) for the aromatic amines in Table I, and for their fluorescamine derivatives (Figs. 5–8), which have lower detection limits but broader spectra, in Table II. For 2,4-diaminotoluene + fluorescamine, we have measured the fluorescence intensity as a function of concentration, with a standard deviation of 11% at 10^{-6} M. The detection limit was found to be 10^{-12} M under the conditions of the experiment.

We also demonstrated the reduction of 2,4-DNT to the corresponding DAT and its reaction with fluorescamine. This was made by bubbling the DNT vapor through the Pd nanocatalysts, suspended on multiwalled carbon nanotubes, in the presence of hydrogen gas, and an ethanol solution of fluorescamine. Evidently, by using more powerful laser sources and more sensitive detectors with lower noise, the detection

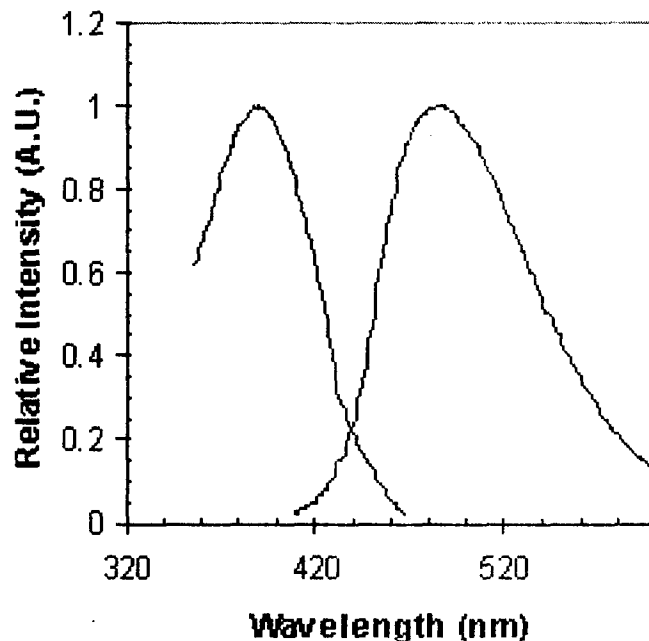


Fig. 8. Emission and excitation spectra of 2,4,6-TAT + Fluorescamine 10^{-6} M. Bandwidths: 10 nm.

levels could be lowered further than the 10^{-12} M reported here, or the aromatic amines could be measured directly without need for derivatization, which would permit greater specificity, if needed. Reaction kinetics could be altered by changing experimental conditions to make the speed of the reactions more competitive with other procedures. The present conditions are optimized for 2,4-diaminotoluene reduced from 2,4-dinitrotoluene by a novel method. 2,4-DNT is likely to be the main component in explosive vapors leaking from a plastic landmine containing TNT.¹ An alternative approach might call for deposition on a solid substrate (cold finger) or to measure the DAT directly in the vapor phase. This method could be modified to apply to other explosive mixtures or be applied to explosives extracted from soil with supercritical fluid carbon dioxide.

ACKNOWLEDGMENTS

This work was partially supported by a grant from DOD-AFOSR (f49620-03-1-0361). The authors (D.E. and C.M.W.) also want to acknowledge helpful discussions with technical contacts from HORIBA Jobin Yvon (Spex Fluorescence Division) (Ray Kaminski, James Mattheis, and Karen Rubelowsky). We also wish to acknowledge useful conversations with Ernesto Cespedes of the Idaho National Laboratory.

1. A. B. Crockett, T. F. Jenkins, H. D. Craig, and W. F. Sisk, "Overview of On-Site Analytical Methods for Explosives in Soil", Special Report 98-4 (NTIS, Springfield, VA, February, 1998).
2. J. Akhavan, *The Chemistry of Explosives* (The Royal Society of Chemistry, London, 1998).
3. T. Swager, in *Electronic Noses and Sensors for the Detection of Explosives*, J. W. Gardner and J. Yinon, Eds. (Kluwer Academic Publishers, Boston, 2004).
4. M. Fisher and J. Sikes, in *Electronic Noses and Sensors for the Detection of Explosives*, J. W. Gardner and J. Yinon, Eds. (Kluwer Academic Publishers, Boston, 2004).
5. J. Yinon, *Forensic and Environmental Detection of Explosives* (John Wiley and Sons, New York, 1999).
6. J. Yinon and S. Zitrin, *Modern Methods and Application in Analysis of Explosives* (John Wiley and Sons, New York, 1993).
7. C. M. Pace, J. R. Donnelly, J. L. Jeter, W. C. Brumley, and G. W. Sovocool, J.—Assoc. Off. Anal. Chem., Intertl. **79**, 777 (1996).

8. G. G. Guilbault, Ed., *Practical Fluorescence* (Marcel Dekker, New York, 1990), 2nd ed., Revised and Expanded, pp. 99–100.
9. I. B. Berlin, *Handbook of Fluorescence Spectra of Aromatic Molecules* (Academic Press, New York, 1965), pp. 59–60.
10. J. T. Brownrigg, D. A. Busch, and L. P. Giering, *A Luminescence Survey of Hazardous Materials*, Report No. CG-D-53-79 (NTIS, May, 1979).
11. M. Kasha and R. Rawls, *Photochem. Photobiol.* **7**, 561 (1968).
12. M. Kasha, *Discuss. Faraday Soc.* **9**, 14 (1950).
13. R. P. Haugland, *The Handbook, A Guide to Fluorescent Probes and Labeling Technologies* (Invitrogen Corp., Eugene, OR, 2005), 10th ed.
14. V. N. Ivanova and V. A. Nadolinniy, *Khimiya v Interesakh Ustoichivogo Razvitiya* **11**, 353 (Publisher Siberian Branch of Russian Academy of Science) (2003).
15. V. A. Nadolinniy, V. N. Ivanova, and S. N. Lunegov, *Khimiya v Interesakh Ustoichivogo Razvitiya*, **11**, 391 (2003).
16. M. Ohde, H. Ohde, and C. M. Wai, *Langmuir* **21**, 1738 (2005).
17. B. Yoon, H. Kim, and C. M. Wai, *Chem. Commun.* **9**, 1040 (2003).
18. B. Yoon and C. M. Wai, *J. Am. Chem. Soc.* **127**, 17174 (2005).
19. C. A. Parker, *Photoluminescence of Solutions* (Elsevier, New York, 1968).
20. J. R. Lakowicz, *Principles of Fluorescence Spectroscopy* (Kluwer Academic/Plenum Publishers, New York, 1999), 2nd ed., pp. 79–80.
21. Spex Fluorescence Group, Application Notes F-1, “Sub-Picomolar Fluorescein” (HORIBA Jobin Yvon Inc, Edison, NJ, 2000).

Increasing Selectivity for TNT-Based Explosive Detection by Synchronous Luminescence and Derivative Spectroscopy with Quantum Yields of Selected Aromatic Amines

CHRYSSTAL N. SHEAFF, DELYLE EASTWOOD,* and CHIEN M. WAI*

Department of Chemistry, University of Idaho, P.O. Box 442343 Moscow, Idaho 83844-2343

The detection of explosive material is at the forefront of current analytical problems. A detection method is desired that is not restricted to detecting only explosive materials, but is also capable of identifying the origin and type of explosive. It is essential that a detection method have the selectivity to distinguish among compounds in a mixture of explosives. The nitro compounds found in explosives have low fluorescent yields or are considered to be non-fluorescent; however, after reduction, the amino compounds exhibit relatively high fluorescence. We discuss how to increase selectivity of explosive detection using fluorescence; this includes synchronous luminescence and derivative spectroscopy with appropriate smoothing. By implementing synchronous luminescence and derivative spectroscopy, we were able to resolve the reduction products of one major TNT-based explosive compound, 2,4-diaminotoluene, and the reduction products of other minor TNT-based explosives in a mixture. We also report for the first time the quantum yields of these important compounds. Relative quantum yields are useful in establishing relative fluorescence intensities and are an important spectroscopic measurement of molecules. Our approach allows for rapid, sensitive, and selective detection with the discrimination necessary to distinguish among various explosives.

Index Headings: Aromatic amines; Nitro aromatics; Explosive vapors; Fluorescence; Synchronous luminescence; Derivative spectroscopy; Quantum yields.

INTRODUCTION

Plastic landmines and improvised explosive devices (IEDs) are known problems that cause civilian casualties in different regions of the world. Over 1.2 million forgotten landmines in the world are responsible for thousands of deaths and injuries to people each year.¹ The best way to identify these explosives is to detect the explosive vapors leaking from the plastic mines. Most of the landmines and explosive devices contain 2,4,6-TNT (2,4,6-trinitrotoluene)-based explosives. Explosive vapors from the TNT mixture often include trinitrotoluenes, dinitrotoluenes, mononitrotoluenes, trinitrobenzenes, dinitrobenzenes, and nitrobenzene.¹ The relative concentrations and vapor pressures of these components under various environmental conditions (e.g., above buried landmines) are given in the literature.^{1,2} It is reported that, of these possible compounds, 2,4,6-TNT, 2,4-dinitrotoluene (2,4-DNT), and 1,3-dinitrobenzene (1,3-DNB) are the major chemical components.¹ TNT is known to have a vapor pressure that is lower than that of 2,4-DNT,² while 1,3-DNB is not only detected less frequently than 2,4-DNT but is also less stable.¹ For these reasons, 2,4-DNT is the compound that is most often used for the detection and confirmation of explosive vapors.

To date, there is not a detection method for explosive vapors

that completely meets all the current requirements of being rapid, sensitive, selective, and field portable. Several methods for detecting explosive vapors include, but are not limited to, gas chromatography-mass spectroscopy (GC-MS), ion mobility spectroscopy (IMS), dogs, and most recently the electronic nose.³ Although all of the current methods offer advantages, each has its own disadvantages. GC-MS suffers from lack of speed and is not field portable; IMS suffers from masking effects and is subject to frequent false alarms; and dogs have the disadvantages of fatigue and limited workload. Currently, the most promising method for the detection of explosives involves using an electronic nose, such as "FIDO".⁴ This electronic nose uses a fluorescent polymer to detect nitro aromatics through fluorescence quenching. Although this method of explosive detection is sensitive and field portable, it is expensive to produce in bulk and does not allow for the specificity that may be required for explosive signatures and forensic analysis. The disadvantages of the current methods make it clear that there is a need for a new approach to detect explosives that is rapid, sensitive, and selective, while still having the capability of being field portable. The inherently highly sensitive nature of fluorescence makes it ideal for detecting explosive vapors.

The molecular electronic transitions for the nitro aromatic compounds, which are found in explosive vapors, have low to no fluorescence yields. This is due to high intersystem crossing rates ($S_1^* \rightarrow T_n^*$),⁵ which yield non-fluorescent (radiationless) decay. The $-NO_2$ substituent on aromatic rings is an electron-withdrawing group, therefore causing a charge transfer transition from the ring to the nitro group.⁵ The lone pair of electrons on the $-NO_2$ gives an $n \rightarrow \pi^*$ transition, which, from selection rules, forbids radiative decay. If, however, the nitro aromatics are converted to aromatic amines, upon reduction, the molecular electronic transitions allow for relatively intense fluorescence of the aromatic amines.⁵ The main reason for the increase in the fluorescence of aromatic amines is due to a $\pi \rightarrow \pi^*$ transition. This transition occurs because the $-NH_2$ substituent is a strong electron-donating group, therefore providing electrons to the ring and subsequently allowing for radiative decay. It can be considered that the $-NO_2$ substituent involves an $n \rightarrow \pi^*$ transition and that the $-NH_2$ substituent involves a $\pi \rightarrow \pi^*$ transition. The theory, along with a full description of the fluorescence of aromatic amines, is given in detail by Kasha and Rawls.⁶ Previous research done by our group⁷ shows that the reduction of nitro aromatics to aromatic amines can be accomplished in one minute by using catalytic metallic (Pd) nanoparticles, synthesized in supercritical fluid carbon dioxide and subsequently supported on carbon nanotubes.⁸ In this previous research, we provided preliminary data⁷ indicating that 2,4-DNT vapor can be collected and rapidly reduced to 2,4-DAT, thereby allowing for fluorescence

Received 4 October 2006; accepted 9 November 2006.

* Authors to whom correspondence should be sent. E-mail: delyle@uidaho.edu; cwai@uidaho.edu.

analysis. Therefore, after this method of rapid reduction, fluorescence studies of the explosive vapors trapped in ethanol solution or potentially front surface on suitable substrates can occur. Our present approach uses a preliminary design for a prototype of a miniaturized sensor, perhaps with lasers or LEDs (light emitting diodes) to increase sensitivity.

When conventional fluorescence is used to analyze mixtures, the primary disadvantage is selectivity. This is due to the often broad and featureless characteristics of the excitation and emission spectra. The need for a highly sensitive and selective method of detecting explosives led us to explore synchronous luminescence (SL) for detection and identification of various explosive compounds (after reduction) simultaneously. Advantages of SL include decreases in the full-width at half-maximum (FWHM) of spectral bands, spectral band simplification, and a reduction in spectral overlap.⁹ The advantages that SL has over other detection methods directed us to study how this fluorescent technique could potentially be used for the simultaneous identification of individual explosive vapors in a mixture. Fluorescence identification of mixtures implementing the use of SL has been especially useful for petroleum oil spills as described by Eastwood.¹⁰ By applying the same principle, but with aromatic amines, this would allow for rapid, sensitive, and selective detection of explosive vapors with the discrimination necessary for the identification of individual components in a mixture. A full description of the theory, applications, and advantages of SL and use of forensic identification are given in the references.^{9,10}

Derivative spectroscopy is a technique that is commonly used when it is desired to reveal spectral detail that is not apparent in the original spectrum.⁹⁻¹² It is often used when analyzing mixtures, because it increases resolution, increases spectral discrimination, and can be used to improve fingerprint techniques to determine minor structural differences between similar spectra.^{9,12} Applying derivative spectroscopy to a spectrum has several effects on the signal. First, spectral bands with narrower FWHM values result in more intense derivative spectra;¹² therefore, derivative spectroscopy discriminates against wide peaks. Secondly, derivative spectroscopy decreases the signal-to-noise (S/N) ratio. To overcome this disadvantage, a smoothing function must be applied. Smoothing the spectrum is advantageous because it decreases noise and allows for more accurate peak position, peak height, and peak width.¹² The larger the smoothing function, the greater the decrease in noise; however, this results in a greater chance of spectral distortion due to over-smoothing. It is therefore a balance between desired noise reduction and concern about spectral distortion.

Quantum yields (QYs) have been considered to be one of the most important spectroscopic measurements for molecules.¹³ They provide information on radiationless decay, electronic transitions, purity, and chemical structures.^{14,15} Quantum yields are a measure of the ratio of photons emitted to photons absorbed, with values ranging from 0.000 to 1.00. A value of less than unity indicates that some radiationless decay has occurred; this includes internal conversion, vibrational relaxation, and intersystem crossing.¹⁶ Several methods of calculating absolute and relative QYs are available; however, the calculation of absolute QYs has been proven to be difficult.¹⁶ As a result, most spectroscopists choose the relative QY approach. Calculation of relative QYs can be troublesome if certain experimental factors are not considered; including

concentration, linear range, solvent, and excitation wavelength. High sample concentrations can cause nonlinearity, inner-filter effects, and self-absorption, resulting in inaccurate absorbance unit and emission intensity values.¹⁴ If different solvents are used, the refractive indices need to be considered. It is good practice to cross-reference known standards with one another to validate standard QY values.¹⁶ Incorrect QYs are far too easy to obtain; therefore, it is important when calculating unknown QYs that the chosen standard value is well established.¹⁶ In our study we are using the QY values to estimate relative fluorescence intensities. QYs offer valuable molecular information for the selected aromatic amines that is not currently available in the literature; therefore, we included them in this paper.

INSTRUMENTATION

As already discussed in previous research,⁷ experiments were carried out using a Spex (HORIBA Jobin Yvon) analytical grade spectrophotometer (FluoroMax-3TM) with a 150 watt xenon arc lamp. The instrument was calibrated by measuring the spectrum of the xenon lamp for the excitation monochromator (wavelength calibration and intensity) and measuring the water Raman peak for the emission monochromator (wavelength calibration and intensity). The reagents were all used as received and were the highest grade obtainable. The standard chemicals 2,4-DAT (99.4%) and 2,6-DAT (99.7%) were obtained from AccuStandard Inc, and *p*-toluidine and *o*-toluidine (97% or better) were obtained from Sigma. The solvent used was 200 proof USP ethanol. Nitric acid (singly distilled from Aldrich) and HPLC grade water, also from Aldrich, were used for cell cleaning. Fluorescein from Fluka was used to check the limit of detection of the instrument in a basic (NaOH) solution. To obtain SL spectra, you simultaneously scan the excitation and emission monochromators while keeping a constant wavelength interval (offset) between the two.⁵ Synchronous spectra were measured at an offset of 9.0 nm with bandwidths of 3.0 nm. All SL spectra are set to the excitation monochromator. To optimize resolution, all spectra reported here have an integration time of 1.0 s. Starna fused silica cells with 1 cm path length were used with right angle excitation for the solutions. All spectra were ethanol-blank subtracted. A Hewlett-Packard (8909A with Peltier temperature control accessory) ultraviolet-visible (UV-Vis) absorption instrument was used to obtain the absorption data needed for quantum yield measurements. A solid reference standard, holmium oxide filter, was used to determine absorbance and wavelength accuracy. The holmium oxide standard has various peak wavelengths between 279 nm and 637 nm. The wavelength accuracy is ± 0.2 nm, with an absorbance accuracy of ± 0.01 absorbance units. The standard was purchased from Avian Technologies LLC.

RESULTS AND DISCUSSION

Synchronous luminescence (SL) of three possible compounds in an explosive mixture, after reduction from nitro aromatics to aromatic amines,^{1,17} allowed for the discrimination necessary to distinguish among one major TNT-based compound and two minor TNT-based compounds in a mixture. This three-component artificial mixture consisted of 2,4-DAT, 2,6-DAT, and *p*-toluidine. We chose 2,4-DAT as the major reduction product due to its higher concentration and its higher

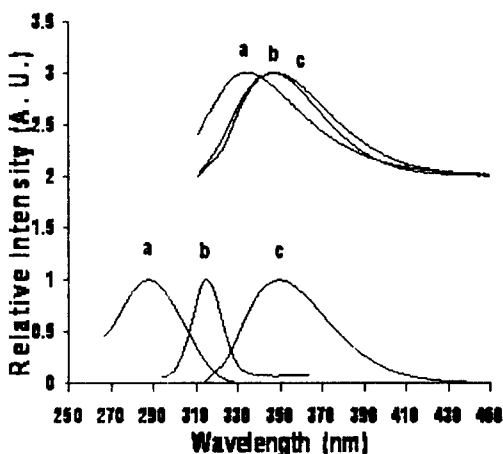


Fig. 1. (Top) Normalized emission spectra of (a) 2,6-DAT, (b) 2,4-DAT, and (c) *p*-toluidine. (Bottom) Normalized (a) excitation, (b) synchronous, and (c) emission spectra of *p*-toluidine. All are ethanol blank subtracted at a concentration of 1.0×10^{-4} M, 3.0 nm bandwidths.

stability compared to 1,3-DNB and its higher vapor pressure compared to TNT. Although 2,6-DNT is not considered a major explosive vapor, this minor component was chosen because it is frequently detected.¹ *p*-Nitrotoluene is a TNT-based compound that is also found in explosive materials; this compound has a higher vapor pressure than 2,4-DNT (0.03 torr compared to that of 2,4-DNT, 2.3×10^{-4} torr). It is for this reason we chose *p*-toluidine (the reduction product of *p*-nitrotoluene) as the second minor component in the artificial mixture. Our group recently studied the excitation and emission spectra of these and several other compounds.⁷ Due to the broad FWHM of these compounds, when overlaying the emission spectra of the three compounds, it is evident that the emission spectra would not yield adequate separation (Fig. 1, top). SL is a fluorescence technique that is known to simplify spectral bands and decrease the FWHM; therefore, we used SL to identify the aromatic amines. Figure 1 (bottom) shows the excitation, emission, and SL of *p*-toluidine. This figure shows how SL reduces the FWHM of the spectral bands. Maximum SL peak intensity occurs when an offset ($\Delta\lambda$) matches that of the Stoke's shift ($\delta\lambda$, $\delta\lambda = \lambda_{em} - \lambda_{ex}$);⁹ for these compounds that would be around 60.0 nm. Although the SL spectra using this offset did decrease the FWHM from 59.0 nm to 33.0 nm (compared to emission at the same concentration), this offset did not decrease the FWHM enough to be able to distinguish among compounds in a mixture. We tried several offsets until the desired separation of 2,4-DAT, 2,6-DAT, and *p*-toluidine was achieved. Figure 2 shows how decreasing the offset from 60.0 nm to 9.0 nm decreases the FWHM from 33.0 nm to 14.0 nm. Table I lists the FWHM values and peak wavelength location for excitation, emission, and SL for each compound studied. SL resulted in a decrease in FWHM of approximately 35.0 nm for each compound (compared to emission). To reduce the effects of scatter interference, bandwidths should not exceed half of the offset.⁹ For these compounds a bandwidth of 3.0 nm resulted in optimum selectivity. Figure 3 shows the overlaid individual SL spectra of 2,4-DAT, 2,6-DAT, and *p*-toluidine at 10^{-4} M. After it was confirmed that the individual SL spectra indicate appropriate separation, we analyzed a three-component artificial mixture. Figure 4 (left) is the SL of the artificial mixture containing 2,6-DAT at 4×10^{-5} M, 2,4-DAT at 2×10^{-5} M, and *p*-toluidine at 1.0×10^{-5} M. This

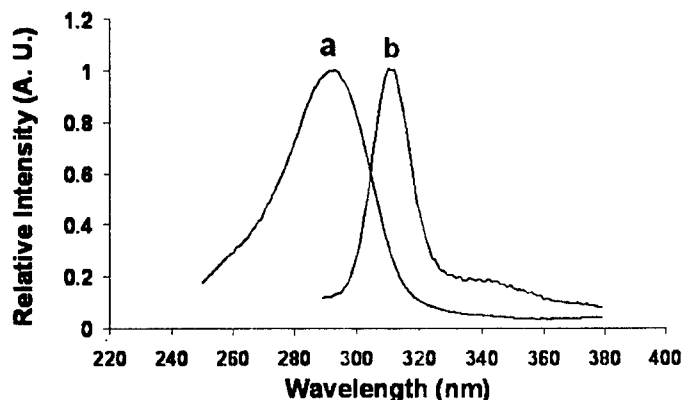


Fig. 2. Normalized SL spectra indicating decrease in FWHM with offset of (a) 60.0 nm to (b) 9.0 nm for 2,4-DAT at 4×10^{-5} M, bandwidth of 3.0 nm.

artificial mixture yields two peaks, one at 300 nm and the other at 314 nm. The peak at 300 nm correlates to the peak location of 2,6-DAT, but the peak at 314 nm does not correlate to either 2,4-DAT (310 nm) or *p*-toluidine (317 nm). Initially, this spectrum reveals only two peaks; however, after applying the second derivative, three peaks are revealed. The three peaks are located at 299 nm, 311 nm, and 316 nm, as seen in Fig. 4 (right). These peak wavelengths are consistent with 2,6-DAT, 2,4-DAT, and *p*-toluidine, respectively.

Derivative spectroscopy can be used to further increase selectivity of detection for multi-component mixtures like explosives. By comparing the SL spectra to the second-derivative spectra (Fig. 4, left, and Fig. 4, right), it is evident that derivative spectroscopy is essential in increasing the resolution to the level necessary to distinguish among overlapping spectral bands. In derivative spectroscopy, broader peaks become less intense and narrow peaks become more intense.¹² This is evident when comparing the spectrum of 2,6-DAT in the left-hand panel of Fig. 4 to that in the right-hand panel of Fig. 4. The peak at 300 nm in the left-hand panel is less intense than the other peak; in the right-hand panel, the peak at 300 nm becomes the most intense peak. Of the three compounds, this effect is most evident for 2,6-DAT because it has the smallest FWHM (refer to Table I). A consequence of applying a derivative to a spectrum is a decrease in the S/N ratio.^{9,12} It is important that a smoothing function is applied either prior to, or after, each derivative function. A 5-point Savitzky-Golay smoothing gave us the greatest resolution without sacrificing shifts in peak wavelength locations due to over-smoothing. The derivatives applied to the spectra were obtained using the FluorEssence™ software (January 2005), created by Spex® Fluorescence, and powered by Origin®. This software program obtains the derivative spectra by averaging

TABLE I. Compound, peak wavelength location, and FWHM.

Compound	Ex peak FWHM (nm)	Em peak FWHM (nm)	SL peak FWHM (nm)
2,6-DAT	287 27	335 51	300 10
<i>o</i> -toluidine	282 32	340 49	305 16
2,4-DAT	290 39	350 50	311 14
<i>p</i> -toluidine	285 42	349 50	317 15

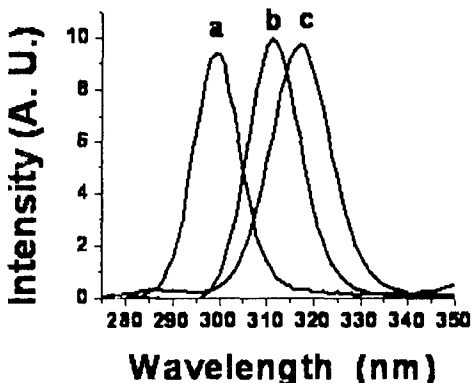


Fig. 3. Normalized overlaid synchronous spectra of (a) 2,6-diaminotoluene, (b) 2,4-diaminotoluene, and (c) p-toluidine. SL is set to wavelength of the excitation monochromator, all are ethanol blank subtracted at 1.0×10^{-4} M, offset of 9.0 nm, bandwidth of 3.0 nm.

the slopes of two adjacent data points. Equation 1 details how the operation is carried out by the software program; x represents the x-axis, y represents y-axis, and i represents the initial location:

$$\frac{1}{2} \left(\frac{y_{i+1} - y_i}{x_{i+1} - x_i} + \frac{y_i - y_{i-1}}{x_i - x_{i-1}} \right) \quad (1)$$

The success of the three-component mixture prompted us to analyze a four-component artificial mixture. This included the three compounds in the first artificial mixture, but with the addition of *o*-toluidine (1.0×10^{-5} M). *o*-Nitrotoluene is also a TNT-based compound found in explosive materials.^{1,17} Like *p*-nitrotoluene, *o*-nitrotoluene has a higher vapor pressure (0.11 torr) than 2,4-DNT; therefore, the detection of this compound is also important. Figure 5 (left) is the SL spectra of the four-component mixture, with a single peak located at 310 nm. Again, SL in conjunction with the second derivative was necessary to reveal all peaks in the mixture. The right-hand panel of Fig. 5 shows how remarkably well derivative spectroscopy can reveal hidden bands due to spectral overlap. After the application of the second derivative, four peaks corresponding to the four compounds in the mixture are

revealed, and at the expected wavelengths. Table II gives a summary of the experimental results, including individual SL peak locations at various concentrations and second-derivative (of SL) peak locations for mixture 1 and mixture 2. This table shows that concentration, artificial mixtures, and derivative spectroscopy did not affect the peak wavelength location by more than one nanometer. As indicated by Table II and Fig. 5, with these parameters, each of the four compounds have peak wavelength maxima that are separated by only 5.0 nm, and yet with the use of SL and derivative spectroscopy, we have the resolution necessary to distinguish among the four compounds in an artificial mixture. For the SL studies ($\Delta\lambda = 9.0$ nm), it was determined that the detection limits for 2,4-DAT, 2,6-DAT, *p*-toluidine, and *o*-toluidine were 2.6×10^{-6} M, 2.3×10^{-6} M, 6.7×10^{-7} M, and 1.7×10^{-7} M, respectively. The data presented within this research paper were obtained in ethanol solutions; however, from preliminary data acquired from previous research,⁷ we anticipate that the same results will be obtained in a gas-phase sample. By using a more sensitive detector, and a more intense excitation source, a decrease in the detection limit can potentially be achieved.¹⁶ In the artificial mixtures, *p*-toluidine and *o*-toluidine were chosen to have lower concentrations than the other two compounds due to the high likelihood that they would be found in less abundance. 2,6-DAT would most likely be found at a lower concentration than 2,4-DAT; however, for clarity we chose a higher concentration of 2,6-DAT to 2,4-DAT. Typical real-world sample concentrations for these compounds have large variations depending on the type of landmine.¹ Additionally, environmental factors such as moisture and temperature cause variation in detection concentrations. Taking one example (lab sample # N99-79) from the literature, 2,4-DNT had a concentration of 6013 ($\mu\text{g}/\text{kg}$) and 2,6-DNT had a concentration of 3480 ($\mu\text{g}/\text{kg}$).¹ *p*-Nitrotoluene and *o*-nitrotoluene were not detected in this sample since they were below the detection limit of the GC-ECD instrument used. All of our experiments were reproduced at least in triplicate. We analyzed other mixtures with varying concentrations; all gave similar results to the above data. In one case, using the fourth derivative gave clearer results, but usually this was not necessary. It has been determined that, at the same concentration, the SL maximum intensity (I_{\max}), for the four compounds are *o*-toluidine, $>$ *p*-toluidine $>$ 2,4-DAT $>$ 2,6-DAT.

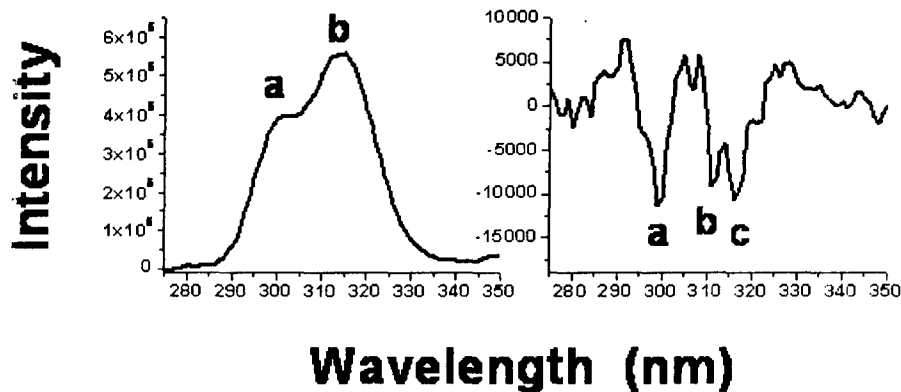


Fig. 4. (Left) SL of a three-component artificial mixture, (a) 300 nm, and (b) 314 nm. (Right) The second derivative of the SL spectra on the left. Three peaks at (a) 299 nm, (b) 311 nm, and (c) 316 nm correspond to 2,6-DAT, 2,4-DAT, and *p*-toluidine, respectively.

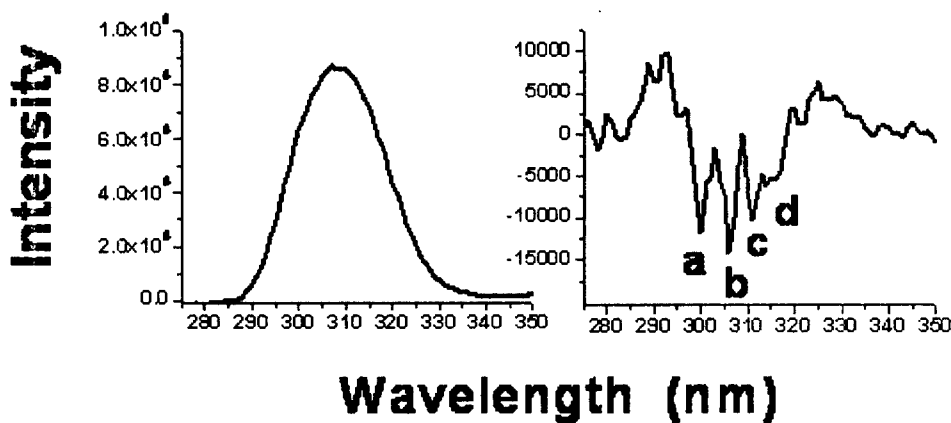


FIG. 5. (Left) SL of a four-component artificial mixture, single peak is located at 310 nm. (Right) Second derivative of SL on the left. Four peaks at (a) 300 nm, (b) 305 nm, (c) 311 nm, and (d) 316 nm corresponding to 2,6-DAT, o-toluidine, 2,4-DAT, and p-toluidine, respectively.

Quantum yields (QYs) provide specific information about a compound; therefore the added molecular information makes determining the QY values of the selected aromatic amines important.¹⁴ QY is defined as the ratio of the number of photons emitted to the number of photons absorbed.⁵ There are several ways to calculate quantum yields;^{15,18} we have chosen the most widely used method of using relative quantum yields.¹⁹ Equation 2 indicates how we calculated the relative QYs.¹⁹

$$QY_X = \frac{(QY_S)(D_X)(A_S)(I_S)(n_X^2)}{(D_S)(A_X)(I_X)(n_S^2)} \quad (2)$$

QY is the quantum yield, S is the standard, and X is the unknown. A is the absorbance value at the excitation wavelength, D is the integrated area under the curve in photon units, I is the intensity of the lamp at the excitation wavelength, and n is the index of refraction of the solution. It is important when calculating QYs that saturation, quenching, and self-absorption do not become a problem. Therefore, it is recommended that only dilute solutions are used and that absorption values remain under 0.05 absorbance units.^{13,16,20} For all of our measurements the absorbance was measured on a Hewlett-Packard instrument with absorbance units less than 0.05. For both absorbance and fluorescence measurements, we ensured that solute concentrations were in the linear range and that saturation of the detector did not occur. The D term (integrated area under the curve) is obtained by acquiring the fluorescence emission spectra of the sample, making sure that the value is in photon units. The I term (intensity of the lamp) is

obtained by acquiring the fluorescence excitation spectra of the excitation source; for our research this was a 150 watt xenon lamp. The I value is simply the intensity of the lamp, at the wavelength used to excite the sample. For our calculations we could neglect the refractive index term since all samples were dissolved in the same solvent. To ensure accurate results of the relative QYs, we cross-referenced two known reference standards, sulforhodamine 101 (in ethanol) and anthracene (in ethanol). Literature QY values and our measured QY values for these standards are given in Table III. By comparison, our measured quantum yields are similar to the literature QY values and fall within the expected error range; an error^{16,20} of 5% to 10% is considered reasonable. Calculated quantum yields for 2,4-DAT, 2,6-DAT, p-toluidine, and o-toluidine are also given in Table III. QY values were measured at least in triplicate, with the average value and standard deviation given in the table. By solely taking into account the I_{max} 's of these compounds, the QY results for the four aromatic amines are as predicted, o-toluidine > p-toluidine > 2,4-DAT > 2,6-DAT.

CONCLUSION

In summary, we show that by implementing synchronous luminescence (SL) and derivative spectroscopy, we have the resolution to distinguish among four likely reduction products present in a TNT-based explosive mixture. SL has advantages over other identification techniques in that, in addition to being rapid and sensitive, SL is selective. This is demonstrated by our research on artificial mixtures of the reduction products 2,4-DAT, 2,6-DAT, p-toluidine, and o-toluidine. Derivative spectroscopy further increased selectivity by revealing spectral

TABLE II. Compound, SL peak wavelength location at corresponding concentration, and second-derivative peak (SL) of mixtures.

Compound	SL peak of individual compound (nm)	[C] (mol/L)	2nd derivative peaks of SL for mixture 1 (nm)	2nd derivative peaks of SL for mixture 2 (nm)
2,6-DAT	300, 299	$1.0 \times 10^{-4}, 1.0 \times 10^{-5}$		
<i>o</i> -toluidine	300, 300	$4 \times 10^{-5}, 4 \times 10^{-6}$	299	300
	305, 306 305	$1.0 \times 10^{-4}, 1.0 \times 10^{-5}$ 1.0×10^{-6}	NA	305
2,4-DAT	311, 310	$1.0 \times 10^{-4}, 1.0 \times 10^{-5}$		
<i>p</i> -toluidine	311, 311	$2 \times 10^{-5}, 2 \times 10^{-6}$	311	311
	317, 317 316	$1.0 \times 10^{-4}, 1.0 \times 10^{-5}$ 1.0×10^{-6}	316	316

TABLE III. Quantum yield values for selected aromatic amines.

Compound	Solvent	Standard	λ_{ex} nm	Spectral range (nm)	Average quantum yield	Std. dev.
Sulforhodamine 101	Ethanol	A ^a	565	570-750	0.985	±0.090
Anthracene	Ethanol	S ^b	356	370-540	0.295	±0.030
2,6-DAT	Ethanol	A ₊	290	310-450	0.011	±0.002
<i>o</i> -toluidine	Ethanol	A ₊	290	310-450	0.174	±0.013
2,4-DAT	Ethanol	A ₊	295	310-450	0.035	±0.008
<i>p</i> -toluidine	Ethanol	A ₊	290	300-450	0.094	±0.009

^a A₊ Anthracene used as reference standard (0.300).^{16,18,24}^b S^b Sulforhodamine 101 used as reference standard (1.00).^{20,23}

peaks not readily apparent due to spectral overlap. Although SL has been used with wide applications for oils,¹⁰ polycyclic aromatic hydrocarbons (PAHs),⁹ and phenols,²¹ we report the first successful results using SL for the identification of aromatic amines. Hyfantis et al. used a field-portable synchronous scanning luminescope (SSL) to detect PAHs and pesticides.²² Although they did attempt to use this instrument to detect TNT, it was used as a colorimeter with zero offset, so that they did not use the power of SL. This leads us to believe that a field-portable SL instrument could be customized for the identification of explosive vapors. QYs give valuable information about a compound, including purity, structure, and relative fluorescence intensities. With careful analytical technique, we have obtained the relative QYs of the selected aromatic amines. Our proposed method is directed at detecting explosive vapors. Since we are not analyzing soil or water samples, the matrix effects are negligible. Further studies implementing SL for analyzing other TNT-based explosive vapors are also of interest to us. These would include the reduction products related to aminobenzenes and the isomers of diaminobenzene that are also found in many landmines. We are also interested in other types of explosives; with appropriate modifications, our general approach could possibly be applied to these explosives. Future work will also include more research on the rapid reduction and collection of various explosive vapors.

ACKNOWLEDGMENTS

This work was partially supported by a grant from DOD-AFOSR (F49620-03-1-0361), and by Battelle (27887). The authors (D.E. and C.M.W.) want to thank Dr. Howard Mayfield from AFRL Tyndall AFB (FL), and Dr. R. S. Addleman from Pacific Northwest National Laboratory for their helpful discussions. We also wish to thank Dr. Ron Crawford of the Department of Environmental Research Institute (ERI) for the use of his absorption instrument.

1. T. F. Jenkins, M. E. Walsh, P. H. Miyares, J. A. Kopeczynski, T. A. Ranney, V. George, J. C. Pennington, and T. E. Berry, Jr., "Analysis of Explosives-Related Chemical Signatures in Soil Samples Collected Near Buried Land Mines", US Army Cold Regions Research and Engineering Laboratory, Technical Report 00-5, 1 (2000).
2. J. W. Gardner, "Review of Conventional Electronic Nose and Their Possible Application to the Detection of Explosives", in *Electronic Noses and Sensors for the Detection of Explosives*, J. W. Gardner and J. Yinon, Eds. (Kluwer Academic Publishers, Boston, 2004), Chap. 1, p. 1.
3. D. S. Moore, *Rev. Sci. Instrum.* **75**, 2499 (2004).
4. T. Swager, "Polymer Electronics for Explosive Detection", *Electronic Noses and Sensors for the Detection of Explosives*, E. L. Wehry and J. Yinon, Eds. (Kluwer Academic Publishers, Boston, 2004), Chap. 2, p. 29.
5. E. L. Wehry, "Effects of Molecular Structure on Fluorescence and Phosphorescence", in *Practical Fluorescence*, G. G. Guilbault, Ed. (Marcel Dekker, New York, 1990), 2nd ed., Chap. 3, p. 75.
6. M. Kasha and R. H. Rawls, *Photochem. Photobiol.* **7**, 561 (1968).
7. D. Eastwood, C. Fernandez, B. Yoon, C. N. Sheaff, and C. M. Wai, *Appl. Spectrosc.* **60**, 958 (2006).
8. B. Yoon and C. M. Wai, *J. Am. Chem. Soc.* **127**, 17174 (2005).
9. T. Vo-Dinh, "Synchronous Excitation Spectroscopy", in *Modern Fluorescence Spectroscopy*, E. L. Wehry, Ed. (Plenum Press, New York, 1981), vol. 4, Chap. 5, p. 167.
10. D. Eastwood, "Use of Luminescence Spectroscopy in Oil Identification", in *Modern Fluorescence Spectroscopy*, E. L. Wehry, Ed. (Plenum Press, New York, 1981), vol. 4, Chap. 7, p. 251.
11. D. A. Skoog, F. J. Holler, and T. A. Nieman, "Molecular Luminescence Spectrometry", in *Instrumental Analysis*, J. Vondeling, M. Sherman, J. Bortel, V. Peculis, and F. Mésina, Eds. (Books/Cole Thomson Learning, USA, 1998), Chap. 15, p. 335.
12. T. O'Haver, "An Introduction to Signal Processing in Chemical Analysis", <http://www.wam.umd.edu/~tob/spectrum/TOC.html> (2006).
13. C. L. Renschler and L. A. Harrah, *Anal. Chem.* **55**, 798 (1983).
14. I. B. Berlin, "The Determination of Quantum Yields", in *Handbook of Fluorescence Spectra of Aromatic Molecules* (Academic Press, New York, 1965), Chap. 5, p. 68.
15. S. P. Nighswander-Rempel, *J. Fluoresc.* **16**, 483 (2006).
16. HORIBA Jobin Yvon, "A Guide to Recording Fluorescence Quantum Yields", www.jyhoriba.co.uk.
17. V. N. Ivanova and V. A. Nadolinnyi, *Khimiya v Interesakh Ustoichivogo Razvitiya* **11**, 353 (2003) [English transl: Publisher Siberian Branch of Russian Academy of Science].
18. C. A. Parker and W. T. Rees, *Analyst* (Cambridge, U.K.) **85**, 587 (1960).
19. J. N. Demas and G. A. Crosby, *J. Phys. Chem.* **75**, 8 (1971).
20. R. A. Velapoldi and H. H. Tønnesen, *J. Fluoresc.* **14**, 4 (2004).
21. F. J. Purcell, R. Kantinski, and R. H. Obernauf, "Synchronous-Excitation Fluorescence Applied to Characterization of Phenolic Species", in *Advances in Luminescence Spectroscopy*, C. Love and D. Eastwood, Eds. (ASTM, Philadelphia, PA, 1985), p. 81.
22. G. J. Hyfantis, S. Matthew, Jr., T. P. Finnegan, P. J. Mulligan, and W. Watts, *Proc. SPIE-Int. Soc. Opt. Eng.* **3853**, 110 (1999).
23. R. Haugland, "Tools for Fluorescence Applications", in *The Handbook-A Guide to Fluorescent Probes and Labeling Technologies*, T. Z. Spence, Ed. (Invitrogen Corp., USA, 2005), 10th ed., Chap. 23, p. 987.
24. C. A. Parker, "Measurement of Fluorescence Efficiency", in *Photoluminescence of Solutions* (Elsevier, New York, 1968), Chap. 3, p. 261.